

DISSERTATION

ASSESSMENT OF THE EFFECTS OF LIGAMENTOUS INJURY IN THE HUMAN CERVICAL SPINE

Submitted by

Patrick Devin Leahy

Department of Mechanical Engineering

In partial fulfillment of the requirements

For the Degree of Doctor of Philosophy

Colorado State University

Fort Collins, Colorado

Spring 2012

Doctoral Committee:

Advisor: Christian Puttlitz

Paul Heyliger  
Hiroshi Sakurai  
Brandon Santoni

Copyright by Patrick Devin Leahy 2012

All Rights Reserved

## ABSTRACT

### ASSESSMENT OF THE EFFECTS OF LIGAMENTOUS INJURY IN THE HUMAN CERVICAL SPINE

Ligamentous support is critical to constraining motion of the cervical spine. Injuries to the ligamentous structure can allow hypermobility of the spine, which may cause deleterious pressures to be applied to the enveloped neural tissues. These injuries are a common result of head trauma and automobile accidents, particularly those involving whiplash-provoking impacts. The injuries are typically relegated to the facet capsule (FC) and anterior longitudinal (ALL) ligaments following cervical hyperextension trauma, or the flaval (LF) and interspinous (ISL) ligaments following hyperflexion. Impacts sustained with the head turned typically injure the alar ligament. The biomechanical sequelae resulting from each of these specific injuries are currently ill-defined, confounding the treatment process. Furthermore, clinical diagnosis of ligamentous injuries is often accomplished by measuring the range of motion (ROM) of the vertebrae, where current methods have difficulty differentiating between each type of ligamentous injury.

Pursuant to enhancing treatment and diagnosis of ligamentous injuries, a finite element (FE) model of the intact human full-cervical (C0-C7) spine was generated from computed tomography (CT) scans of cadaveric human spines. The model enables the quantification of ROM, stresses, and strains, and can be modified to reflect ligamentous injury. In order to validate the model, six human, cadaveric, full-cervical spines were tested under pure  $\pm 1.5$  Nm

moment loadings in the axial rotation, lateral bending, flexion, and extension directions. ROM for each vertebra, facet contact pressures, and cortical strains were experimentally measured.

To evaluate injured ligament mechanical properties, a novel methodology was developed where seven alar, fourteen ALL, and twelve LF cadaveric bone-ligament-bone preparations were subjected to a partial-injury inducing, high-speed (50 mm/s) tensile loading. Post-injury stiffnesses and toe region lengths were compared to the pre-injury state for these specimens.

These experimental data were incorporated into the FE model to analyze the kinematic and kinetic effects of partial ligamentous injury. For comparison, the model was also adapted to reflect fully injured (transected) ligaments. Injuries simulated at the C5-C6 level included: 1) partial FC injury, 2) full FC injury, 3) partial FC and ALL injury, 4) full FC and ALL injury, 5) partial LF and full ISL injury, 6) full LF and ISL injury, 7) partial FC, ALL, LF, and full ISL injury, and 8) full FC, ALL, LF, and ISL injury. The model was also modified to replicate injury to the right alar ligament. Five cadaveric cervical spines were tested under pure moment conditions with scalpel-sectioning of these ligaments for validation of the full-injury models.

Comparisons between the intact and various injury cases were made to determine the biomechanical alterations experienced by the cervical spine due to the specific ligamentous injuries. Variances in ROM and potential impingement on the neural tissues were focused upon. The overarching goals of the study were to identify a unique kinematic response for each specific ligamentous injury to allow for more accurate clinical diagnosis, and to enhance the understanding of the post-injury biomechanical sequelae.

## **ACKNOWLEDGEMENTS**

I would like to thank my advisor, Dr. Christian Puttlitz, for his guidance in making this project novel and applicable to pertinent issues in the field of biomechanics. I also appreciate the assistance of my committee, Drs. Paul Heyliger, Hiroshi Sakurai, and Brandon Santoni, who have been involved in laying out the fundamentals of this work as well as assisting with the finer points. For dealing with issues involving the two worthy foes of computers and statistics, I would like to thank Mark Ringerud and Jim zumBrunnen, respectively. Tribute is owed to Vikas Patel for adding a clinical viewpoint. Lastly, a great deal of gratitude is bestowed upon my friends and colleagues in the OBRL: Ugur Ayturk, Cecily Broomfield, Katrina Easton, Ben Gadomski, Kevin Labus, Kirk McGilvray, Amy Lyons Santoni, Snehal Shetye, Kevin Troyer, and Wes Womack. Each of you has provided vital assistance, support, and comic relief.

## **DEDICATION**

This work is dedicated to my father, who taught me to strive for the best.

## TABLE OF CONTENTS

ABSTRACT.....	ii
ACKNOWLEDGEMENTS.....	iv
DEDICATION.....	v
LIST OF FIGURES.....	viii
LIST OF TABLES.....	xii
LIST OF EQUATIONS.....	xiii
1 BACKGROUND.....	1
1.1 Function of the Human Cervical Spine.....	1
1.2 Anatomy of the Human Cervical Spine.....	1
1.2.1 Geometry.....	1
1.2.2 Materials.....	14
1.3 History of Human Cervical Spine Experimental Biomechanical Testing.....	21
1.3.1 <i>In-vivo</i> Testing.....	22
1.3.2 <i>In-vitro</i> Testing.....	23
1.3.3 Intact Testing.....	24
1.3.4 Injury Testing.....	24
1.4 History of Cervical Spine Finite Element Modeling.....	25
1.5 Cervical Spine Affliction.....	26
2 SPECIFIC AIMS IN RESPONSE TO CERVICAL SPINE LIGAMENTOUS INJURY.....	29
2.1 Specific Aim 1: Develop a converged and validated computational finite element model of the intact full-cervical (C0-C7) osteoligamentous complex.....	29
2.2 Specific Aim 2: Experimentally determine the mechanical properties of ligaments commonly injured in whiplash-type trauma.....	30
2.3 Specific Aim 3: Modify the intact cervical spine finite element model to include injured ligament mechanical properties in order to simulate the effects of ligamentous injury on the cervical spine.....	31
2.4 Specific Aim 4: Use the aforementioned intact and damaged cervical models to enhance the diagnostic procedure.....	32
3 EXPERIMENTAL METHODOLOGY AND DATA.....	33
3.1 Intact Cervical Spine Finite Element Model (Specific Aim 1).....	35
3.1.1 Intact Cervical Spine Finite Element Model Generation.....	35
3.1.2 Intact Cervical Spine Finite Element Model Convergence.....	47
3.1.3 Intact Cervical Spine Finite Element Model Analysis.....	49
3.1.4 Intact Cervical Spine Finite Element Model Experimental Validation Method.....	51

3.1.5	Intact Cervical Spine Finite Element Model Analytic and Experimental Validation Results.....	56
3.2	Experimental Measurement of Injured Ligament Mechanical Properties (Specific Aim 2).....	70
3.2.1	Injured Ligament Properties Experimental Method .....	70
3.2.2	Injured Ligament Properties Experimental Data Analysis .....	74
3.2.3	Injured Ligament Properties Experimental Results .....	75
3.3	Ligamentous Injury Cervical Spine Finite Element Model (Specific Aim 3) .....	79
3.3.1	Ligamentous Injury Cervical Spine Finite Element Model Generation .....	79
3.3.2	Ligamentous Injury Cervical Spine Finite Element Model Analysis .....	80
3.3.3	Ligamentous Injury Cervical Spine Finite Element Model Experimental Validation Method.....	81
3.3.4	Ligamentous Injury Cervical Spine Finite Element Model Analytic and Experimental Validation Results .....	82
3.4	Comparison of Cervical Spine Finite Element Models in Pursuit of an Enhanced Diagnostic Procedure (Specific Aim 4).....	94
3.4.1	Diagnostic Enhancement Analytical and Experimental Method .....	94
3.4.2	Diagnostic Enhancement Analytical and Experimental Results.....	96
4	OVERALL CONCLUSIONS.....	104
5	FUTURE WORK .....	105
6	REFERENCES .....	107

## LIST OF FIGURES

Figure 1: The entire spine with each region denoted. Variation in curvature from the lordotic cervical and lumbar regions to the kyphotic thoracic region is demonstrated (adapted from Gray's Anatomy [36, 124]).	2
Figure 2: Bending axes of the spine (adapted from White[121]).	3
Figure 3: The full-cervical spine vertebrae, divided into the upper and lower regions. The occiput (C0) is not pictured (adapted from Gray's Anatomy [36, 124]).	3
Figure 4: A typical lower-cervical vertebra, showing superior (A) and lateral (B) views (adapted from www.ispub.com [128]).	4
Figure 5: Demonstration of coupled axial rotation with lateral bending (adapted from White [122]).	6
Figure 6: C2 (axis) vertebra, showing the prominent dens protrusion (adapted from Gray's Anatomy [35]).	7
Figure 7: (Left) The composition and local coordinate system of the intervertebral disc. (Middle) Collagen fiber orientation on the periphery of the annulus. (Right) Hydrostatic pressure exerted by the nucleus when the disc is compressed (adapted from Joshi [48]).	8
Figure 8: Ligaments of the lower cervical spine shown on a typical lower-cervical functional spinal unit (adapted from www.uphs.penn.edu [124, 129]).	11
Figure 9: (Left) The anatomy and ligamentous support of the atlanto-axial joint (adapted from Panjabi [84]). (Right) A simplified model of alar restraint on atlantal and occipital axial rotation [22].	12
Figure 10: The structure and constitutive materials of bone [100].	15
Figure 11: The three-layer composition of cartilage (adapted from Mow [70]).	19
Figure 12: A typical method for evaluating vertebral rotations from radiographic imaging. (Left) Total lordosis angle of the lower cervical spine is measured. (Right) Relative intervertebral angle at a single functional spine unit is measured (adapted from Harrison [39, 124]).	27
Figure 13: Synthesis of the finite element model proceeding from top left: (A) Segmented voxels are assigned to specific tissues in Amira. (B) Smoothed surfaces are generated from the segmented voxels in Amira. (C) Meshed elements are projected in TrueGrid to surfaces created in Amira. (D) Solid and shell elements are imported into ABAQUS, where spring elements and articular cartilage are added. Note the axial rotation of C0 and C1 in figures B and C, and its subsequent reduction in figure D after reorientation (see section 3.1.1.1.5 Model Orientation).	36
Figure 14: Sagittal view of the segmentation of the intervertebral disc, showing annulus (green) and nucleus (pink).	38

Figure 15: Finite element model of the annular ground substance (green) and collagen fibers (blue). ..... 38

Figure 16: (Left) Arrow highlights articulating cartilage on the dens as imaged via  $\mu$ CT. Cartilage thickness was measured at 3-5 points across the width of the cross-section. (Right) Cartilage at the same anatomic location as modeled in ABAQUS. Note the three-layer arrangement, shown in green (deep), white (mid), and red (superficial) colored elements. The blue colored elements denote cortical bone. .... 40

Figure 17: Example of the dispersed spring elements (red) used to model the physiologic width of the ligaments. The flaval ligament is shown..... 41

Figure 18: The peripheral dispersion of the facet capsule ligament spring elements (white). .... 42

Figure 19: Solid element (tan) representation of the transverse atlantal element. .... 42

Figure 20: Method of lowering mesh resolution. A row of elements is deleted, and the adjacent rows are merged. .... 48

Figure 21: Approximate locations of the intervertebral foramina measurement points [83]. .... 50

Figure 22: Experimental setup for full-cervical spine testing showing typical strain gauge placement. The load-cell is obscured by the strain gauge wiring..... 52

Figure 23: Custom driveshaft is shown attached to the stepper motor on left and occiput mount on right..... 52

Figure 24: A wooden wedge was affixed to the caudal face of C7 to maintain a physiologic lordosis angle when potted in PMMA. .... 53

Figure 25: A typical moment/rotation plot for a functional spinal unit. Hysteresis is evident between the loading and unloading curves..... 55

Figure 26: Summed intervertebral biaxial rotation comparison between current and previous studies for intact cervical spines at 1.5 Nm loading [61, 80, 122]. Standard deviation bars are shown for current experiments. .... 57

Figure 27: Summed intervertebral bilateral bending comparison between current and previous studies for intact cervical spines at 1.5 Nm loading [44, 62, 96]. Standard deviation bars are shown for current experiments. .... 57

Figure 28: Summed intervertebral flexion+extension rotation comparison between current and previous studies for intact cervical spines at 1.5 Nm loading [44, 62, 96]. Standard deviation bars are shown for current experiments. .... 58

Figure 29: The nonlinear experimental (Exp) and FE-predicted C0-C1 intervertebral rotations due to the application of moments about the three primary bending axes. The experimental averages are plotted within corridors formed by +/- one standard deviation. The negative moment denotes flexion in the flexion and extension plot..... 60

Figure 30: The nonlinear experimental (Exp) and FE-predicted C1-C2 intervertebral rotations due to the application of moments about the three primary bending axes. The experimental averages are plotted within corridors formed by +/- one standard deviation. The negative moment denotes flexion in the flexion and extension plot..... 61

Figure 31: The nonlinear experimental (Exp) and FE-predicted C2-C3 intervertebral rotations due to the application of moments about the three primary bending axes. The experimental

averages are plotted within corridors formed by +/- one standard deviation. The negative moment denotes flexion in the flexion and extension plot..... 62

Figure 32: Experimentally-measured movement of the center of C1-C2 facet contact pressure from flexion (left) to extension (right). Axes labels correspond to discrete pressure measurement regions on the Tekscan film (each region measures 1.27 mm by 1.27 mm). ..... 63

Figure 33: The experimentally-measured (Exp) and FE-predicted unilateral contact forces at the C1-C2 facets throughout moment loading. The experimental averages are plotted within corridors formed by +/- one standard deviation. The negative moment denotes flexion in the flexion and extension plot. .... 64

Figure 34: The experimentally-measured (Exp) and FE-predicted cortical strains at the atlas at peak moments. Average strains were generally reduced when the facet capsule ligaments were sectioned at the atlanto-axial joint..... 66

Figure 35: The FE-predicted change in left C5-C6 intervertebral foramen height and width for the intact cervical spine due to the application of a 1.5 Nm moment. .... 67

Figure 36: The variance in convergence parameters relative to the base (Medium Resolution) model. .... 69

Figure 37: A typical bone-ligament-bone preparation, prior to potting in PMMA (LF shown). .... 71

Figure 38: Wires were used to prevent slippage of the dens within the PMMA (red arrow). Wires were also employed to hold the occipital and atlantal bones together in a physiologic configuration (the atlanto-occipital junction is denoted with the blue arrow)..... 71

Figure 39: The ligament tensile-testing apparatus. .... 73

Figure 40: Alignment of the holes in the sliding, actuator-mounted square tube and potting box-mounted rod prior to shear-pin insertion ensured no initial force was applied by the actuator to the ligament..... 74

Figure 41: A typical ligament force/displacement plot shows an increase in toe region length (displacement at 10 N) after injury..... 76

Figure 42: A typical damage step force/displacement curve. The displacement continued to increase after the force drop, indicating system lag. .... 78

Figure 43: Experimentally-measured (Exp) and FE-predicted C5-C6 summed biaxial rotations for various ligamentous injuries at 0.75 Nm loading. Standard deviation bars are shown for experimental data..... 82

Figure 44: Experimentally-measured (Exp) and FE-predicted C5-C6 summed bilateral bending rotations for various ligamentous injuries at 0.75 Nm loading. Standard deviation bars are shown for experimental data. .... 83

Figure 45: Experimentally-measured (Exp) and FE-predicted C5-C6 summed flexion+extension rotations for various ligamentous injuries at 0.75 Nm loading. Standard deviation bars are shown for experimental data. .... 83

Figure 46: FE-predicted C5-C6 summed biaxial rotations for various ligamentous injuries with intertransverse tissue damage at 0.75 Nm loading. .... 85

Figure 47: FE-predicted C5-C6 summed bilateral bending rotations for various ligamentous injuries with intertransverse tissue damage at 0.75 Nm loading. .... 86

Figure 48: FE-predicted C5-C6 summed flexion+extension rotations for various ligamentous injuries with intertransverse tissue damage at 0.75 Nm loading. .... 86

Figure 49: FE-predicted change in left C5-C6 intervertebral foramen height for various injuries due to the application of a 0.75 Nm moment. The intact and full FC+ALL injury spines loaded with 1.5 Nm moments are also shown for comparison..... 88

Figure 50: FE-predicted change in left C5-C6 intervertebral foramen width for various injuries due to the application of a 0.75 Nm moment. The intact and full FC+ALL injury spines loaded with 1.5 Nm moments are also shown for comparison..... 88

Figure 51: FE-predicted change in left C5-C6 intervertebral foramen height for various injuries with intertransverse tissue injury due to the application of a 0.75 Nm moment. The intact and full FC+ALL injury spines loaded with 1.5 Nm moments are also shown for comparison..... 90

Figure 52: FE-predicted change in left C5-C6 intervertebral foramen width for various injuries with intertransverse tissue injury due to the application of a 0.75 Nm moment. The intact and full FC+ALL injury spines loaded with 1.5 Nm moments are also shown for comparison..... 90

Figure 53: Experimentally-measured (Exp) and FE-predicted C1-C2 summed intervertebral rotations for various ligamentous injuries at 0.75 Nm loading. Standard deviation bars are shown for experimental data. .... 92

Figure 54: Experimentally-measured (Exp) and FE-predicted C0-C1 summed intervertebral rotations for various ligamentous injuries at 0.75 Nm loading. Standard deviation bars are shown for experimental data. .... 93

Figure 55: (Left) Intervertebral angles were measured in flexion and extension by comparing the angles made between the yellow lines at  $\pm 0.75$  Nm. These lines were drawn between the anterior/caudal endplate and the posterior/cranial wall of the spinal canal. (Right) A similar procedure was used to measure intervertebral angles in lateral bending. These lines were drawn between the uncinat processes. .... 95

Figure 56: Radiographs were taken of the spines while under steady-state, pure-moment loading. The x-ray radiation source (the yellow box at right) blocked the motion analysis markers when in use. .... 96

Figure 57: Comparison of FE-predicted C5-C6 intervertebral rotations for the various ligamentous injuries due to a 0.75 Nm moment. .... 98

Figure 58: Comparison of FE-predicted C5-C6 intervertebral rotations for the various ligamentous injuries with intertransverse tissue damage due to a 0.75 Nm moment. .... 98

Figure 59: Comparison between intervertebral angle measurements made by the stereophotogrammetric motion analysis system and graphical measurements from radiographs. .... 99

Figure 60: A diagnostic flowchart to be utilized with clinical range of motion test data. .... 102

Figure 61: A diagnostic flowchart to be utilized with clinical range of motion test data with intertransverse tissue damage. .... 103

## LIST OF TABLES

Table 1: Mechanical properties for multiple loading conditions on the cervical intervertebral disc and anterior longitudinal ligament complex [69].	17
Table 2: Previously reported quasistatic stiffness values for cervical ligaments [11, 17, 56, 81, 88, 105, 130, 132, 134].	20
Table 3: Cadaveric cervical spine specimen pool. The far right column describes the tests run on each individual specimen.	34
Table 4: Material properties for cortical and trabecular bone in the upper-cervical portion of the finite element model.	45
Table 5: Articular cartilage material properties and thickness distribution used in the cervical finite element model. Two-layer cartilage structures used a 45% superficial, 55% deep thickness distribution.	46
Table 6: Summary of the ligament properties used in the cervical finite element model. Average stiffnesses are reported due to the highly nonlinear properties of the ligaments.	46
Table 7: Number of elements comprising soft tissues in the upper cervical FE model. (*) denotes the use of second-order elements.	49
Table 8: Alar stiffness before and after induced damage. The standard deviations are shown in parentheses. Significant ( $p < 0.01$ ) differences are shown in shaded cells.	76
Table 9: Alar displacement at reference forces before and after damage. The standard deviations are shown in parentheses. Significant ( $p < 0.01$ ) differences are shown in shaded cells.	76
Table 10: ALL stiffness before and after induced damage. The standard deviations are shown in parentheses. Significant ( $p < 0.01$ ) differences are shown in shaded cells.	77
Table 11: ALL displacement at reference forces before and after damage. The standard deviations are shown in parentheses. Significant ( $p < 0.01$ ) differences are shown in shaded cells.	77
Table 12: LF stiffness before and after induced damage. The standard deviations are shown in parentheses. Negative stiffness reduction indicates stiffness increased after damage. Significant ( $p < 0.01$ ) differences are shown in shaded cells.	77
Table 13: LF displacement at reference forces before and after damage. The standard deviations are shown in parentheses. Significant ( $p < 0.01$ ) differences are shown in shaded cells.	77
Table 14: Cervical stabilization of the spine with ligamentous and intertransverse tissue injury is recommended when measured values exceed that of the intact 1.5 Nm-loaded case.	101

## LIST OF EQUATIONS

Equation 1: Calculation for modulus from CT density.....	44
Equation 2: Calculation of transverse and shear moduli.....	44
Equation 3: Calculation of strain gauge principal strains from the strain of the individual gauge components.....	55

## **1 BACKGROUND**

### **1.1 Function of the Human Cervical Spine**

The human spine is a structure of multitudinous function. It is a system that spans a considerable portion of the body, allowing a large degree of multi-axial flexibility while simultaneously providing support to loads originating from the upper body [122]. The spine must allow these large multi-axial motions of the body while limiting pinching and deleterious stretching of the sensitive nervous and vascular tissues that pass within the peri-spinous region [70, 122]. Due to this fine functional balance, the spine is susceptible to grave injury and chronic affliction, and is therefore a primary candidate for biomechanical study.

### **1.2 Anatomy of the Human Cervical Spine**

#### **1.2.1 Geometry**

The basic building blocks of the spine are the rigid, bony vertebrae and the flexible intervertebral discs. Twenty-four vertebrae compose the flexible portions of the spine, further divided into the cervical (C1-C7), thoracic (T1-T12), and lumbar (L1-L5) regions. Inferior to these regions is the inflexible portion of the spine, composed of nine fused sacral and coccygeal vertebrae (Figure 1). Each region has a characteristic curvature in the sagittal plane. When viewed from the posterior, this curvature is “kyphotic” if convex, and “lordotic” if concave. Although not predicted by beam theory, these curvatures are believed to enhance axial

compression strength, flexibility, and lend additional shock-absorbing ability to the spine [16, 68, 88, 122].

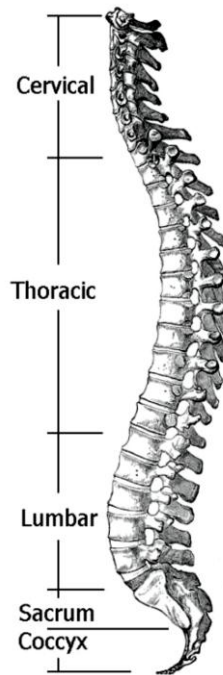


Figure 1: The entire spine with each region denoted. Variation in curvature from the lordotic cervical and lumbar regions to the kyphotic thoracic region is demonstrated (adapted from Gray's Anatomy [36, 124]).

As the superior portion of the spine, the cervical region is the sole bony support for the head. Originating from the relatively stiff thoracic region (characterized by rib attachment points), it allows a greater degree of flexibility than any other portion of the spine [122]. Copious flexibility provides greater aural and visual acuity, among other benefits [68]. Motion of the spine is measured along three primary rotational axes: the flexion and extension axis, lateral bending axis, and axial rotation axis (Figure 2). Total physiologic range of motion (ROM) of the cervical spine can reach  $89^{\circ}$  in combined flexion+extension,  $110^{\circ}$  in bilateral (combined left and right) bending, and  $196^{\circ}$  in biaxial rotation [122].

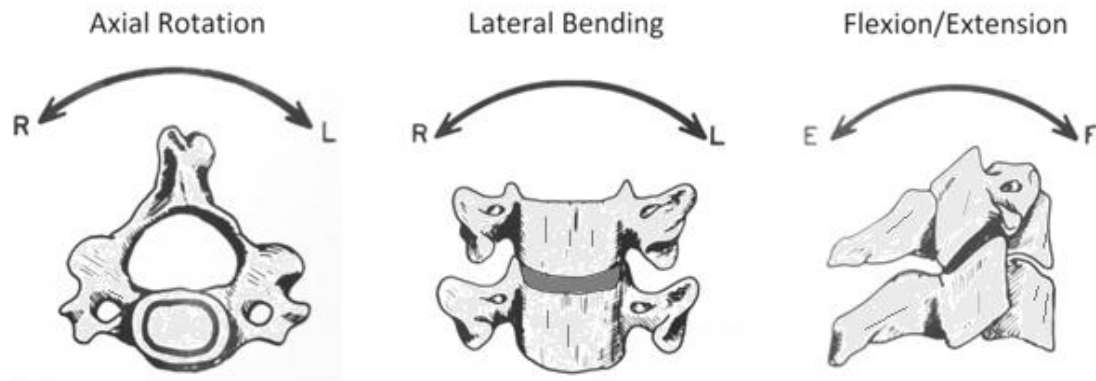


Figure 2: Bending axes of the spine (adapted from White[121]).

The cervical spine must accommodate this flexibility while simultaneously providing protection for the nervous tissues that pass within [122]. To accomplish this, the cervical spine is composed of two structures of distinctly different mechanical properties: the upper (C0-C2) and lower regions (C3-C7, Figure 3).

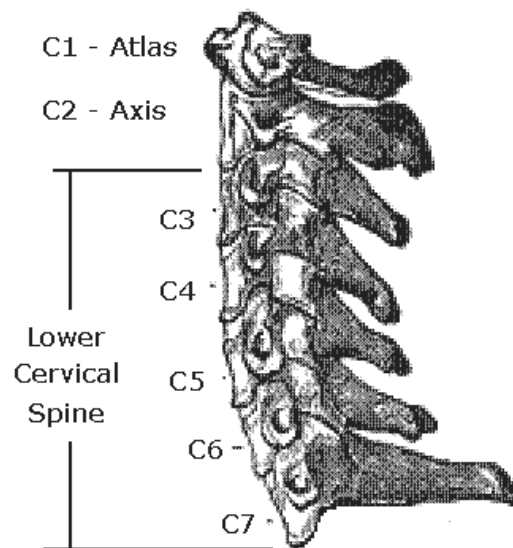


Figure 3: The full-cervical spine vertebrae, divided into the upper and lower regions. The occiput (C0) is not pictured (adapted from Gray's Anatomy [36, 124]).

### 1.2.1.1 Bony Tissue

The lower cervical spine is characterized by five relatively similar vertebrae. The vertebra is the stiffest member of the spine, and provides a shielded conduit for delicate tissues and attachment points for musculature [122]. External features of the vertebrae are composed

of dense cortical bone, filled with porous, truss-like trabecular/cancellous bone. This structure allows for a rigid structure while maintaining low overall density, and enables a nutrient path to the internal regions of the bone [70]. Figure 4 demonstrates a typical lower-cervical vertebra and important anatomical features.

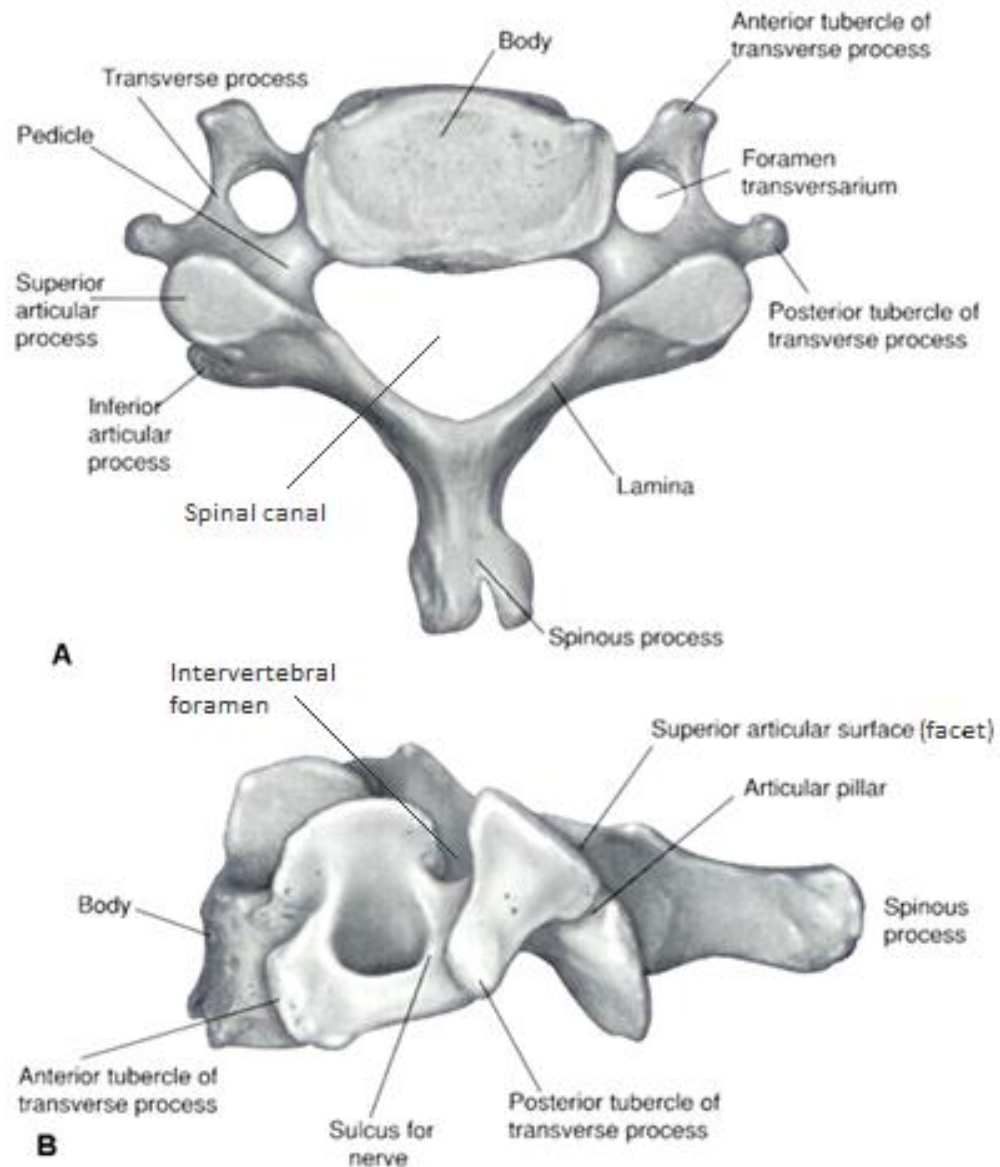


Figure 4: A typical lower-cervical vertebra, showing superior (A) and lateral (B) views (adapted from [www.ispub.com](http://www.ispub.com) [128]).

The most massive portion of the vertebra is the body. The body is the attachment point to the intervertebral discs, with these two components forming the anterior column. Vital vascular and nervous tissues pass through the spinal canal (containing the spinal cord), the intervertebral (neural) foramina, and the foramen transversarium in the cervical spine. The spinous processes and tubercles allow muscular attachment for provision of support and motion control [122]. The cervical spine uniquely contains unciniate processes, which are raised lateral ridges on the superior face of the vertebral body. These protrusions are believed to limit translational movements, which can apply detrimental shear stress to the spinal cord [122]. The vertebrae also support posteriorly-located, articulating cartilaginous surfaces, known as “facet” or “zygapophyseal” joints. The facet joints are comprised of bony protrusions covered with smooth cartilage pads that allow relative sliding to occur. Size of the facets ranges from 8 to 18 mm when viewed in the plane of the articulating surface [126]. Although the intervertebral disc is often the sole compressive load-carrying member, the facet joints aid in supporting the spine in extension and during large axial rotations and lateral bends [16, 87]. The lordotic curve is comparable to the alignment seen in extension, where the facets are engaged, which explains why the curved spine is better able to resist axial compression loading than the straight spine [16, 88].

The facet joints are oriented differently throughout the spine, according to the primary loading vector [65]. Due to these orientations, facet joints are partially responsible for creating coupled motions within the spine. Coupled motions are minor rotations around an axis orthogonal to the primary axis of rotation. For example, minor axial rotation naturally accompanies lateral bending (Figure 5) [19, 122].

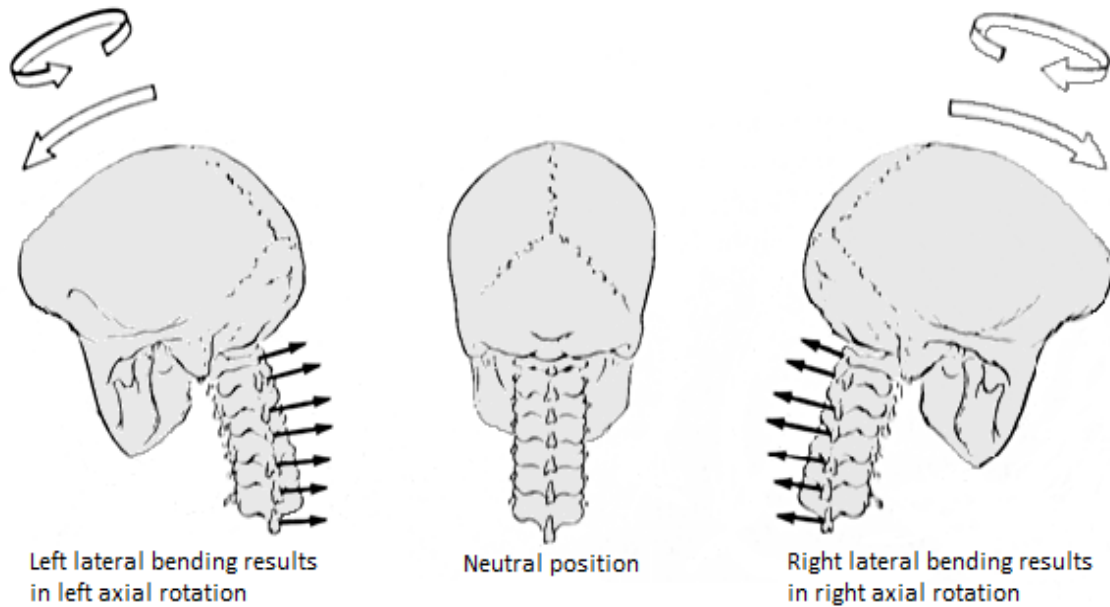


Figure 5: Demonstration of coupled axial rotation with lateral bending (adapted from White [122]).

In the primary bending modes, the lower cervical spine allows a high degree of flexibility in the axial rotation (approximately 40% of total cervical motion), lateral bending (72%), and flexion+extension (44%) directions [22, 82]. Most of the total cervical axial rotation occurs within the upper cervical spine, particularly the junction between the C1 and C2 vertebrae, which is commonly known as the “atlanto-axial joint”. Unlike the nearly repetitive lower cervical portion, the upper cervical portion is comprised of vastly differently shaped vertebrae, and is supported entirely by sliding cartilaginous surfaces, as it lacks intervertebral discs. The C2 vertebra, or axis, is inferiorly similar to the C3-C7 bodies, but possesses the dens, or odontoid process, a prominent superior protrusion (Figure 6). The dens fits within the ring shaped C1 (atlas) vertebra, where it forms a pin joint between the anterior portion of C1 and the largest and strongest ligament in the cervical spine, the transverse atlantal ligament [24, 81]. This single joint allows approximately 55% of the total axial rotation in the cervical spine [22]. Correspondingly, the facets joints are oriented much more perpendicular to the axis of rotation than at other vertebral junctions, allowing free axial rotation [78].

The base of the skull, or occiput, is often considered part of the upper cervical spine and denoted as C0. As opposed to facet articulations, the occiput fits into a cartilage-lined, trough-shaped area on the superior face of the atlas. Split into two halves by the spinal canal, these sagittally-symmetric joints are known as the “occipital condyles”.

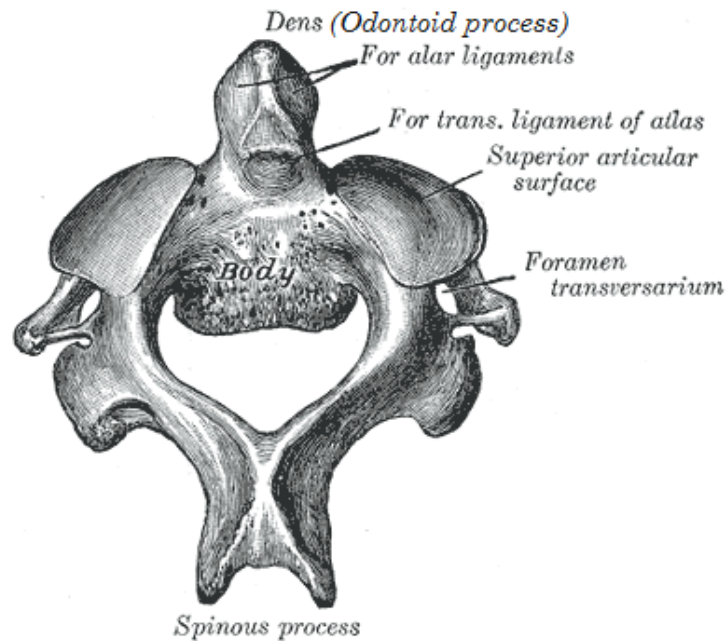


Figure 6: C2 (axis) vertebra, showing the prominent dens protrusion (adapted from Gray’s Anatomy [35]).

### 1.2.1.2 Neural Tissue

The cervical spine supports a complex network of neural tissue. Tissues contained within the vertebrae are of particular interest to those researching spinal biomechanics. These tissues include the spinal cord, the spinal ganglia, and the nerve roots. The spinal cord is the main path of information between the brain and the rest of the body and lies within the spinal canal. Nerve roots channel this information to anatomical regions and sprout from the spinal cord at each level of the cervical spine. These roots gain access to the body by passing through the intervertebral foramina bilaterally [68]. The spinal ganglia are swollen regions near the junction of the nerve roots and the spinal cord [68]. Despite having the largest cross-section of any tissue in the nerve-root structure, the ganglia lie directly within the narrowest regions of the

intervertebral foramina [83]. When measuring spinal ganglia and intervertebral foramina width at all levels between C2-C3 and C6-C7, previous studies have shown that the ganglia consume an average of 72% (range: 61-95%) of the available width of the intervertebral foramina in a healthy, neutral-posture spine. Repeating the same study while examining the height of the structures results in the ganglia taking 68% (range: 58-80%) of the available space [2, 28, 43, 51, 59, 83]. These spinal ganglia measurements neglect the presence of adipose and vascular tissues that must also pass through the intervertebral foramina, which further reduce the available space for the neural tissue [68].

### 1.2.1.3 Intervertebral Disc

The intervertebral discs are situated between the vertebral bodies of the lower cervical spine, allowing rotation and minor translation between the vertebral bodies. These discs can be dissected into the central nucleus pulposus, the circumscribing annulus fibrosus, and the inferior and superior cartilaginous endplates (Figure 7).

The healthy nucleus pulposus is a highly hydrated, gelatinous substance containing proteins such as proteoglycans and loose collagen. It appears barrel-shaped when viewed in the coronal or sagittal plane, and comprises approximately 25% of the cross-sectional area of the total cervical disc as viewed in the transverse plane [133].

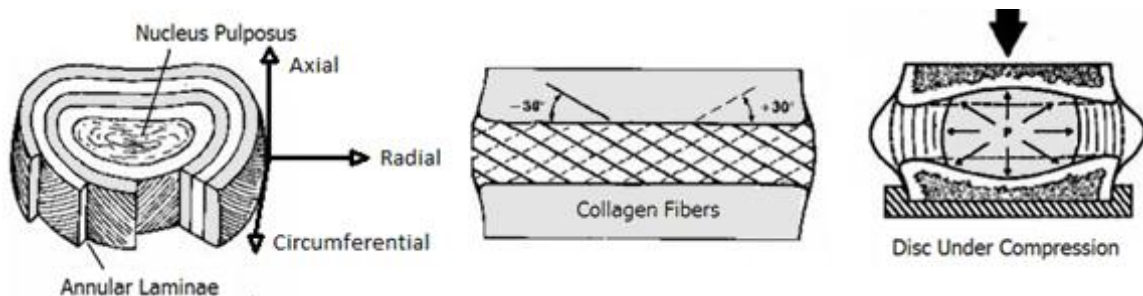


Figure 7: (Left) The composition and local coordinate system of the intervertebral disc. (Middle) Collagen fiber orientation on the periphery of the annulus. (Right) Hydrostatic pressure exerted by the nucleus when the disc is compressed (adapted from Joshi [48]).

Conversely, the annulus fibrosus demonstrates a system of approximately 20 oriented collagen-fiber reinforced laminae, similar to an angle-ply composite laminate [70]. The fibers vary in orientation along the radial direction, ranging from  $60^{\circ}$  (relative to the axial direction) at the exterior laminae, to  $45^{\circ}$  near the nucleus pulposus [70]. These fibers thread into the cartilaginous endplates near the center of the disc, and attach directly to the vertebral body at the perimeter via Sharpey's fibers [122]. The purpose of this arrangement is believed to provide two-fold benefits; the annulus can provide stiffness in the axial, transverse shear, and torsional shear loading directions, while simultaneously containing the nearly hydrostatic pressure generated within the nucleus pulposus due to axial loading [70, 122].

The cartilaginous endplate is a non-articulating divider between the inner intervertebral disc components and the vertebral bodies. Thickness of the cartilaginous endplate is approximately 0.6 mm in the central portion, increasing to roughly 1.2 mm at the perimeter [70, 90, 103]. The permeability of the endplate is vital, since much of the nutrient and hydration supply to the disc depends on passage through the endplate [70]. The endplate may also guard the disc from mechanical damage by providing a gradual decrease in stiffness relative to the rigid vertebral bodies [56, 70].

#### **1.2.1.4 Articular Cartilage**

Facet cartilage thickness varies greatly throughout the cervical spine. The lower region features relatively constant cartilage dimensions, rarely exceeding 0.5 mm in thickness [126]. In contrast, the current study has found the upper cervical facets contain cartilage in excess of 2 mm in thickness, with variance of over 1 mm across the articulating area (see section 3.1.1.1.3 Articular Cartilage). This additional thickness may be necessary to compensate for the loading and shock-absorbing ability that is provided by the intervertebral disc in the lower spine [132].

#### **1.2.1.5 Musculature**

The muscles of the spine may be divided into three groups: deep, intermediate, and superficial. The superficial muscles are the furthest exterior and generally largest [122]. These muscles may span across multiple vertebrae, and are responsible for most of the active motions of the spine [30, 68]. This is in contrast to the deep musculature, which is characterized by smaller muscles linking the adjacent transverse and spinous processes. These muscles are believed to be predominantly used for active stabilization of the spinal structure, supplementing the stiffening provided by the ligaments [68, 122]. The intermediate muscles provide for both stiffening and mobility.

#### **1.2.1.6 Ligaments**

Disregarding the intervertebral discs, facet joints, and connected musculature, the spine is still passively supported by ligaments. This ligamentous support is necessary, as the intervertebral discs are relatively compliant, and the musculature is not able to react quickly enough to provide adequate support in impact situations [85, 86].

Owing to differences in directional flexibility, the upper and lower cervical spines feature a vastly different ligamentous structure. The lower cervical spine is characterized by ligaments that are largely repetitive in both geometry and mechanical properties [71]. The posterior portions of the vertebrae are connected by the ligamentum flavum (LF) and the comparatively-minor interspinous (ISL) ligaments. The LF serves as a posterior wall for the spinal canal, as well as a shock-absorbing tether to prevent hyperflexion [45, 72, 122]. It is located a substantial distance from the intervertebral center of rotation, thus it undergoes relatively large strains during normal spinal movement. The LF must also maintain tension at low strains in order to prevent buckling into the spinal canal, where it could impinge on the spinal cord [72]. The facet capsule ligaments (FC) completely circumscribe the mating facet cartilage pairs. These

ligaments provide stiffness to the facet joints and contain the lubricating synovial fluid. At the posterior margin of the anterior column, the posterior longitudinal ligament (PLL) tightly adheres to both the anterior column and the intervertebral discs. Opposite the anterior column is the anterior longitudinal ligament (ALL), which is very similar to the PLL in appearance and mechanical characteristics (Figure 8) [7, 60, 92].

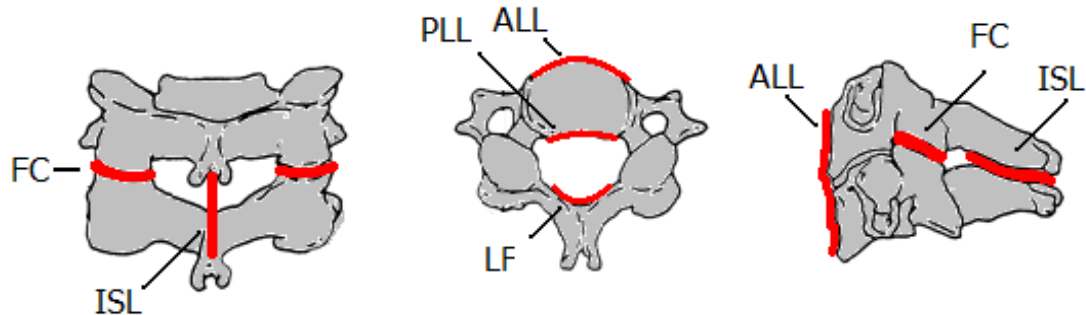


Figure 8: Ligaments of the lower cervical spine shown on a typical lower-cervical functional spinal unit (adapted from [www.uphs.penn.edu](http://www.uphs.penn.edu) [124, 129]).

Several ligaments of the lower cervical spine extend into the upper cervical region, although the geometries of these ligaments fan from a tape-like shape to a membranous structure. The membranous shape enables different mechanical properties, and can provide containment for important soft tissues such as the spinal cord [45, 115]. Construct stiffness of these ligaments is usually reduced relative to their inferior portions, allowing for further ROM [21, 71].

As previously detailed, the atlanto-axial joint is formed by the dens, ring of the atlas, and the transverse atlantal ligament (ATL). The ATL inserts into tubercles on the lateral masses of the atlas, and wraps across the posterior face of the dens, spanning approximately 20 mm [14, 62]. The ATL possesses a very large cross-section, measuring approximately 3 mm in thickness and 9 mm in height [14, 27]. Considering its role as an articulating member, the ATL is constructed of a stiff fibrocartilaginous tissue. Beyond its role in the atlanto-axial joint, the ATL possesses superior and inferior cruciform elements, which bridge the main structure of the ATL to the

occiput and inferior portion of the dens, respectively. These portions exhibit reduced cross-sections as compared to the main portion of the ATL, typically measuring 5 mm in width and 1.3-1.4 mm in thickness [134].

Owing to the primary mobility of the atlanto-axial joint, the upper-cervical ligamentous structure provides low resistance to axial rotation until reaching the endpoints of travel. This region of low mechanical resistance is commonly termed the “neutral zone”. Surrounding the atlanto-axial joint are the superior continuation of the ALL and the posterior atlanto-axial membrane, which is often considered a reduced stiffness perpetuation of the LF [68, 122]. Primary resistance to hyper-rotation is provided by the alar ligaments, which are shown in both physiologic and simplified functional form in Figure 9. The alar ligaments connect the lateral masses of both C0 and C1 to the superior tip of the dens. These ligaments are relatively short in relation to their thickness (2-2.6:1 length/thickness ratio) [22, 27], resulting in non-uniform collagen fiber recruitment over their cross-sections when resisting axial rotation [79]. Additional rotational restraint is afforded by the C1-C2 FC ligaments.

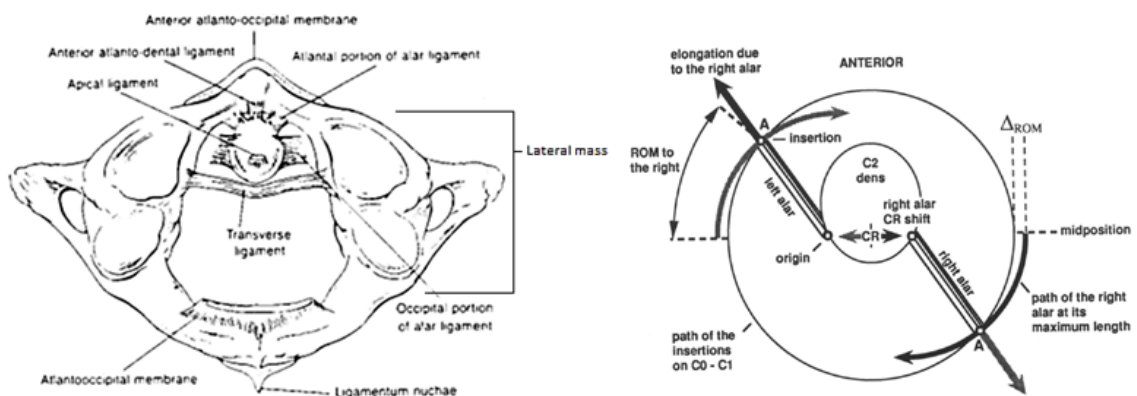


Figure 9: (Left) The anatomy and ligamentous support of the atlanto-axial joint (adapted from Panjabi [84]). (Right) A simplified model of alar restraint on atlantal and occipital axial rotation [22].

The trough-shaped atlanto-occipital joint (C0-C1) provides approximately 20 degrees of motion throughout flexion+extension, but is more constrained in the other directions [22, 78]. Ligaments present at this joint include the thin anterior atlanto-occipital membrane, which

extends from the anterior arch of C1 to the opening at the base of the skull (the foramen magnum). This is mirrored about the coronal plane by the posterior atlanto-occipital membrane. Further support is provided by capsular ligaments circumscribing the occipital condyles [117].

The upper cervical spine has many ligaments that span from C2 directly to C0. These are generally concentrated around the spinal canal. Extending from the superior tip of the dens directly to the anterior margin of the foramen magnum is the apical ligament. This ligament resists upward loading of the head, but is only found in approximately 70-80% of the population [113, 134]. Sharing a similar insertion point on the dens, the occipital portion of the alar ligaments attach to the lateral edges of the foramen magnum. These alar ligaments are similar to the atlantal alar ligaments but are larger in cross-section [26, 27].

Forming the anterior wall of the spinal canal is the tectorial membrane (TM). This thick (1.0 mm) and tough membrane runs between the base of the dens and the anterior lip of the foramen magnum. The TM seals the spinal canal from the anterior portion of the spine. The TM provides stiffness to the cervical spine, intimately attaches to the dura mater (outer sheath) of the spinal cord, and prevents the tip of the dens from protruding into the spinal canal [115]. This membrane is also in close contact to the cruciate portions of the ATL [115].

Several other ligaments of more minor mechanical function are found within the cervical spine. These ligaments are often absent from the cervical spine, or have been found to provide very little mechanical support. The more commonly acknowledged of these ligaments include the accessory axial-occipital, atlanto-dental, lateral atlantal-occipital, intertransverse, ligamentum nuchae, supraspinous, transverse-occipital, and Barkow ligaments [26, 47, 67, 112, 114, 116, 117].

### 1.2.2 Materials

The mechanically-predominant constituent tissues of the spine are collagen (types I and II), elastin, hydroxyapatite, and amorphous calcium phosphate. Other materials found in significant amounts include water, cells, and proteins such as glycolipids, proteoglycans, and other varieties of collagen [70]. These materials do not feature the same degree of mechanical strength and stiffness as the predominant structural materials, but still serve important roles as supporting matrix materials. This is in addition to biological functions such as delivery of nutrients and removal of metabolic wastes [70].

Collagen is a fibrous material composed of protein. The varieties of collagen are distinguished by their polypeptide makeup and anatomical placement. Type I collagen is the dominant variety of collagen in bone. This species of collagen also represents the major fiber component of tensile-loaded tissues such as tendons and ligaments [70]. Type II collagen is more common in articular cartilage, where it supports compressive and shear loading [70].

Elastin is a fibrous protein that allows a large reversible strain and excellent fatigue properties [37]. It is typically found in tissues that require considerable stretching, such as skin. It is also an important component of ligaments, allowing large, recoverable deformation [60].

Hydroxyapatite  $[\text{Ca}_{10}(\text{PO}_4)_6(\text{OH})_2]$  and calcium phosphate  $[\text{CaHPO}_4]$  are highly rigid, inorganic minerals. These compounds comprise the majority of bony tissue [70].

### 1.2.2.1 Bone

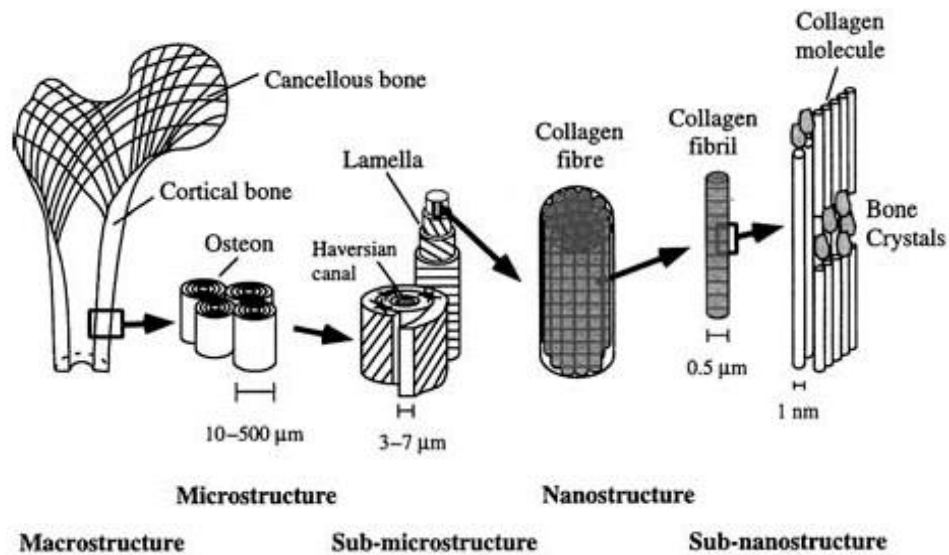


Figure 10: The structure and constitutive materials of bone [100].

Bone is a very complicated structural composite, adapted to provide strength and stiffness in the predominantly-loaded direction while minimizing weight [55]. Composed of both inorganic and organic phases, bone holds the ability to self-adapt to loading conditions, optimizing structural efficiency. Approximately 75% of bone mass is inorganic hydroxyapatite and calcium phosphate. These minerals are largely responsible for giving bone its characteristic stiffness [70]. The remaining bone mass is an organic osteoid matrix. Further analysis of the osteoid matrix reveals that 90% of its substance is Type I collagen, with the balance amorphous ground substances (Figure 10) [70].

This composite structure of bone leads to variable and anisotropic properties at the micro-scale, often designated the “tissue” level. However, the anisotropy of bone is greater when examined at larger length scale (the “apparent” level). This phenomena is due to bone being composed of two tissues, cortical (dense) and trabecular (porous) bone. The classification of bone into these types is dependent upon density, anatomic location, and the prevalence of Haversian systems [70].

In general, cortical bone comprises the external shell of individual bones. Cortical bone density is relatively constant, varying between 1.3 and 1.8 g/cc [70]. Haversian canals are the primary method of synthesis, where minerals are deposited along the interior wall of pipe-like structures [70]. Mechanical properties are dependent on the orientation of these Haversian systems. Commonly reported elastic moduli for cortical bone range from 9-20 GPa, these values being highly dependent on anatomical location and testing direction of specimens [96].

Trabecular bone forms the internal support of bones and is highly porous. The typical trabecular structure is truss-like with the supporting members being rod shaped spicules or “trabeculae”. In denser trabecular bone the trabeculae become plate-like in shape [55]. Trabecular density (0.1-1.3 g/cc) and elastic modulus (3.2-10 GPa) are highly variable [70, 97]. Haversian systems are largely absent from trabecular bone, as bone is typically deposited directly on the surface of the trabeculae [70]. Lacking Haversian systems, anisotropy is less intrinsic to the tissue and more influenced by the predominant orientation of the trabeculae. This orientation is typically aligned with the predominant loading vector seen by the bone [55]. Despite this anisotropy, previous research has revealed a reliable correlation between bone density and mechanical properties such as modulus, yield strength, and ultimate strength [12, 96].

#### **1.2.2.2 Intervertebral Disc**

As anticipated by its laminar structure, the annulus fibrosus demonstrates anisotropic mechanical properties. Elastic modulus in the circumferential direction (in the direction of collagen reinforcement) under tensile loading has been found to vary between 28-78 MPa, while stiffness in the radial direction is 100 times less [42, 53].

Due to its hydration level (90% water by weight) and generally unorganized collagen presence, the nucleus pulposus is often considered an isotropic, nearly incompressible material,

with Poisson’s ratio near 0.5 [70]. Modulus is very low, reported at 0.04 MPa in tensile loading [70]. The cartilaginous endplate is predominantly loaded in compression, with reported moduli in the range of 0.3-2 MPa and a Poisson’s ratio of 0.3 [33, 64, 70, 74, 101, 105].

However, in the context of spinal mechanics, the entire intervertebral disc must be examined. This approach accounts for the interaction of tissues, geometry, and the effects of nuclear swelling pressure. Swelling pressure is a difficult variable to experimentally replicate, as it is dependent on loading history, hydration, and specimen degeneration [70]. Acknowledging these obstacles, publications exhibit large variance in mechanical properties (Table 1).

Table 1: Mechanical properties for multiple loading conditions on the cervical intervertebral disc and anterior longitudinal ligament complex [69].

<b>Loading</b>	<b>Mean Stiffness</b>	<b>Stiffness Range</b>
Compression (N/mm)	492	57-2060
Anterior shear (N/mm)	62	12-317
Posterior shear (N/mm)	50	13-169
Right lateral shear (N/mm)	73	17-267
Flexion (Nm/deg)	0.21	0.05-0.65
Extension (Nm/deg)	0.32	0.06-0.78
Right bending (Nm/deg)	0.33	0.09-0.91
CCW torsion (Nm/deg)	0.42	0.23-0.93

### 1.2.2.3 Articular Cartilage

Articular cartilage is an extremely complex multiphase material. It exhibits properties like that of porous media, where hydration level is loading dependent. Resulting hydraulic pressure is theorized to provide 80-95% percent of cartilage's stiffness under dynamic loading [5]. Furthermore, this hydraulic support is variable throughout the thickness due to nonhomogeneous material properties [70].

This inhomogeneity may be resultant of cartilage's necessity to resist both compressive impact and surface shear loadings. To accomplish these objectives, cartilage exists in three mechanically-functional layers: the superficial, middle, and deep zones (Figure 11) [70]. This variable structure is evident upon examination of the collagen fiber alignment. The superficial layer is composed of the highest amount of collagen (85% of dry weight). It is also the most hydrated level (75-80% water by total weight). In the superficial layer, the collagen fibrils are organized parallel to the articulating surface. Accordingly, the collagen is better able to resist tears originating from the tangential and compressive stresses seen at the articulating surface. The superficial region is typically considered to account for 10-20% of the total cartilage thickness [70].

Continuing to the middle zone, the cartilage fibrils become more erratic in orientation. The collagen content lessens with proteoglycans filling the balance. The middle zone is the thickest region, comprising 40-60% of the total cartilage thickness. The deep layer shares a similar collagen and proteoglycan composition with the middle zone but features a different collagen arrangement. The collagen fibrils in this layer are woven together to form large bundles, which are primarily perpendicular to the subchondral surface. This orientation allows the collagen to anchor to the subchondral bone, preventing delamination of the entire cartilage pad [70].

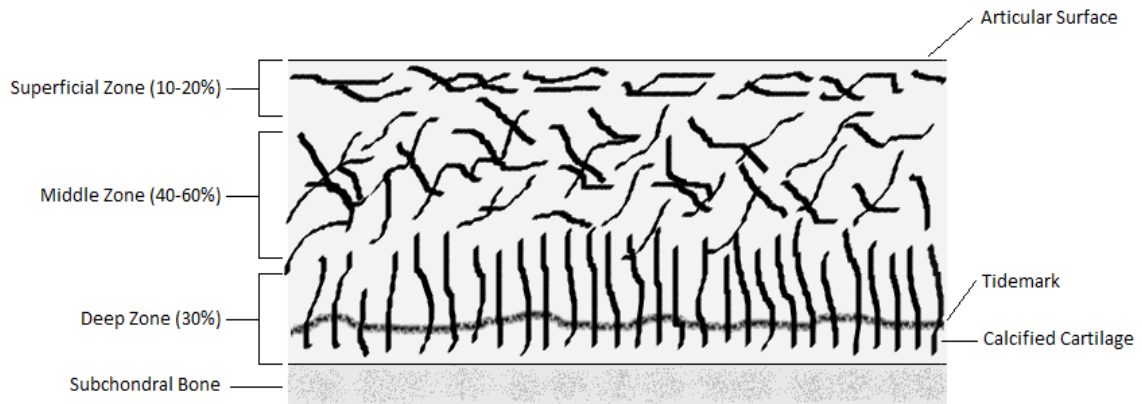


Figure 11: The three-layer composition of cartilage (adapted from Mow [70]).

Contact properties for sliding articular cartilage pairs are typically regarded as frictionless or with a very low friction coefficient ( $\mu = 0.01-0.1$ ) [11, 57]. Lubricity is provided by the high hydration level of the cartilage as well as secreted synovial fluid [54, 120]. Despite the low friction, shear loading is still present at the articulating surface. This can largely be explained due to mechanical interlocking of the mated cartilage pads. Cartilage is a fairly low modulus material under quasistatic loading (0.5-1 MPa), particularly at the highly hydrated superficial layer. This low surface modulus allows the opposing cartilage pads to indent each other under compressive pressures, which can be quite large (2-12 MPa) [5]. Accordingly, cartilage must allow large strains (experimentally measured up to 14%) without sustaining damage [5]. Higher loading rates feature more hydraulic support, creating much stiffer moduli (10 MPa) [4, 5, 11]. In all loading cases, Poisson's ratio of cartilage is fairly high (0.3-0.4) [11, 120].

#### 1.2.2.4 Musculature

Muscle tissue has a vastly different set of properties depending on whether it is active or not. Previous studies have reported that muscles within the spine can support a maximum stress of 480 kPa when active [95]. When the muscles are passive, the tissue still retains approximately 30-60% of its active stiffness [122]. Some of the muscles more intimately intertwined with the

spine, such as the “deep” variety (see section 1.2.1.5), must then be accounted for in mechanical analysis of the osteoligamentous structure even when the tissue is passive.

### 1.2.2.5 Ligaments

Table 2: Previously reported quasistatic stiffness values for cervical ligaments [11, 17, 57, 81, 89, 106, 131, 133, 135].

Ligament	Stiffness Range (N/mm)
Alar	21.2-80.1
Anterior atlanto-occipital	13.6-16.9
Anterior longitudinal	16-98.8
Apical	27-28.6
Facet capsule	29.2-62
Flaval	11.6-88.1
Interspinous	5.3-7.7
Posterior atlanto-occipital	5.7-7.1
Posterior longitudinal	10.8-145.4
Tectorial membrane	7.1-9
Transverse atlantal	85.8-141.3
Vertical cruciate portions of transverse atlantal	19-21.6

The ligaments have been repeatedly found to influence spinal biomechanics more than any other tissue [11, 86, 135, 136]. Unfortunately, ligaments demonstrate extreme interspecimen variability in mechanical properties. Much of this variance is due to intrinsic mechanical properties, not external dimensions [71, 106]. Due to the nonlinear mechanics of ligaments, reported stiffnesses may fluctuate simply based on the load range analyzed (Table 2). Ligaments also display extreme loading-rate dependence. Stiffnesses have been shown to increase by 200-700% when altering strain rates from quasistatic (<0.05/s) to higher rates (>10/s). Failure strain also decreases with increased strain rate, only allowing 2-30% of the elongation possible at lower strain rates [45, 106].

Ligaments feature a typical composition of approximately 70% water, with the main structural integrity contributed by type I collagen and elastin [70]. Most ligaments present a collagen to elastin ratio of 11:1, while the ligamentum flavum contains a very large amount of

highly deformable elastin (1:2 collagen to elastin ratio), forming the most elastin-dense tissue in the human body [7, 85, 122]. Ligaments are generally able to stretch beyond the failure strain of the embedded collagen, due to the fibers' ability to move within the matrix substance. This motion is aided by the crimped or coil spring-like shape of the relaxed collagen fibers, which can extend greatly when loaded. This characteristic is also believed to allow ligaments to return to their relaxed length after large, non-injurious strains [70]. Ligaments are typically considered tension-only members, although the alar and transverse atlantal ligaments are often analyzed as three-dimensional structures due to their short and thick aspect ratios [49, 79, 134, 135].

### **1.3 History of Human Cervical Spine Experimental Biomechanical Testing**

The goal of biomechanical testing is to simulate a realistic loading case on living tissue. However, this goal is extremely difficult to reach. Thus, compromises are nearly always present in biomechanical testing.

In the context of human spine testing, most experimental protocols fall within two domains: "*in-vivo*" (living subject) and "*in-vitro*" (cadaveric subject). Each of these methods has specific strengths and weaknesses, which must be weighed depending on the desired data outcome. Furthermore, the specimens tested can be divided into "intact" or "injured" cases.

While the human body has seen little change during the modern era of biomechanics, testing methodology has evolved to reflect available technology. Early experimenters could not benefit from modern computer-controlled loading and measurement devices. For instance, motion data were previously captured by manually measuring distances between carefully chosen reference points [21, 86]. Modern technology now allows digital sampling of vast numbers of reference points at extremely rapid rates. Software is available to parse and process the large datasets that are created. Weight and pulley-type loading systems have been replaced

with force-feedback, computer-controlled apparatuses [86, 124]. These loading mechanisms allow a specimen to be dynamically cycled throughout its test range, yielding additional measurement points. They also simplify the task of preconditioning, which can reduce the hysteresis often observed in biological tissue testing [7, 60]. Thus, the same essential experiments conducted decades ago still provide novel data with modern execution; the complexity of biomechanical systems is so immense that modern technology is often required for accurate characterization. Furthermore, biodiversity is great enough that reiterating previous experiments with a larger number of test subjects may create more viable datasets.

### **1.3.1 *In-vivo* Testing**

*In-vivo* testing may be further subdivided into controlled laboratory experiments and examination of clinical data. Laboratory experiments allow researchers to specify testing conditions, but the experiments are limited to non-injurious scenarios in humans. Clinical facilities can provide data concerning injury prevalence and sequelae, but they offer little information regarding the specific loadings required to produce the injuries.

*In-vivo* experimentation presents the most realistic specimens, but places severe limits on the types of loading and the ability to instrument the specimen for data acquisition. It is simply neither legal nor ethical to risk injury to patients or volunteers. This generally restricts *in-vivo* experimentation to slow, controlled ROM tests. These tests may entail gently moving the spine throughout the physiologic range of axial rotation, lateral bending, flexion, and extension, either with external manual manipulation or the muscular control of the test subject. Data collection is typically constrained to non-invasive means such as radiographs (X-ray, etc) or fluoroscopy [108]. More risky experiments have been conducted (high speed inertial loadings,

etc), although basic safety risks and the corresponding unavailability of test subjects limit the number of these experiments [44].

### **1.3.2 *In-vitro* Testing**

Testing of cadaveric human specimens allows a much wider breadth of collectible data and potential scenarios to be examined. Repeatability is greatly eased with the use of mechanical loading devices. However, there is still typically large variability in results due to interspecimen mechanical characteristics. Application of sensors and other measurement devices is far less limited, although there is a danger of the measurement devices creating artifact by interfering with natural physiologic mechanics.

Although the biomechanical similarities between fresh tissue and thawed frozen tissue has been shown [127], accurate replication of physiologic loadings is formidable. Simulating muscular control is extremely difficult, owing to the complexity of the muscular system and the physiologically-dispersed attachment to the bony tissue [70]. Even gravitational loading on the head is difficult to reproduce considering the potential misalignment of the spine relative to the gravitational force vector.

To mimic the physiologic response of tissues it is ideal to replicate a physiologic injury in loading type and magnitude, while considering environmental factors such as temperature and hydration [111]. Levels of temperature and hydration are especially pertinent in the testing of soft tissues. For example, porcine spinal ligaments have been found to fail at a 50% larger force when temperature was reduced from body temperature (37.8°C) to room temperature (21.1°C) [7, 91].

Unfortunately, some tissues undergo extremely rapid degradation *post-mortem*. The nervous tissue is a primary example of tissue that is extremely difficult to test *in-vitro*.

Demyelination of the spinal cord proceeds rapidly *post-mortem* [130]. It is also very difficult to maintain the layer of cerebrospinal fluid surrounding the spinal cord, which is critical to accurate simulation of cord impingement [38].

### **1.3.3 Intact Testing**

Specimens exhibiting no pre-existing injuries or debilitating conditions are referred to as “intact”. In the context of *in-vitro* cervical spine testing, this usually designates an osteoligamentous complex with no ligamentous injuries, vertebral fractures, degenerated or injured intervertebral discs, or extraneous ossification such as osteophytes or intervertebral fusions. This condition also excludes the presence of any implanted prostheses.

### **1.3.4 Injury Testing**

Injury testing can be further divided into operations that test a previously existing injury and those that simulate an injury. Experiments where an injury is artificially induced furnish the benefit of providing a control for each specimen. In this scenario, a specimen can be tested in the intact state, be subjected to injury, and then have the experimental regimen repeated post-injury. Due to large interspecimen biodiversity, it is greatly favorable to be able to use a specimen as its own control. However, there are certain injuries and conditions that are unable to be replicated without disturbing other tissues of a specimen. Due to the complex construction of the spine, isolating a tissue for injury simulation is difficult. Accordingly, a specific tissue may have to be removed from the specimen-at-large and tested and injured separately. This poses a difficult problem, as this tissue will likely no longer be able to be

reinserted into the gross specimen for full-spine testing. However, analytical methods (such as finite element modeling) allow a virtual solution to this quandary.

#### **1.4 History of Cervical Spine Finite Element Modeling**

The primary benefit of finite element (FE) models is adjustability. Conditions can be simulated virtually that would be extremely difficult to replicate in an experimental setting. These conditions can reflect injuries, degenerative changes, and/or biodiversity in either tissue geometry or mechanical properties. The drawbacks of an FE model are potentially few, but the quality of the model is paramount to enable accurate computational predictions of actual physical data. Ideally, the desired model measurables will be validated with identical experimental measures under the same conditions [118]. For example, due to the complex load sharing in the human cervical spine, accurate model prediction of gross measurements such as vertebral ROM may not be indicative of accurate stress/strain predictions at the tissue level. Accordingly, if accurate prediction of tissue-level loadings is desired, accurate assessment of these tissue properties is prerequisite to model creation. In the same vein, adequate mesh resolution is necessary to ensure minute tissue characteristics are captured [13]. Ideal finite element size can be determined by comparing models of varying resolution, this process designated “model convergence”. Convergence criteria are met when the predicted data are relatively unaltered between models of differing resolution. Elements modeling the more sensitive tissues, typically soft tissues subject to large strains, require the greatest degree of scrutiny [6, 124]. Returning to the concept of “gross” versus “tissue-level” measures, finer measures such as strain energy are preferential to solely-relying on total ROM and other coarse measurements for convergence studies.

Parameterization of various model properties allows rapid tuning, which expedites the calculation of an iterative solution. This is a useful technique for studying tissues that serve as redundant supports to the cervical complex. A typical application of parameterization is in the cervical ligaments. Multiple ligaments work in concert to constrain the motion of the spine, resulting in complex load sharing. Experimentally determining the exact force applied by each individual ligament is extremely difficult. However, iteratively altering stiffness, preload, and toe length may offer a unique solution when all loading cases (axial rotation, lateral bending, etc) are considered [11, 124, 135-137].

Myriad FE models of the human cervical spine have been developed since the 1980s [11]. Most of those models are limited to either the upper (C0-C2) or lower (C3-C7) cervical spine [11, 49, 73, 93, 125, 136]. The few existing full-cervical (C0-C7) FE models were generally developed to examine dynamic whiplash-type pathology, offering poor resolution to detect more subtle biomechanical characteristics at quasistatic loading rates [49, 131]. Many of the models simplified the intervertebral discs and ligamentous structure. Those models rarely attempted to replicate the membranous characteristics of the upper cervical ligaments, particularly the tectorial membrane. In addition, few of the models were validated with in-house experimental data. Accordingly, subtleties (such as transient response in a ROM test) are ignored due to the difficulty in obtaining such values from literature.

## **1.5 Cervical Spine Affliction**

Injuries affecting the cervical spine must be handled with great care, since the spinal cord and nerve roots are closely intertwined with the cervical vertebrae. The application of excessive stresses to the neural tissues can cause apoptosis (cell death), demyelination (nerve sheath damage), and other deleterious effects that reduce or disable the ability of the tissues to

carry signals between the brain and body [77, 130]. These conditions result in either temporary or permanent neural deficiencies, such as paresis (motor control loss), or paresthesias (sensory disability) [83, 130]. The security of the neurological tissue can be compromised by either damage to an individual vertebra, or misalignment and/or extraneous motion between adjacent vertebrae. Proper alignment of the walls of the spinal canal is necessary to prevent myelopathy (impingement of the spinal cord). Preservation of the intervertebral foraminal space is critical to prevent radiculopathy (impingement of the nerve roots). Both of these conditions may be caused by injury to the cervical ligaments, which can alter the natural alignment and ROM of the cervical vertebrae [29, 39, 76]. As the primary motion-stabilizing structures in the cervical spine, ligaments are responsible for shielding other tissues, such as the intervertebral discs, from carrying too much of the burden of this stabilization. Thus, injuries to the ligamentous structures may allow excessive stresses/strains to be generated in the other cervical tissues [46]. These ligamentous injuries are often the result of vehicular accidents, head impact trauma, or even excessive stretching during exercise [23, 85].

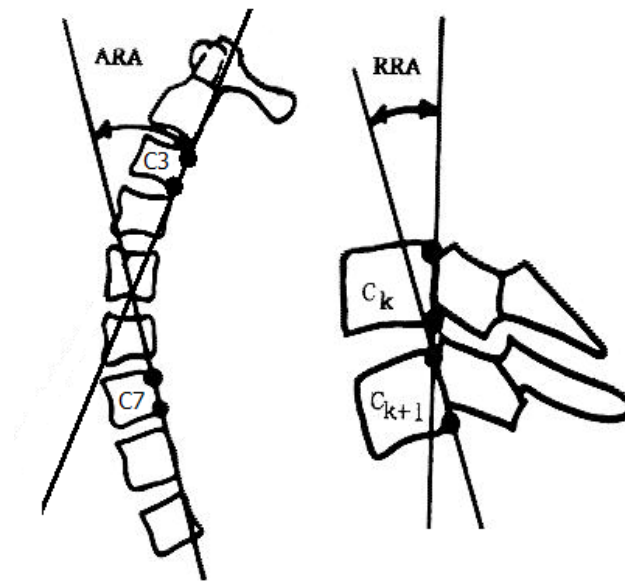


Figure 12: A typical method for evaluating vertebral rotations from radiographic imaging. (Left) Total lordosis angle of the lower cervical spine is measured. (Right) Relative intervertebral angle at a single functional spine unit is measured (adapted from Harrison [39, 124]).

As soft tissue injuries, ligament injuries are not readily apparent from typical radiographs, which poorly visualize low density tissue [104]. However, simple radiographs taken at the endpoints of a ROM test can detect hypermobility of the vertebrae, which may indicate soft tissue injuries (Figure 12). However, the effect of each specific soft tissue injury on ROM is still vague, making these tests currently unreliable for detecting specific injuries [29, 50]. Magnetic resonance (MR) imaging can detect some soft tissue injuries, but is only 70% reliable in detecting ligamentous injuries [20, 34]. Furthermore, MR imaging is often neglected for cost reasons [20, 63]. The correct diagnosis of soft tissue injuries that potentially allow harm to the nervous tissues is critical given the risk of severe and/or permanent neurological impairment [23, 41].

## **2 SPECIFIC AIMS IN RESPONSE TO CERVICAL SPINE LIGAMENTOUS INJURY**

Many clinicians have attempted to construct guidelines specifying the segmental kinetic and kinematic effects of soft tissue injury such that diagnoses can be performed via radiography. However, these guidelines often feature conflicting information, as they are largely based on clinical experience rather than rigorous biomechanical study [8, 20, 34, 40, 41, 63, 104]. Given the potential of permanent neurological deficit or death due to incorrect cervical soft tissue injury diagnosis and/or treatment, quantification of the relevant biomechanical parameters that are altered due to soft tissue injuries is critically needed. Thus, the overarching goals of this study are to enhance diagnosis and enlighten the biomechanical sequelae of cervical soft tissue injury. Accomplishment of these goals will ultimately reduce patient risk, increase treatment efficacy, and lower costs [8, 20, 40, 41, 66]. In pursuit of these objectives, the following specific aims were proposed:

### **2.1 Specific Aim 1: Develop a converged and validated computational finite element model of the intact full-cervical (C0-C7) osteoligamentous complex.**

This model will quantify the stresses, strains, and ROM experienced by the healthy, cervical, osteoligamentous spine during physiologic motion. The FE modeling approach allows analysis of metrics not readily measured *in-vivo*, such as internal tissue stresses and strains. FE modeling also enables the global effects of individual tissue property modifications to be analyzed.

The model will represent the merging of a previously validated and converged lower cervical (C3-C7) portion and a newly-generated upper cervical (C0-C2) portion [124]. Computed tomography data will define geometry and material properties will be obtained from published literature. Pursuant to enhancing soft tissue injury diagnosis and analysis of radiculopathic etiology, ROM and change in intervertebral (neural) foramina height and width resulting from pure moments applied in the axial rotation, lateral bending, flexion, and extension directions will be quantified. These data will define the baseline characteristics for the healthy spine. Comparison of the intervertebral foramina dimensions to those of the encapsulated neural tissue will be performed. This method has been shown to be efficacious by previous studies that have investigated mechanically-induced radiculopathy [2, 28, 43, 51, 59, 83].

Experimental, *in-vitro*, cadaveric data will be used to validate the model predictions under identical, pure-moment loading conditions. Validation metrics will include ROM for each vertebra, cortical strain, and facet contact pressures in the atlanto-axial joint. Convergence will be accomplished by analyzing ROM, facet contact forces and pressures, and strain energy from three models of varying mesh resolution.

## **2.2 Specific Aim 2: Experimentally determine the mechanical properties of ligaments commonly injured in whiplash-type trauma.**

To the author's knowledge, no study has measured the mechanical properties of individual ligaments both prior to and post-injury [110]. Given the near ubiquitous acceptance of ligament properties as the most important parameter in determining spinal kinematics, the experimental measurement of post-injury ligament mechanical properties is of paramount importance.

Emphasis is placed on analyzing the ligamentous-hyperstrain injuries that often result from whiplash-type trauma (hyperextension and hyperflexion), due to the prevalence of these accidents and the societal cost of associated treatment [110]. Cadaveric alar, anterior longitudinal, and flaval bone-ligament-bone preparations will be tensioned to induce permanent deformation (apparent damage) at strain rates (10/s) reported to exist during traumatic injury [60]. These ligaments are chosen as they have a predominating influence on cervical mechanics and are commonly injured in whiplash-type trauma [46, 62, 85]. The post-damage quasistatic stiffness and toe region length (displacement from resting position to extension at 10 N) will be compared to the pre-damage state for each ligament specimen.

### **2.3 Specific Aim 3: Modify the intact cervical spine finite element model to include injured ligament mechanical properties in order to simulate the effects of ligamentous injury on the cervical spine.**

Specific insults will be computationally modeled at the C5-C6 space, the most common level of injury [46, 85]. Models will reflect partially-injured (hyperstrained) and fully-injured (transected) ligaments. The specific injuries to be modeled include: 1) partial FC injury, 2) full FC injury, 3) partial FC and ALL injury, 4) full FC and ALL injury, 5) partial LF and full ISL injury, 6) full LF and ISL injury, 7) partial FC, ALL, LF, and full ISL injury, and 8) full FC, ALL, LF, and ISL injury. The FC ligaments will be modeled to sustain corollary damage with the ALL, and the ISL will be modeled to have totally ruptured when the LF sustains damage. This injury pathology is consistent with results from clinical and experimental studies of whiplash-type injuries [46, 85]. Full and partial unilateral alar ligament injury in the C0-C2 region will also be modeled to examine impact scenarios that include traumatic twisting of the head and neck [62, 79].

Validation of the full-injury models will be accomplished via *in-vitro*, cadaveric spine testing using serial ligament-sectioning techniques. Experimental validation of the partial-injury models is impossible due to the method of partial ligament injury (see Specific Aim 2). However, it is hypothesized that the FE-predicted kinematic behavior of the partial-injury models will be very similar to the full-injury models. All injury models are hypothesized to exceed ROM of the intact case (see Specific Aim 1). Measurement of the intervertebral foramina height and width will be compared to the intact case. It is predicted that the additional ROM afforded by ligamentous injury will substantially reduce the size of the foramina.

#### **2.4 Specific Aim 4: Use the aforementioned intact and damaged cervical models to enhance the diagnostic procedure.**

The resultant ROM from the injuries listed in Specific Aim 3 will be compared under all three loading directions. It is anticipated that each specific injury will demonstrate a unique kinematic signature that is capable of being detected via clinical ROM testing. These results will be organized into a decision-making flowchart that will allow healthcare practitioners to systematically diagnose specific injuries using radiographic images taken during clinical ROM testing. A supplemental table of the injuries that may result in neural impingement or potentially damaging stresses and/or strains to the intervertebral disc and facet cartilage will also be produced. These parameters will be compared to the normal, intact (physiologic) standards to determine if cervical stabilization is necessary.

### **3 EXPERIMENTAL METHODOLOGY AND DATA**

Efforts in pursuit of the four specific aims have yielded substantial supportive data. The newly-generated upper cervical FE model is capable of accurately predicting ROM and facet contact forces (Specific Aim 1). The model has been validated to both externally-published data as well as results from the experimental ROM testing of six cadaveric, full-cervical spines (see Table 3 for entire cadaveric specimen pool). The FE model has also successfully demonstrated adequate mesh resolution through a comprehensive convergence study.

Experimental research of injured ligament properties (Specific Aim 2) has demonstrated the efficacy and feasibility of the tensile testing and injury induction protocols. A total of 7 alar, 14 ALL, and 12 LF ligament specimens have been tested, showing significant reductions in stiffness for the ALL ligaments after injury, and significant increases in post-injury toe region length for all ligament types.

The FE models have predicted the ROM subsequent to ligamentous injuries (Specific Aim 3). These predictions have shown that ROM of the injured models exceed those of the intact cases, and ROM of the partial ligamentous injury models are very similar to those of the full-injury models. Five cadaveric, full-cervical spines have been experimentally tested with serial ligament-sectioning at the C5-C6 level, replicating the FE-modeled full ligamentous injuries. Four cadaveric spines have been tested to replicate right alar ligament injuries. These experimental ROM data are in agreement with the full-injury FE model predictions.

Injuries resulting from hyperextension (FC and ALL injury) show very similar ROM to that of the hyperflexion injury case (LF and ISL injury) under clinically-relevant combined flexion+extension loading. However, the axial rotation and lateral bending loading directions show largely different ROM between the two injury cases. This supports the hypothesis that each specific injury results in a unique kinematic signature capable of detection through clinical ROM testing (Specific Aim 4).

The following chapters further detail the work that has been performed in pursuit of the goals of this project.

Table 3: Cadaveric cervical spine specimen pool. The far right column describes the tests run on each individual specimen.

<b>Gender</b>	<b>Age (yr)</b>	<b>Height (cm)</b>	<b>Weight (kg)</b>	<b>Test</b>
Male	34	188	79	Ligament tensile
Male	45	180	62	Intact ROM, ROM with sectioned ligaments, Ligament tensile
Female	55	175	75	Intact ROM, ROM & radiographs with sectioned ligaments, Ligament tensile
Male	56	193	82	Intact ROM, ROM & radiographs with sectioned ligaments, Ligament tensile
Female	58	168	73	Intact ROM, ROM & radiographs with sectioned ligaments, Ligament tensile
Male	59	183	91	Intact ROM, ROM & radiographs with sectioned ligaments, Ligament tensile
Female	64	170	74	Clinical-CT scanned for FE model geometry
Male	65	173	70	Intact ROM, Ligament tensile
Male	69	175	64	Micro-CT cartilage thickness measurement

### **3.1 Intact Cervical Spine Finite Element Model (Specific Aim 1)**

#### **3.1.1 Intact Cervical Spine Finite Element Model Generation**

The full-cervical spine FE model created in this study is the incorporation of a pre-existing fully validated and converged lower cervical portion (C3-C7) and a newly-generated upper cervical portion (C0-C2) [124]. However, in the interests of computational efficiency, the model was subsequently broken into separate upper (C0-C3) and lower (C3-C7) sections for analysis. Considering the approximate 200 hour runtime for a typical full-cervical simulation, this technique was deemed vital to accommodate the limitations of the available computational hardware. To preserve continuity between the sections, modeling techniques such as material properties, approximate mesh resolution, and ligamentous representation were retained. ABAQUS (ABAQUS V6.9-EF2, Dassault Systèmes Simulia Corp, Providence, RI) was used for model generation and execution of subsequent analyses.

##### **3.1.1.1 Generation of Geometry**

###### **3.1.1.1.1 Bony Tissue**

Bony geometry for both the upper and lower cervical FE model portions was obtained from a clinical-resolution, quantitative computed tomography (qCT) scan of a single, fresh-frozen, female cadaveric spine (age: 64 yr, height: 170 cm, weight: 74 kg). CT measurement yielded 0.5 mm transverse resolution with 1.0 mm slice thickness. Hounsfield attenuation values (HU) were used to segment the CT dataset into cortical (>350 HU) and trabecular regions (<350 HU and/or circumscribed by cortical bone) with Amira digital image analysis software (Amira V4.1.1, Visage Imaging, Carlsbad, CA). Due to the coarse resolution of the CT measurement, delicate features of the cortical region, such as the transverse foramen, were not captured by

automated thresholding functions. Cortical bone in these regions was manually segmented. Amira was used to generate smoothed surface geometries from the segmented images.

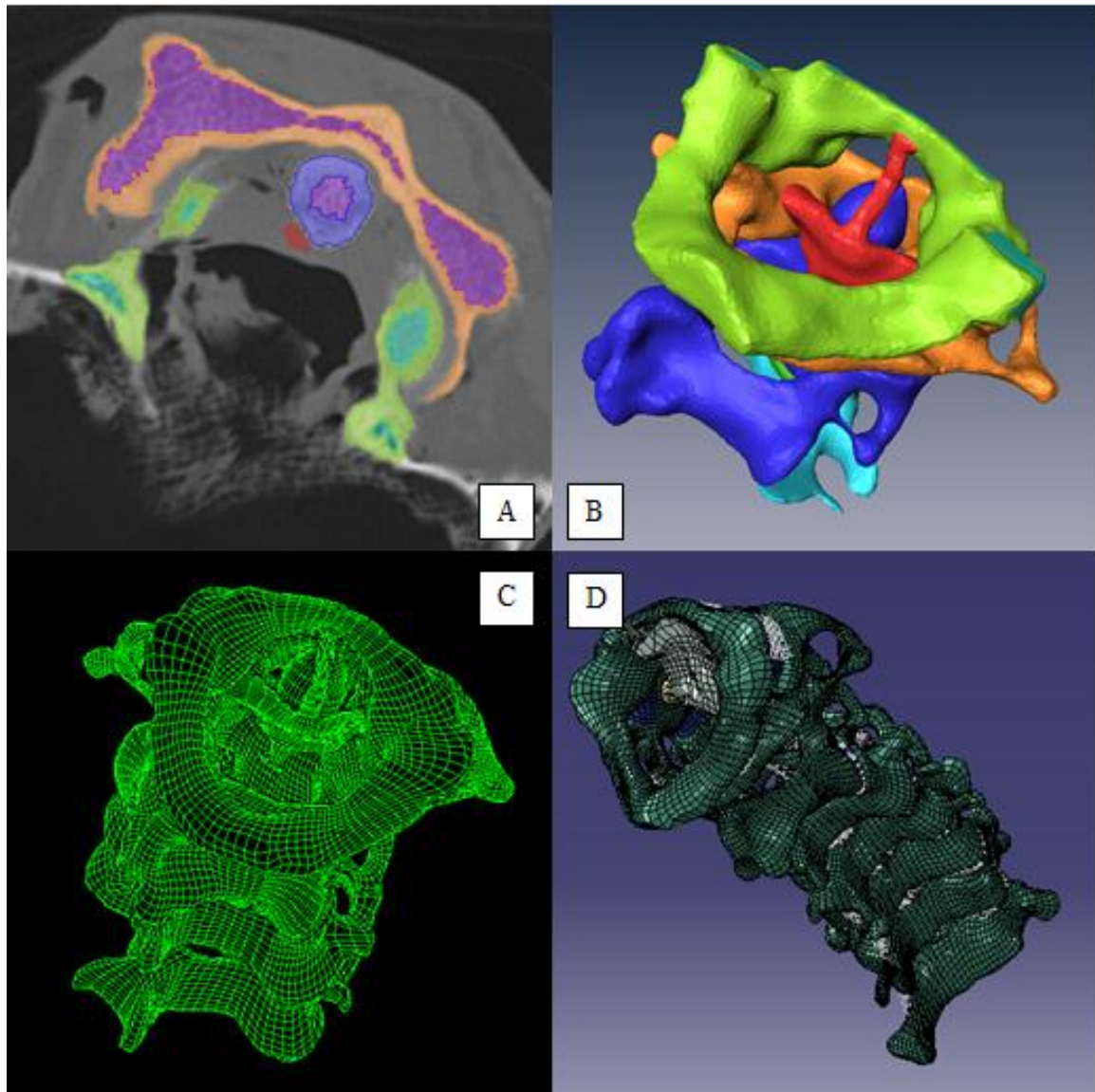


Figure 13: Synthesis of the finite element model proceeding from top left: (A) Segmented voxels are assigned to specific tissues in Amira. (B) Smoothed surfaces are generated from the segmented voxels in Amira. (C) Meshed elements are projected in TrueGrid to surfaces created in Amira. (D) Solid and shell elements are imported into ABAQUS, where spring elements and articular cartilage are added. Note the axial rotation of C0 and C1 in figures B and C, and its subsequent reduction in figure D after reorientation (see section 3.1.1.1.5 Model Orientation).

The surfaces were imported into TrueGrid (TrueGrid V2.3.0, XYZ Scientific Applications, Livermore, CA) for three-dimensional hexahedral meshing. Standard integration, first-order, 8-noded elements were specified for all solid tissues (type: C3D8). Elements assigned to cortical

bone regions were monitored to ensure thickness was approximately equal to the cortical thickness determined via qCT. Emphasis was also made to ensure high resolution at surfaces where articular cartilage would be placed. A custom-written Matlab program (Matlab V7.11.0.584 (R2010b), Mathworks, Natick, MA) classified each trabecular element based on the average Hounsfield density of the enveloped voxels. In this manner, each trabecular element could be sorted into one of ten discrete density bins, and assigned tailored mechanical properties based on the average density of the bin [96]. Verification of the code was accomplished by manually measuring the density of 50 randomly selected regions in Amira and ensuring the elements contained within were assigned to the correct density bin.

Independent nodes were created on the superior bony endplate surface of C3, C4, C5, and C6. Similar nodes were constructed on the inferior bony endplate surfaces of C2 and C7. These nodes were bound to the entire surface using ABAQUS “tie” constraints. In a similar fashion, the entire exterior surfaces of C0 and C1 were constrained to nodes located near their theoretical centers of physiologic rotation. These nodes allowed the application of loading or boundary conditions to the individual vertebrae. They also facilitated the measurement of vertebral rotations and translations.

#### 3.1.1.1.2 Intervertebral Disc

Generation of the upper-cervical model necessitated the construction of only one intervertebral disc, at the C2-C3 level. The external surface was constructed using existing bony geometry as anatomic landmarks. Annular bulge was estimated from existing literature and measurements taken during dissection [73, 124]. A barrel-shaped surface was created in Amira to define the nucleus, which compromised 25% of the area of the disc cross-section as viewed in the transverse plane (Figure 14). The annular and nuclear portions of the disc were then meshed concurrently with TrueGrid.

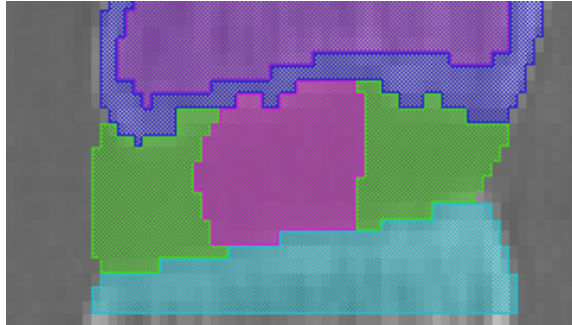


Figure 14: Sagittal view of the segmentation of the intervertebral disc, showing annulus (green) and nucleus (pink).

A custom-written Matlab code was used to disperse 2-noded, tension-only, nonlinear spring elements (type: SPRINGA) throughout the annulus, replicating collagen-fiber reinforcement. These elements were arranged in 9 concentric rings, emulating the lamellar character on the annulus (Figure 15). Radially-varying element angles were chosen to closely match the collagen fiber arrangement seen in the healthy annulus. The cartilaginous endplate was extruded from the inferior face of the C2 vertebral body, to the central thickness of 0.6 mm.

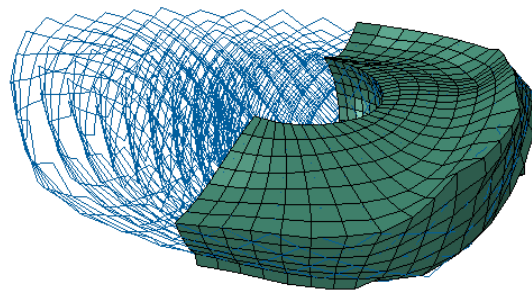


Figure 15: Finite element model of the annular ground substance (green) and collagen fibers (blue).

#### 3.1.1.1.3 Articular Cartilage

A three-layer arrangement was used to model the articular cartilage, allowing the elastic modulus to vary between superficial, mid-substance, and deep (subchondral adjacent) layers. The three-layer model could not be used at the C2-C3 facet interface due to the extremely thin cartilage structures (0.3 mm typical thickness). These facets were instead modeled using only the deep and superficial layers. These multi-layer structures, in conjunction with accurate

cartilage thickness representation, have yielded more accurate predictions for facet contact pressure than the more simplified cartilage models used in most FE analyses [102, 124].

Cartilage thickness was experimentally measured with micro-computed tomography ( $\mu$ CT) (Scanco  $\mu$ CT 80, Scanco Medical AG, Brüttisellen, Switzerland) at evenly-spaced discrete intervals across the articulating face (9-15 points, depending on surface area). Prior to scanning, the specimens were placed in saline for 12 hours to reach physiologic hydration. Scanning was then accomplished in air, which was necessary to visualize the superficial surface, as it has very similar radiation attenuation to saline. Hydration was maintained by placing saline-soaked gauze in the scanning vial. A pilot study verified that this method preserved physiologic hydration throughout the scanning time (approximately 4 hours). Cartilage thicknesses of two other specimens were also measured for comparison by depth-probing with a scalpel blade, yielding similar results to the  $\mu$ CT-scanned specimen. The efficacy of the scalpel-probing method was proven by repeating measurements on the  $\mu$ CT-scanned spine, where less than a 0.1 mm difference was found between the two methods.

The  $\mu$ CT cartilage measurements were taken from a fresh-frozen male cadaver (age: 69 yr, height: 175 cm, weight: 64 kg). This spine was of a different size and gender than the spine used for bony tissue modeling, necessitating an adjustment to cartilage thickness before replication in the model. A gender factor of 69% was disseminated from the literature [132], which was combined with a scale factor 77% (comparing anterior-posterior vertebral length at C1 and C2), resulting in a thickness reduction to 53% ( $69\% \times 77\%$ ) of the  $\mu$ CT-measured value. Cartilage was then extruded in ABAQUS along the vectors normal to the subchondral surface element faces. Extrusion thickness was varied to correspond to the thickness found at the discrete  $\mu$ CT measurement points. Adjacent regions were averaged in thickness at boundaries, producing a smoothly-varying articular surface. Validation of the gender/vertebral size scaling

technique was accomplished by comparing the extruded cartilage thickness to the qCT-measured space between subchondral surfaces. These measurements proved to be nearly identical. For example, the actual gap between the subchondral surfaces at the atlanto-axial facets measured 1.90 mm while the scaling method predicted a cartilage thickness of 1.99 mm (Figure 16).

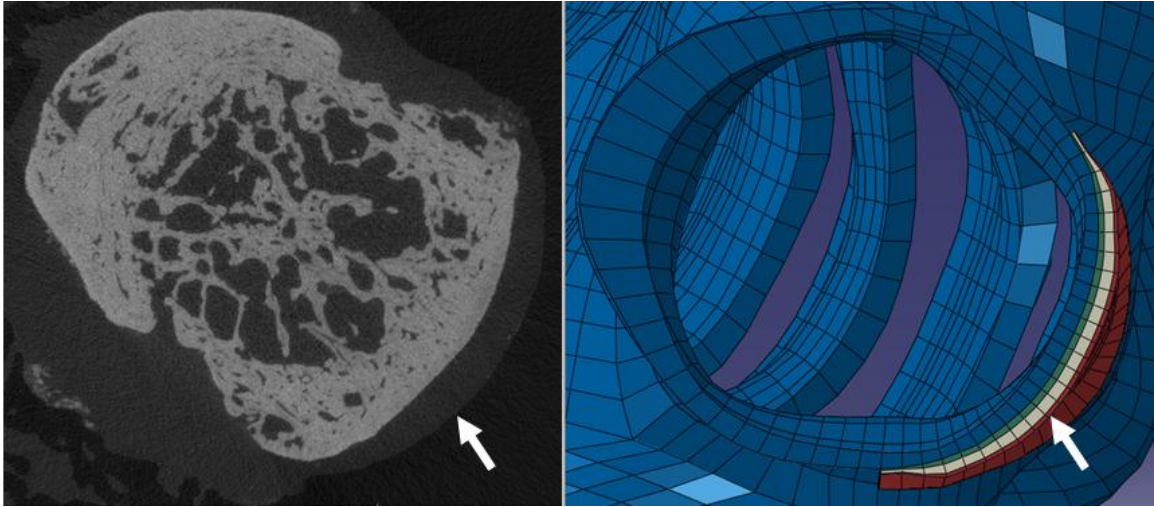


Figure 16: (Left) Arrow highlights articulating cartilage on the dens as imaged via  $\mu$ CT. Cartilage thickness was measured at 3-5 points across the width of the cross-section. (Right) Cartilage at the same anatomic location as modeled in ABAQUS. Note the three-layer arrangement, shown in green (deep), white (mid), and red (superficial) colored elements. The blue colored elements denote cortical bone.

#### 3.1.1.1.4 Ligaments

Ligaments were modeled by 2-noded, tension-only, nonlinear spring elements (type: SPRINGA). Modeled ligaments and membranes included the alar (atlantal and occipital), anterior atlanto-occipital, anterior longitudinal, apical, facet capsule, flaval, interspinous, posterior atlanto-axial, posterior atlanto-occipital, posterior longitudinal, tectorial, and transverse atlantal.

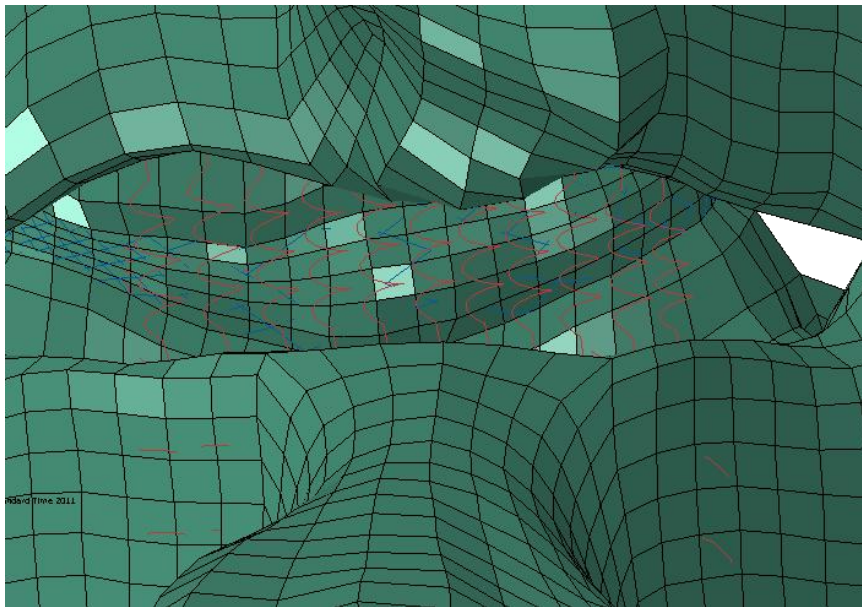


Figure 17: Example of the dispersed spring elements (red) used to model the physiologic width of the ligaments. The flaval ligament is shown.

Multiple parallel springs were attached directly to the cortical bone nodes, allowing force to be distributed across the attachment region (Figure 17). Between 1 and 12 springs were used depending on the cross-sectional size and shape of the ligament, with the exception of the tectorial, transverse atlantal, and upper cervical facet capsule ligaments. Pilot FE data revealed the kinematic importance of maintaining ligamentous attachment around the entire circumference of the upper cervical facet joints. Accordingly, closely-spaced spring elements (54 at C0-C1 and 43 at C1-C2, per side) were used to represent the facet capsular ligaments for the upper-cervical model (Figure 18). A custom-developed Matlab program was written to disperse these elements evenly around the facet circumference.

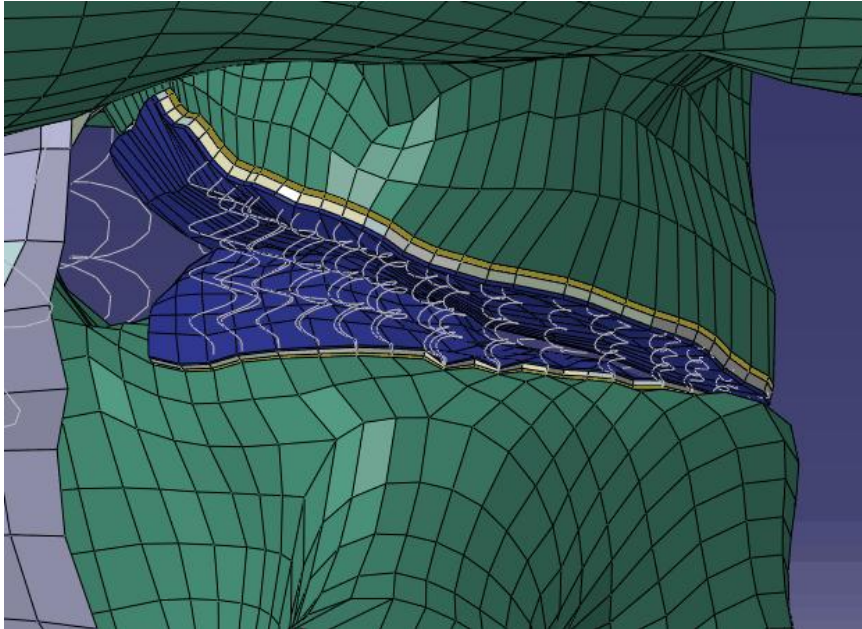


Figure 18: The peripheral dispersion of the facet capsule ligament spring elements (white).

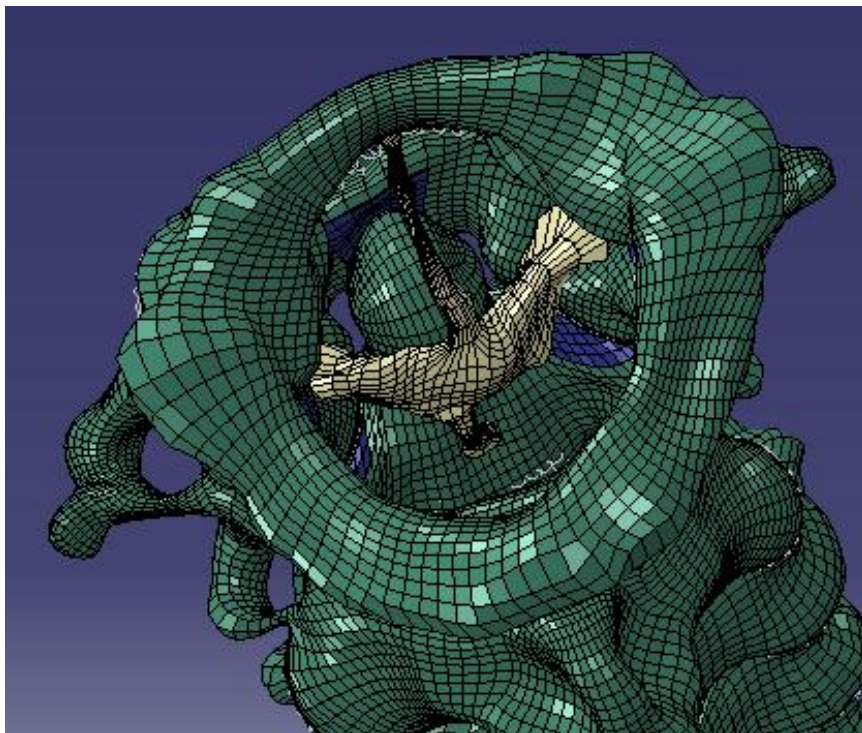


Figure 19: Solid element (tan) representation of the transverse atlantal element.

The three-dimensional mechanical loading of the transverse atlantal ligament precluded the application of spring element representation. Instead, the ATL was modeled with solid hexahedral elements (Type: C3D8, Figure 19).

The tectorial membrane serves as a divider between the atlanto-axial joint and the spinal canal. Accordingly, it necessitated construction by elements able to model membrane structures while allowing for large deformations. Reduced-integration shell elements were chosen to meet these requirements (type: S4R).

Both the ATL and TM were formed from surfaces manually created with the Amira segmentation tool. Bony anatomic landmarks were used in conjunction with measurements from dissection and existing literature to segment voxels allocated to these tissues. TrueGrid was then used to create representative elements.

#### 3.1.1.1.5 Model Orientation

The cadaveric specimen used in the creation of the model was CT-scanned with the atlanto-axial joint at  $32^{\circ}$  of left axial rotation. This geometry was imported into ABAQUS where boundary conditions were applied to rotate the occiput and atlas to a neutral position. This reference position was established with a time-explicit solver, which was better able to avoid the computational complications associated with the overpenetration of adjacent surfaces experienced immediately following model generation. Stiffness of the tectorial membrane was reduced to 1% of its physiologic value to ensure that it did not induce deformation of the underlying ATL or bony tissues. For similar reasons, spring elements representing ligamentous connection between the axis and atlas were temporarily removed. Care was also taken to avoid placing compressive forces on the cartilage. The ATL was given normal material properties in order to constrain the atlas to turn around a physiologic center of rotation. After rotation, the new nodal coordinates were specified as the reference configuration with the aid of a code developed in Matlab. In this manner, a stress and orientation neutral reference configuration could be obtained without causing any unwarranted deformation of the tissue geometry.

### 3.1.1.2 Material Properties

#### 3.1.1.2.1 Bone

Given the difficulty in determining the primary Haversian system orientation in the vertebrae and corresponding directional material properties, cortical bone was modeled as an isotropic material. Linear-elastic properties were specified, with a modulus of 11000 MPa (Table 4). Trabecular bone generally demonstrates more anisotropy [18], and thus was modeled as transversely-isotropic and linearly-elastic. The primary ( $E_3$ ) modulus was oriented along the superior-inferior axis, according to the predominant trabecular orientation in the spine [70, 124]. This primary modulus was calculated from qCT-measured density using the following equation (Equation 1: Calculation for modulus from CT density):

$$E_3 = 6.68 * \rho_{CT} - 94$$

where  $E_3$  (MPa) is the primary modulus, and  $\rho_{CT}$  (HU) is the qCT-measured density [98]. This modulus was then re-evaluated to provide shear and transverse dilatational moduli (Equation 2: Calculation of transverse and shear moduli):

$$E_1 = E_2 = 0.345 * E_3$$

$$G_{13} = G_{23} = E_3 / 2.6$$

$$G_{12} = E_1 / 2.6$$

where the transverse ( $E_1, E_2$ ) and shear moduli ( $G_{12}, G_{13}, G_{23}$ ) are based on the primary modulus ( $E_3$ ) [98, 124].

Table 4: Material properties for cortical and trabecular bone in the upper-cervical portion of the finite element model.

<b>Bone Type</b>	<b>Average Density (HU)</b>	<b>Standard Deviation (HU)</b>	<b><math>E_3 = \text{Primary Elastic Modulus (MPa)}</math></b>	<b><math>E_1 = E_2 = \text{Transverse Elastic Modulus (MPa)}</math></b>	<b>Poisson's Ratio</b>
Cortical	1108.09	351.01	11000	11000	0.3
Trabecular	389.52	270.4	193-9225	67-3182	0.3

### 3.1.1.2.2 Intervertebral Disc

The annulus fibrosus was generated by means of a solid-element ground substance reinforced with a nonlinear spring-element collagen fiber representation, following modeling techniques developed during the genesis of the lower cervical spine FE model [124]. The ground substance was modeled as an ABAQUS-formulated, second-order, reduced-polynomial, hyperelastic material fitted to uniaxial stress/strain test data [1]. Initial elastic modulus was specified at 0.25 MPa, increasing to 0.39 MPa above 30% strain. Poisson's ratio was set at 0.45. Fiber stiffness was parametrically varied depending on the length of the fibers. The nucleus pulposus was regarded as isotropic, with a modulus of 1.5 MPa and a Poisson's ratio of 0.499. The cartilaginous endplate was also modeled with isotropic properties (modulus: 1000 MPa, Poisson's ratio: 0.3). Swelling pressure was mimicked by specifying a thermal strain of 10% in the nucleus and 5% in the annulus [124].

### 3.1.1.2.3 Articular Cartilage

Articular cartilage was also represented by a second-order, reduced-polynomial, hyperelastic material (Table 5) [1]. Tabular stress and strain values were obtained from fitting of experimental, confined-compression data [52, 124].

Table 5: Articular cartilage material properties and thickness distribution used in the cervical finite element model. Two-layer cartilage structures used a 45% superficial, 55% deep thickness distribution.

Layer	Percent of Total Cartilage Thickness	Initial Elastic Modulus (MPa)	Poisson's Ratio
Superficial	20%	0.9	0.4
Mid-Substance	50%	1.8	0.4
Deep	30%	3.5	0.4

#### 3.1.1.2.4 Ligaments

The majority of the ligaments were modeled as tension-only spring elements. Nonlinear stiffness was specified in tabular fashion (Table 6). This method of specification allowed the model to demonstrate the nonlinear kinematics typically found in the cervical spine. Preload and stiffness were individually parameterized [124]. These ligament characteristics were intended to be tuned iteratively until a single set of properties could match the experimentally-measured response to moments in all three bending axes. This protocol implicated a unique, accurate solution for the ligamentous mechanical properties [11, 124, 135-137].

Table 6: Summary of the ligament properties used in the cervical finite element model. Average stiffnesses are reported due to the highly nonlinear properties of the ligaments.

Ligament	Number of Elements per Level	Stiffness (N/mm)
Alar (atlantal)	1	17.8
Alar (occipital)	1	17.8
Anterior atlanto-occipital	10	20.0
Anterior longitudinal	9	38.5
Apical	1	35.0
Facet capsule	1-54	29.4
Flaval	11	33.6
Interspinous	6	5.7
Posterior atlanto-axial	11	4.2
Posterior atlanto-occipital	11	7.3
Posterior longitudinal	9	20.8

The ATL and TM were modeled with shell and solid elements, respectively. Accordingly, stiffnesses of these ligaments were specified with elastic moduli rather than force/displacement data. Due to its relatively small deformation, the transverse portion of the ATL was modeled as a simple, linearly-elastic, isotropic material with an elastic modulus of 90 MPa. The vertical

cruciate portions of the ATL and TM experienced greater amounts of deformation, and were thus specified as second-order, reduced-polynomial, hyperelastic materials. The TM possessed an elastic modulus that varied from 4.3-12.5 MPa, while the ATL vertical cruciate was specified with a modulus varying from 8.3-24.7 MPa. These moduli were selected such that the overall stiffness of the structures would match the force/displacement data from the literature (as summarized in Table 2). Allowing this modulus adjustment limited the mechanical effect of slight inaccuracies in the specification of the soft tissue geometry (for example: over-sized cross-section); it ensured that the specified stiffness of the gross structure matched the experimentally obtained values.

### **3.1.2 Intact Cervical Spine Finite Element Model Convergence**

Previous FE models have shown that materials subjected to large strains are the most susceptible to convergence issues [6, 124]. Therefore, the soft tissues of the upper-cervical region were the focus of the convergence study. Specifically, the ATL, TM, and articular cartilage were designed to accept varying mesh resolution. This entailed the use of “tie” constraints for attachment to the bony geometry. This allowed mesh resolution to be adjusted without modifying the bony tissue. Given the aforementioned difficulty in orienting the model (see section 3.1.1.1.5 Model Orientation), it was more economical to modify the soft tissues of the oriented mesh while leaving the bony tissue mesh unperturbed. This is in opposition to externally generating and orientating an entire new mesh. This methodology also eliminated potential artifact resulting from the manual adjustments that were necessarily made to the mesh geometry during orientation.

The baseline model was designated as the “Medium Resolution” mesh density, and two other models were spawned from this configuration: “Low Resolution” and “High Resolution”.

The Low Resolution model was constructed by successive deletion of rows of elements from the Medium Resolution model (Figure 20). The remaining rows of elements were merged over the gaps created by the deleted elements. Care was taken to preserve elements forming the exterior geometry of the tissues, such that the shape of the soft tissues remained intact.

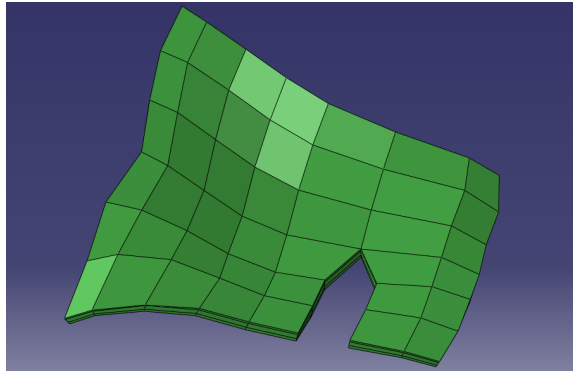


Figure 20: Method of lowering mesh resolution. A row of elements is deleted, and the adjacent rows are merged.

The High Resolution model was created by substituting a higher-resolution, second-order element type (C3D20, 20-noded elements) in the place of the articular cartilage and ATL elements. Using second-order elements, the effective mesh resolution of most tissues could be increased without changing the meshing topology [1]. A pilot study demonstrated the efficacy of altering mesh resolution with this method. The TM could not be converted to a higher-resolution element type since second-order “shell” elements were incompatible with hyperelastic materials such as that specified for the TM.

A 24.2% mesh resolution difference was achieved between the Low and Medium Resolution models (Table 7). Attempts to create models with lower soft tissue mesh resolution were unsuccessful due to the creation of severely distorted elements. This is a consequence of the need of the soft tissue geometries to smoothly mate to other contacting surfaces and the large finite element deformations typically encountered during analysis.

Table 7: Number of elements comprising soft tissues in the upper cervical FE model. (\*) denotes the use of second-order elements.

<b>Model Resolution</b>	<b>Articular Cartilage Elements</b>	<b>ATL Elements</b>	<b>TM Elements</b>	<b>Total Soft Tissue Elements</b>	<b>Total Degrees of Freedom</b>
Low	3294	2704	288	6286	351969
Medium	4347	3528	416	8291	357063
High	4347*	3528*	416	8291	479484

After a solution was obtained for the Medium Resolution model, the two convergence models were analyzed in identical fashion. Observed parameters included ROM, facet contact forces and pressures, and strain energy. Inter-model variance of less than 10% for each of these measures was desired to establish convergence.

### **3.1.3 Intact Cervical Spine Finite Element Model Analysis**

ABAQUS was used with a time-implicit solver for all simulations. For analysis of the upper-cervical section, pure-moment loads of 1.5 Nm were applied to C0 in the axial rotation, lateral bending, flexion, and extension directions. This moment magnitude has been previously found to move the upper cervical spine throughout its entire physiologic ROM without inducing damage [80]. The spine was caudally constrained at C3 with an ABAQUS “Encastre” boundary condition. These loading and boundary conditions were utilized for all subsequent models.

The lower-cervical model was used for measuring intervertebral foramina geometry and simulation of C5-C6 ligamentous injuries (see section 3.3 Ligamentous Injury Cervical Spine Finite Element Model (Specific Aim 3). Loadings were identical to those of the upper-cervical section, with the exception of moments being applied to C3, and constraints to C7. Due to the sagittal symmetry of the FE models and desire to increase computational efficiency, the models were only loaded unilaterally (left side) for the axial rotation and lateral bending cases. Thus, the reported bidirectional rotations are obtained by doubling the unilaterally-measured ROM.

Intervertebral foramina dimensions were measured by a procedure similar to that established by Panjabi *et al* [83]. Nodes corresponding to the points shown in Figure 21 were selected for the left foramen (the side most constricted by moment application) at the C5-C6 level (site of future injury-modeling simulations). A pilot study demonstrated that the contralateral intervertebral foramen underwent an identical constriction when moments were applied in the opposite direction. Foramen width and height during load application were compared to the same measurements in the unloaded configuration. The loaded dimensions of the foramen are reported as a percentage difference to the unloaded dimensions, to accentuate the dynamic change in size. Radiculopathy is assumed to occur when this percentage difference exceeds the amount of space left unoccupied by the average spinal ganglia (see section 1.2.1.2 Neural Tissue). For example, if the average ganglia consumes 72% of the available width of the intervertebral foramen, radiculopathy would be predicted if the foraminal width experiences more than a 28% reduction (32% reduction for foraminal height) [83].

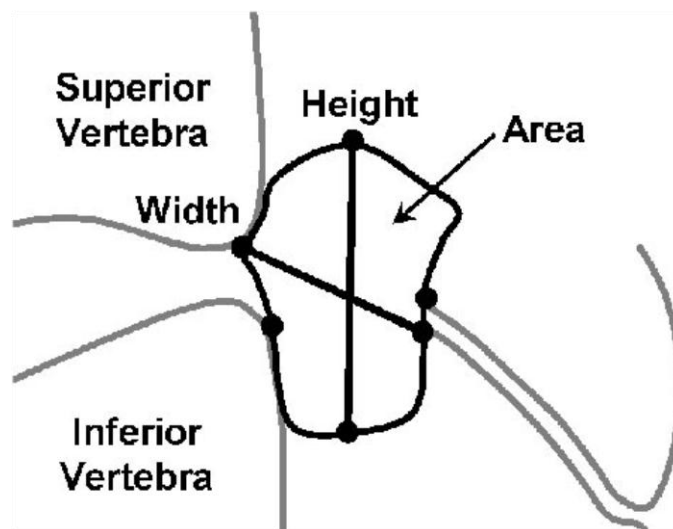


Figure 21: Approximate locations of the intervertebral foramina measurement points [83].

### **3.1.4 Intact Cervical Spine Finite Element Model Experimental Validation Method**

Cadaveric full-cervical (C0-C7) human spines were used to experimentally validate the model predictions. Measurements included ROM for each individual vertebrae, atlantal cortical strain, and atlanto-axial facet contact pressure resulting from the application of pure moments in the axial rotation, lateral bending, flexion, and extension directions.

Fresh-frozen cervical spines (n = 6) that exhibited no evidence of degeneration were harvested. Absence of degenerative issues was ensured by examining specimen serology reports, biplanar radiographs, and continual observation and measurement throughout specimen preparation. Musculature and other extraneous tissues were removed, with care taken to preserve the intervertebral discs and ligaments. Saline-spray hydration was utilized at 15 minute intervals during preparation and testing of specimens.

Superfluous portions of the skull were removed in order to provide clearance for an aluminum occiput fixture which was attached with three self-tapping cap-screws (Figure 22). This occiput fixture allowed attachment via a custom driveshaft to a torque-feedback stepper motor which could rotate the specimen through its physiologic ROM. An axially-sliding joint and two u-joints were incorporated into the driveshaft to allow freedom of motion in the off-axis directions (Figure 23).

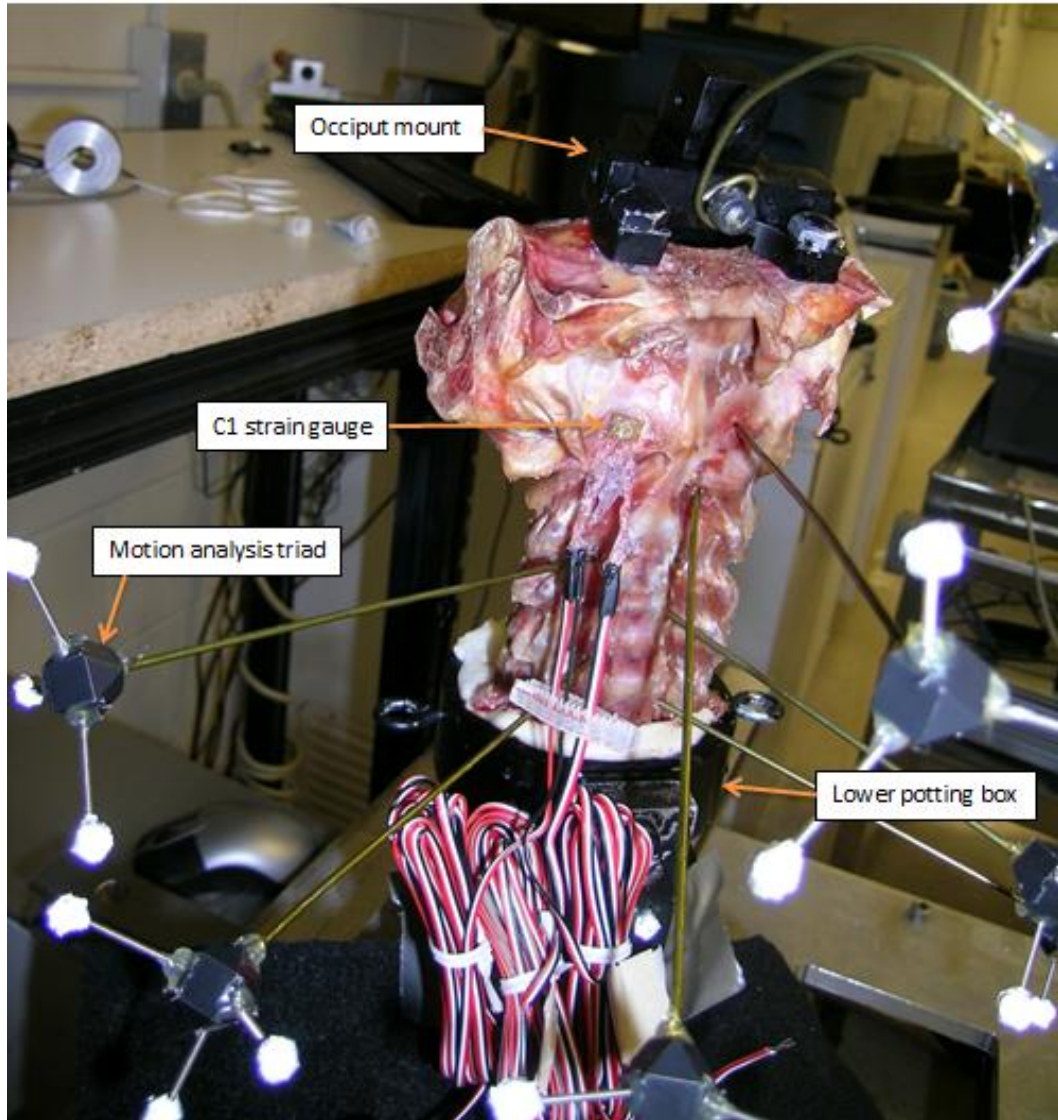


Figure 22: Experimental setup for full-cervical spine testing showing typical strain gauge placement. The load-cell is obscured by the strain gauge wiring.

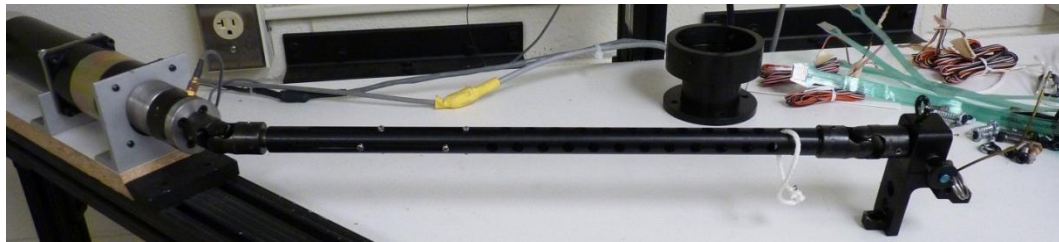


Figure 23: Custom driveshaft is shown attached to the stepper motor on left and occiput mount on right.

Mass minimization of the testing apparatus was identified as paramount to achieving a pure-moment loading condition. A pilot study demonstrated a detrimental artificial moment could be applied by the weight of a heavy testing apparatus. In response, the occiput mount,

driveshaft, and all other moving parts were optimized for weight savings. A pulley-hung counterweight was also used to minimize the weight applied to the specimen. The occiput mount, driveshaft, and necessary hardware were hung sans-specimen, only supported by the counterweight. The mass of the counterweight (362 g) was adjusted until the structure could sit in a free-floating equilibrium.

The caudal fixture held C7 in a poly-methyl-methacrylate (PMMA)-filled potting box mounted directly to a 5 kN/110 Nm load-cell (model MC3A-6, AMTI, Watertown, MA). The load-cell was attached to a custom-made, biaxially-sliding table to ensure an optimum starting alignment between the driveshaft and specimen. A 15° wooden wedge was attached to the inferior endplate of C7 with self-tapping screws in order to maintain a repeatable lordosis angle for all specimens (Figure 24).



Figure 24: A wooden wedge was affixed to the caudal face of C7 to maintain a physiologic lordosis angle when potted in PMMA.

The experimental apparatus was configured to apply either axial rotation, lateral bending, or flexion and extension moments. These loads were randomly ordered for each specimen. Each of these moments was applied to the occiput using a sinusoidal waveform with a peak of  $\pm 1.5$  Nm. Seven cycles were applied per loading condition to achieve requisite preconditioning. Data from the final cycle is reported. Angular velocity of the driveshaft rate was 2.8 degrees/s in order to emulate a quasistatic condition. Starting alignment was obtained by allowing the spines to rest unattached to driveshaft. Due to the expansive axial-rotation neutral zone at the atlanto-axial joint, the spines were manually oriented until the C1 and C2 transverse processes appeared aligned on both the left and right sides, approximating zero initial axial rotation. Upon satisfying this condition, the driveshaft was connected to the occiput mount without disturbing the resting position of the spine.

Force and moment data were recorded at 60 Hz by the 5 kN/110 Nm load-cell. Reflective triads inserted into the vertebral bodies allowed absolute rotation of each vertebra to be measured by a 3-camera, near-infrared motion analysis system at 60 frames/s (model: Eagle 4, Motion Analysis, Santa Rosa, CA). Rotational data were tabulated at -1.5, -0.6, -0.30, -0.15, 0, 0.15, 0.30, 0.6, and 1.5 Nm loads. All data were taken from the "loading" portion of the moment/rotation curve, the portion where moment magnitude was increasing. Despite preconditioning, a neutral zone still manifested at 0 Nm (Figure 25). The average of the two rotation measurements at 0 Nm was taken and added to the rotations measured at the aforementioned moments. This ensured that each moment/rotation plot passed through 0 degrees of rotation at 0 Nm. This methodology was necessary to account for minor variance in initial reference position between tests. This technique also reduced the viscoelastic effects of the tissues, as the spines would drift to a slightly altered reference position during preconditioning.

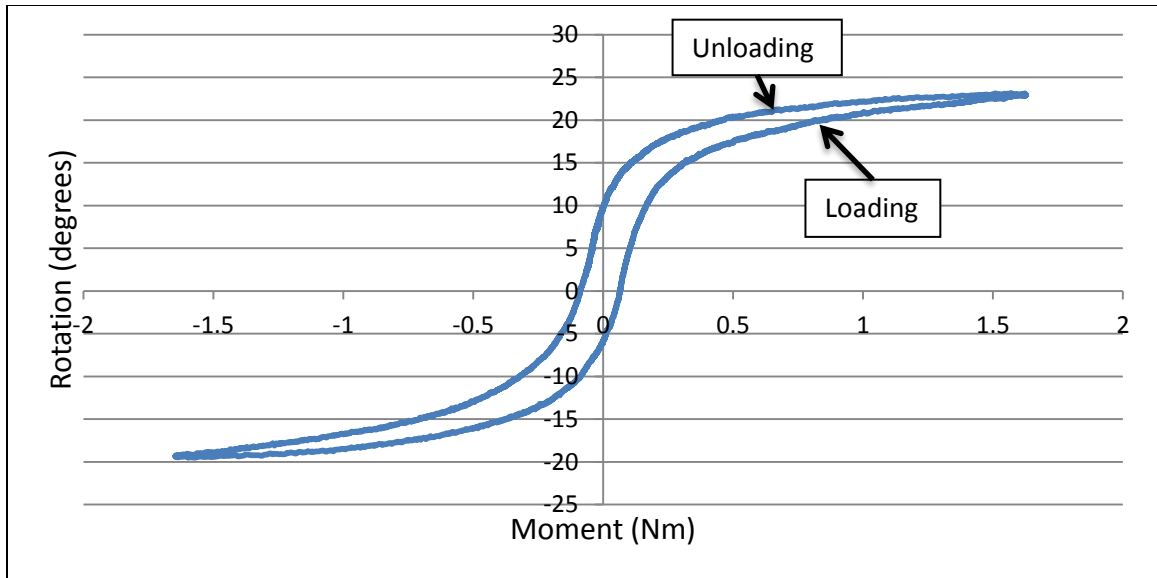


Figure 25: A typical moment/rotation plot for a functional spinal unit. Hysteresis is evident between the loading and unloading curves.

A 0/45/90 degree strain gauge rosette mounted on the anterior face of the atlas allowed cortical strains to be measured at 60 Hz (model: C2A-06-062WW-350, Vishay Micro Measurement, Malvern, PA). The cortical strains measured by the strain gauges were transformed to calculate principal strains ( $E_1, E_2$ ) from the individual gauge strains ( $e_1, e_2, e_3$ , Equation 3: Calculation of strain gauge principal strains from the strain of the individual gauge components):

$$E_1, E_2 = \frac{e_1 + e_2}{2} \pm \frac{1}{\sqrt{2}} * \sqrt{(e_1 - e_2)^2 + (e_2 - e_3)^2}$$

Labview (Labview V8.0.1, National Instruments, Austin, TX) was used to monitor the strain gauge and load-cell data. Both of these measures were zeroed immediately prior to load application for each test.

Immediately after testing the intact case, the facet capsule ligaments at the C1-C2 level were sectioned with a scalpel. This allowed the insertion of a 121-point distributed-pressure

sensor into the facet joints (model: 6900: 10000 psi, Tekscan, South Boston, MA). The previous testing regimen was then performed with C1-C2 facet contact pressure data recorded at 60 Hz. These pressure data were integrated over the contact area to calculate total facet contact force with a custom-developed Matlab code [9]. Calibration of the pressure sensor was accomplished *post-hoc* by compressing the sensor between two pieces of high-density felt in a loadframe.

### **3.1.5 Intact Cervical Spine Finite Element Model Analytic and Experimental Validation Results**

#### **3.1.5.1 Base Resolution Models**

Experimental ROM values generally fell within the bounds of previous studies (Figures 26-28). The lower cervical (C3-C7) response was measured using the existing lower cervical model, and also shows reasonable agreement with the current experimental data [124]. Direct inter-study comparison is difficult, as loading techniques are not uniform in the literature. This is further aggravated by the scarcity of full-cervical (C0-C7) spine experimentation. However, the reported studies utilized similar loading techniques to the current experiments.

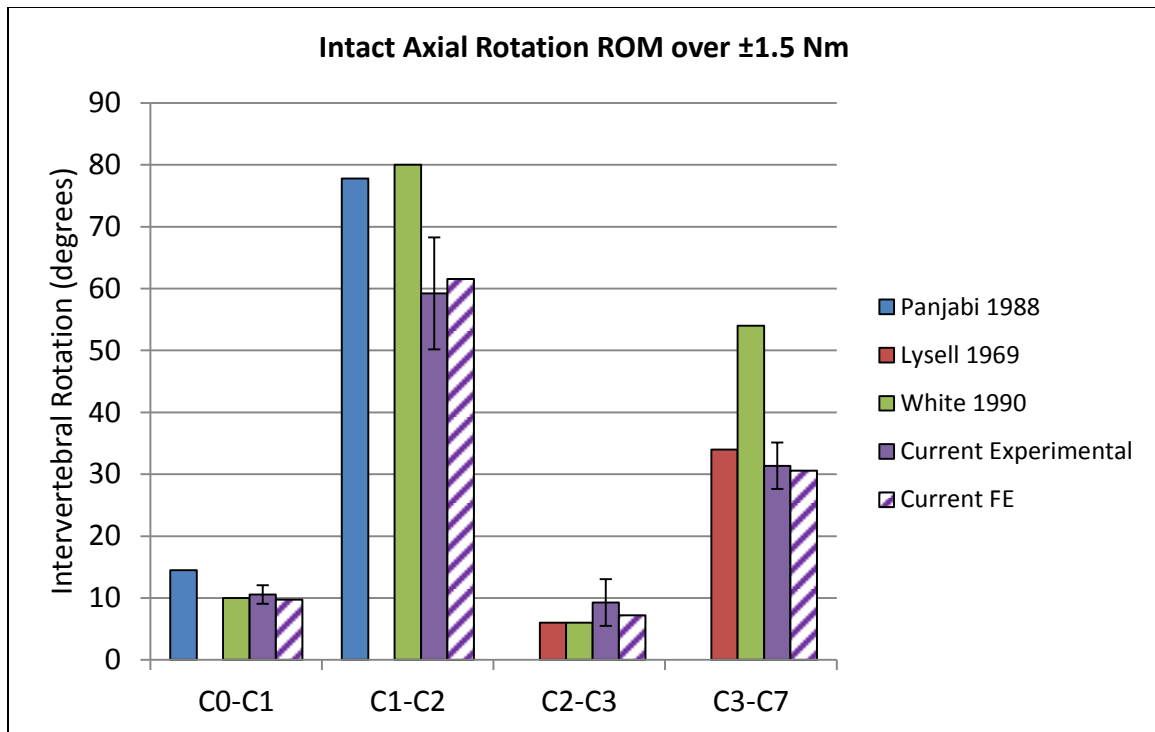


Figure 26: Summed intervertebral biaxial rotation comparison between current and previous studies for intact cervical spines at 1.5 Nm loading [61, 80, 122]. Standard deviation bars are shown for current experiments.

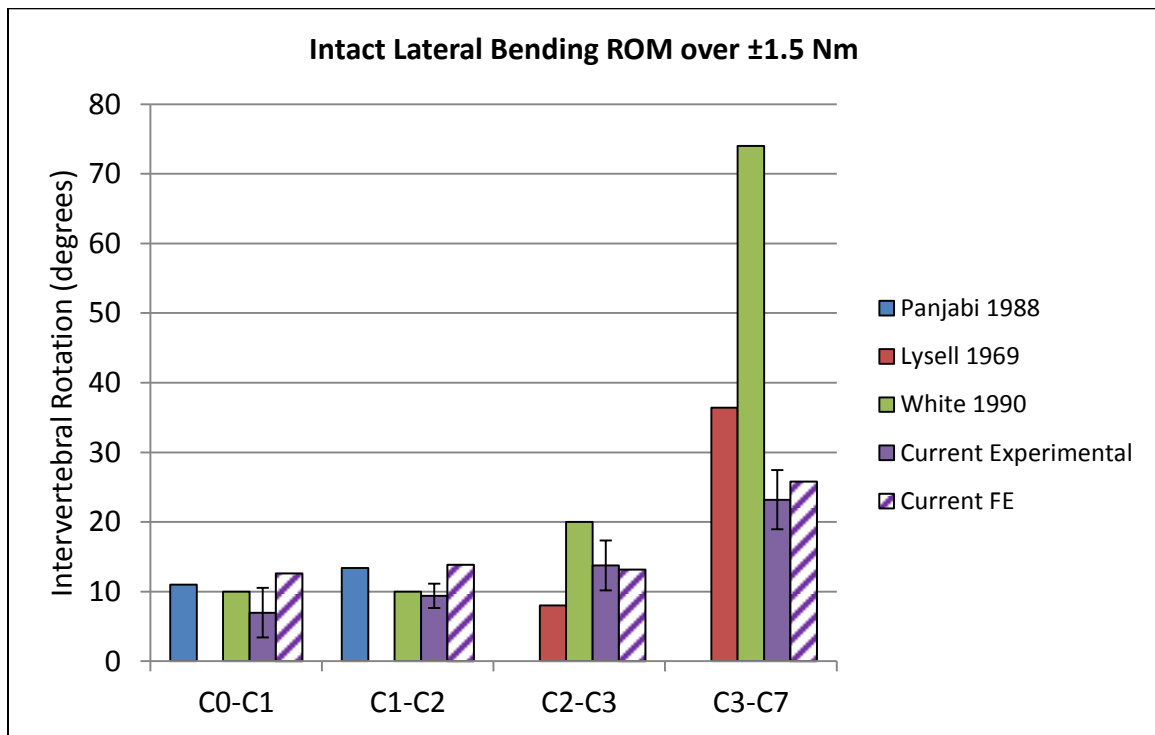


Figure 27: Summed intervertebral bilateral bending comparison between current and previous studies for intact cervical spines at 1.5 Nm loading [44, 62, 96]. Standard deviation bars are shown for current experiments.

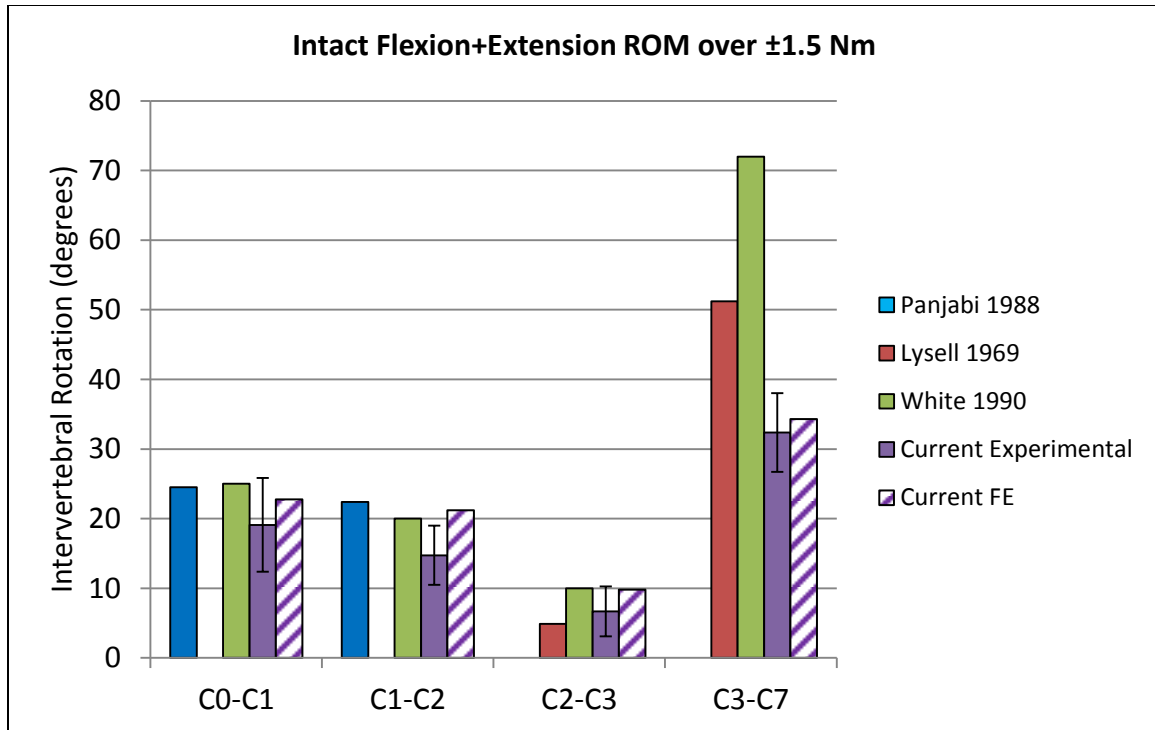


Figure 28: Summed intervertebral flexion+extension rotation comparison between current and previous studies for intact cervical spines at 1.5 Nm loading [44, 62, 96]. Standard deviation bars are shown for current experiments.

In general, the accuracy of the FE model predictions increased as the loading magnitudes were increased (Figures 29-31). The inaccuracy at very small moments was largely due to the FE solver. Very low (near-zero) stiffnesses, such as those exhibited in the neutral zone, often cause FE models to become computationally unstable [1]. Accordingly, rotational stiffnesses necessitated artificial bolstering within the neutral zone. The low stiffness issues in this region were further exacerbated by the low-moment behavior of the intervertebral disc. This effect is illustrated by the relatively flat C2-C3 kinematic responses upon initial loading.

Additional difficulties were encountered when a single ligament provided the predominant stiffening in multiple bending directions. The facet capsule structures are prime examples of such ligaments. These ligaments greatly influenced both the axial rotation and lateral bending responses. Thus, it was very difficult to exactly match the experimental average for both directions with a single ligament property. This may be alleviated in the future by

specifying the ligaments with membranous or shell elements. These element types may be better suited to accurately respond to the shear loading seen in axial rotation.

Noting the relatively low atlanto-axial flexion+extension ROM of the current study compared to previously published research, a concession was made to allow the extension ROM at C1-C2 to exceed the experimentally found values. The current experimental data appear to be overly stiff in extension when compared to previously reported values. This may be a result of an inappropriate reference configuration; the atlanto-axial joints may have been near full extension when the moments were initially applied. Thus, the FE-predicted C1-C2 extension ROM was corrected to match the previously published data.

Delving into the kinematic response at sub-maximal moments, the nonlinear stiffness of the spine is readily apparent. This nonlinearity primarily originates from the shape of the ligamentous force/displacement curve. It became apparent that the ligamentous extensions below 1.5 Nm were largely contained within the toe regions of the ligaments. Therefore, the commonly-published peak ligamentous stiffness values have little applicability within the domain of physiologic spinal motion. Those peak stiffnesses are more applicable for larger loads, where the moment/rotation figures show a greater spinal stiffness and correspondent flattening of the plotted curves.

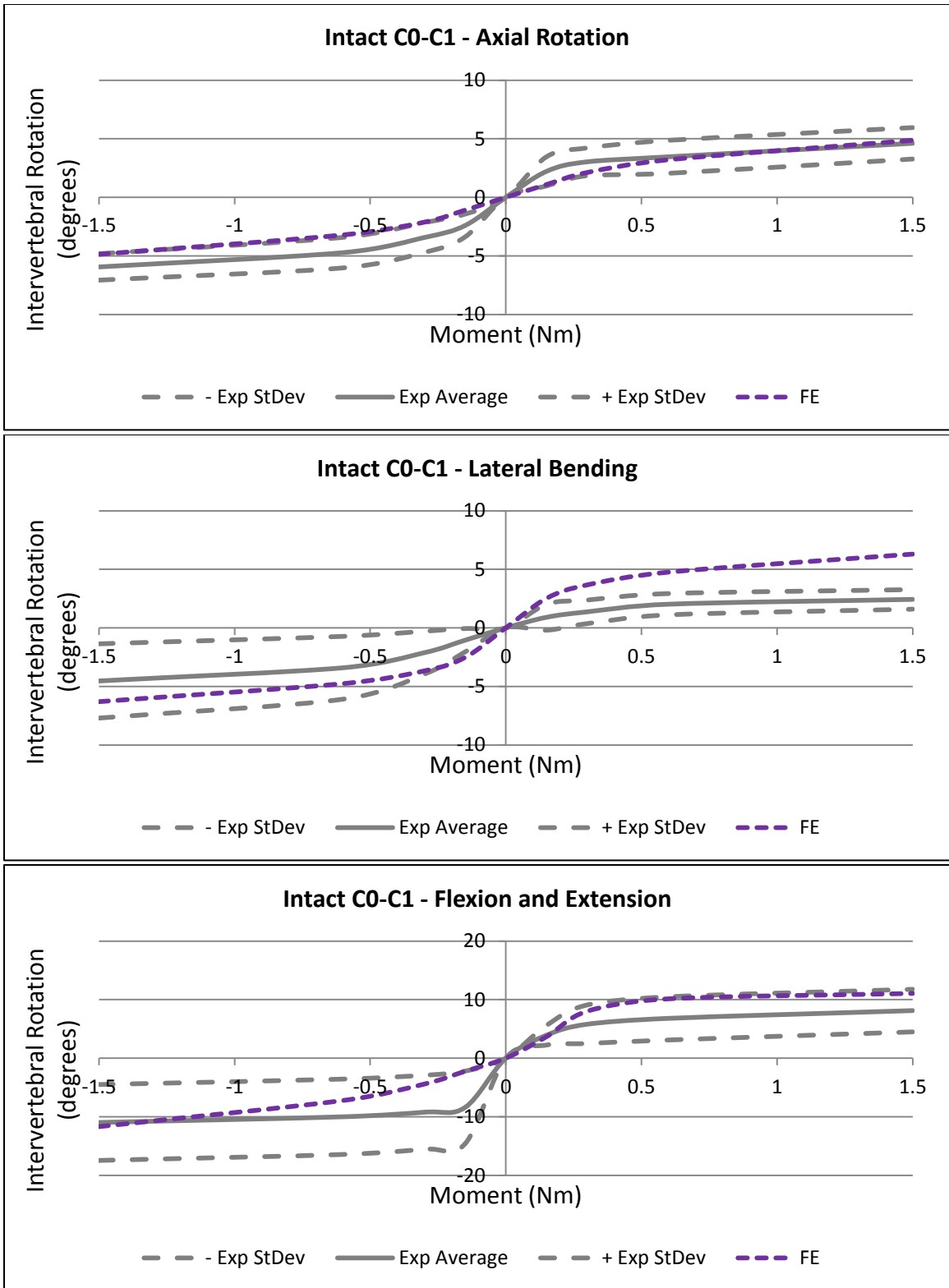


Figure 29: The nonlinear experimental (Exp) and FE-predicted C0-C1 intervertebral rotations due to the application of moments about the three primary bending axes. The experimental averages are plotted within corridors formed by +/- one standard deviation. The negative moment denotes flexion in the flexion and extension plot.

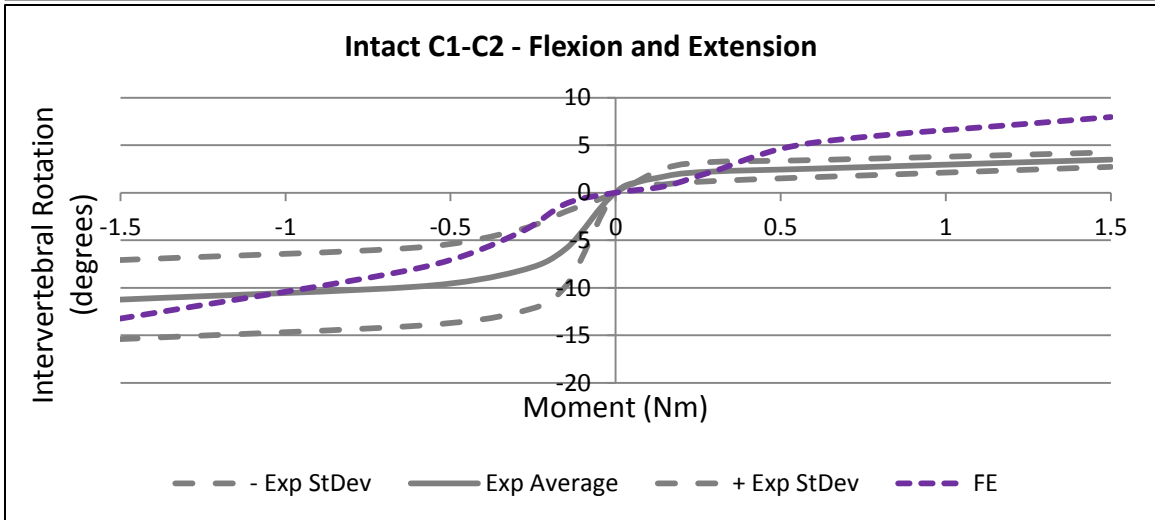
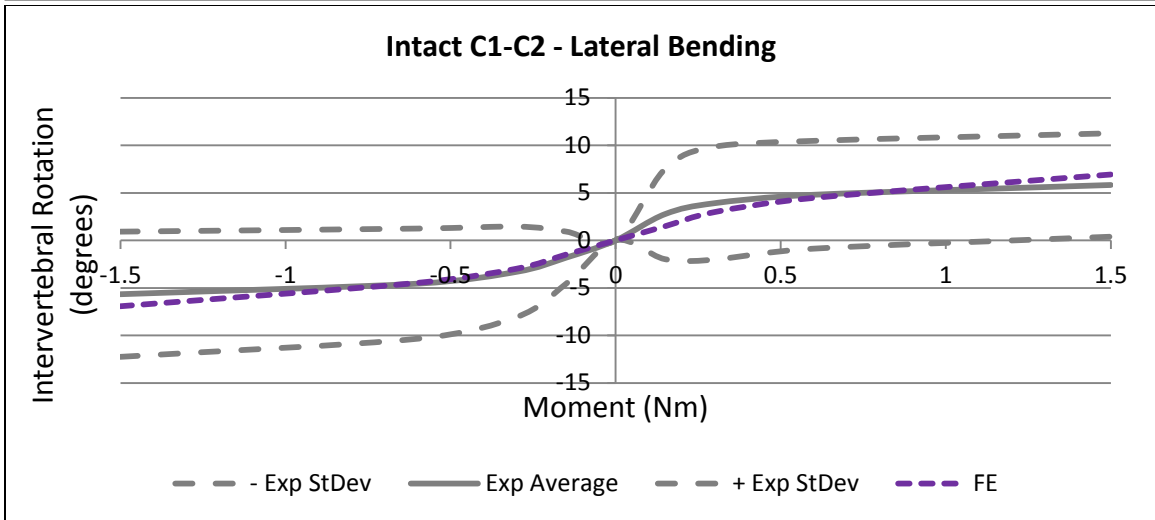
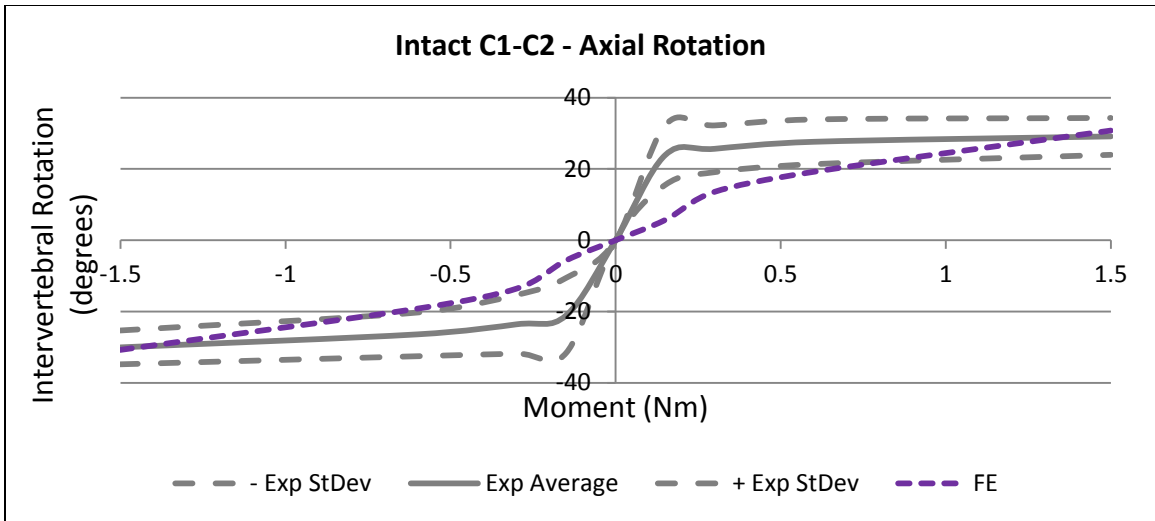


Figure 30: The nonlinear experimental (Exp) and FE-predicted C1-C2 intervertebral rotations due to the application of moments about the three primary bending axes. The experimental averages are plotted within corridors formed by +/- one standard deviation. The negative moment denotes flexion in the flexion and extension plot.

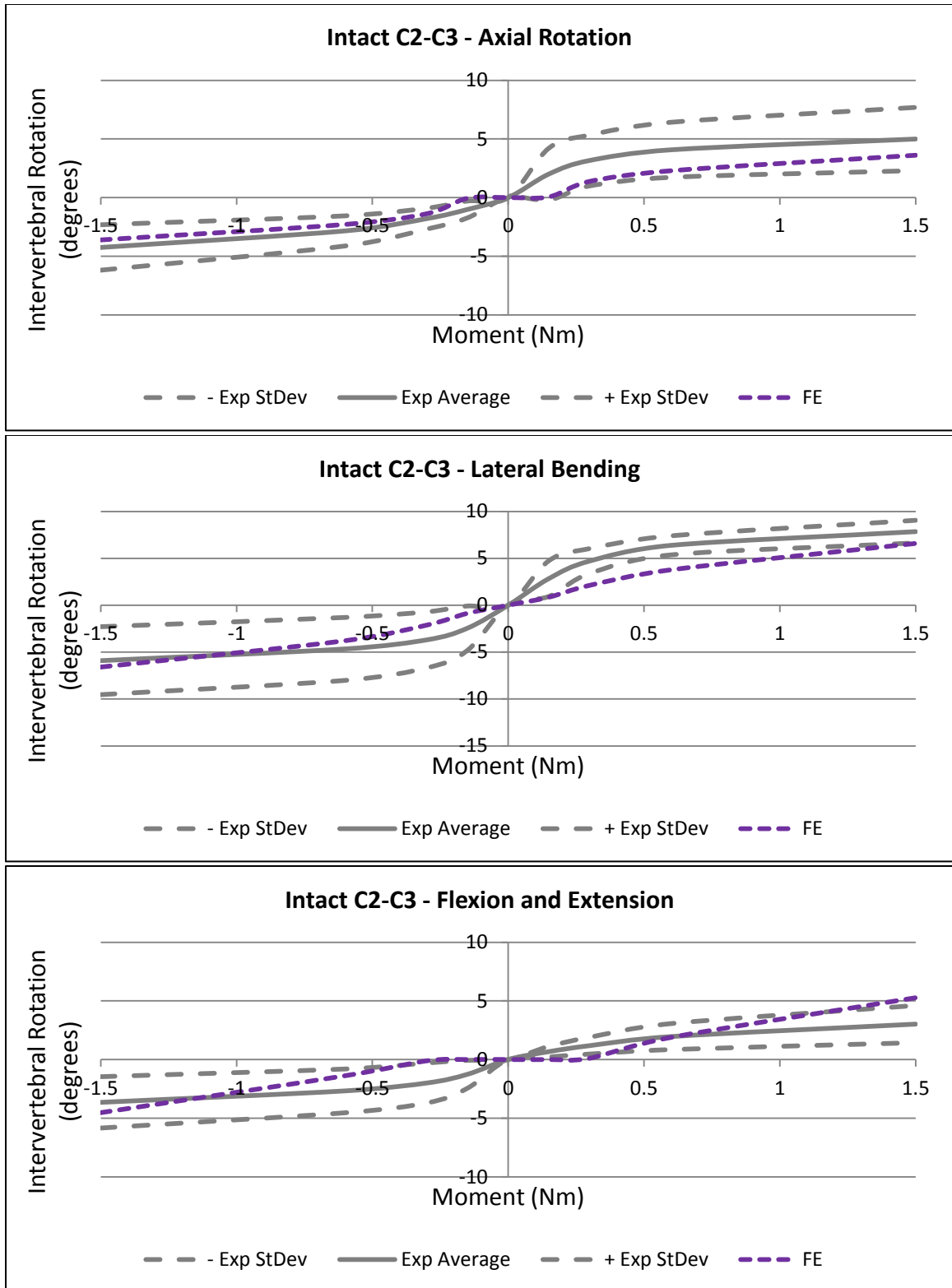


Figure 31: The nonlinear experimental (Exp) and FE-predicted C2-C3 intervertebral rotations due to the application of moments about the three primary bending axes. The experimental averages are plotted within corridors formed by +/- one standard deviation. The negative moment denotes flexion in the flexion and extension plot.

Experimentally-measured facet contact forces at C1-C2 showed a remarkable degree of symmetry during flexion and extension loading. Examining the Tekscan pressure distribution, it is evident that the center of pressure moved in the anterior-posterior direction throughout flexion and extension, but total force magnitude did not change appreciably (Figures 32 and 33). This reveals the critical role of the C1-C2 facets in supporting loads; the facets are constantly resisting forces when loaded in flexion and extension. This is in stark contrast to the facets in the lower cervical spine, which are often completely unloaded in flexion [16, 125]. Lateral bending demonstrated expected behavior, where lateral bending increased load on the ipsilateral facet, while reducing pressure on the contralateral joint. Due to the relative perpendicularity of the facets to the rotational axis of the dens, very little alteration in facet contact force was observed in axial rotation. In contrast to the FE-predicted data, the experimental measurements showed a non-zero force even in the absence of an applied moment. This can be explained by the finite thickness of the Tekscan measurement film, which induced a preload force between the facet surfaces upon insertion.

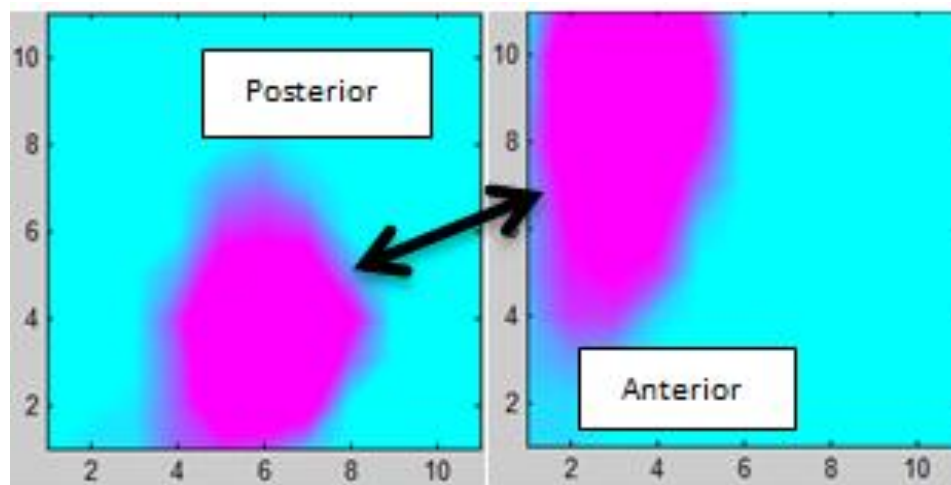


Figure 32: Experimentally-measured movement of the center of C1-C2 facet contact pressure from flexion (left) to extension (right). Axes labels correspond to discrete pressure measurement regions on the Tekscan film (each region measures 1.27 mm by 1.27 mm).

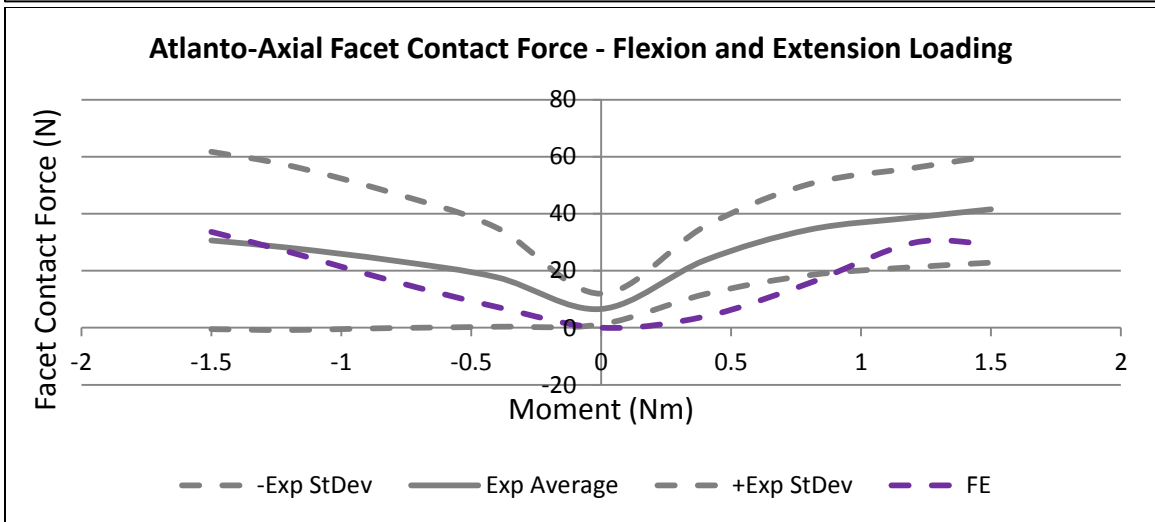
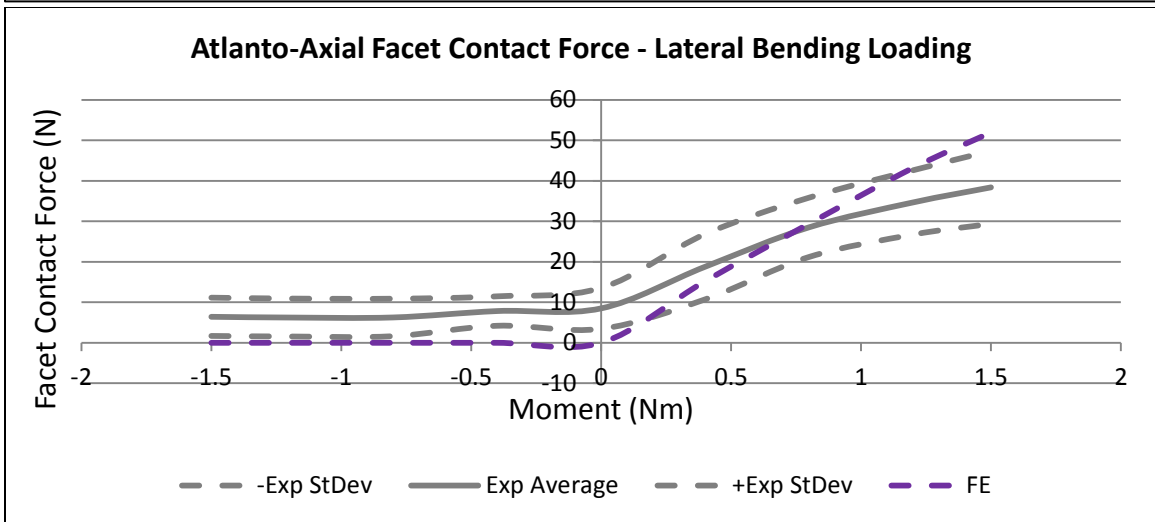
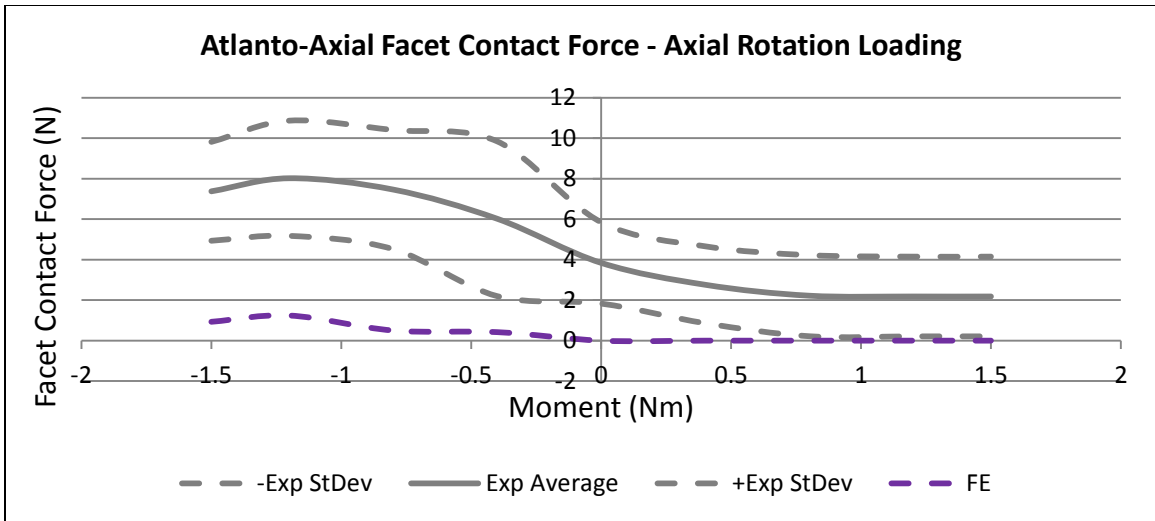


Figure 33: The experimentally-measured (Exp) and FE-predicted unilateral contact forces at the C1-C2 facets throughout moment loading. The experimental averages are plotted within corridors formed by +/- one standard deviation. The negative moment denotes flexion in the flexion and extension plot.

Cortical strains at C1 generally decreased following sectioning of the C1-C2 facet capsule ligaments (Figure 34). This is anticipated, as these ligaments are tensioned at the extrema of intervertebral rotation. Due to the attachment of the ligaments to the cortical tissue, it is expected that the bones are further stressed by the tensile forces present in these ligaments. For similar reasons, the FE-predicted cortical strains are very miniscule in relation to the experimental measures. The stresses at the site are also very low as predicted by the FE model. This may be explained by the physiological attachments of the soft tissues to cortical bone. There is a great deal of soft tissue adherent to the atlas near the strain measurement site in the experimental case. The complexity of this tissue made its modeling unfeasible in the FE case. It appears that the tissue is responsible for applying stresses to the cortical bone in the strain-measured area. In comparison, the FE model predicted much greater strains and stresses at the base of the dens, where the bony structure is loaded via surface-to-surface contact stresses. Von Mises stresses on the order of 40 MPa and deformations of 300 microstrain were found in this location, which shows agreement with previous studies [122]. Furthermore, substantial strains (approximately 200 microstrain) were found in the subchondral bone under the loaded facets. Thus, it appears that the strain under-prediction at the atlas is largely due to the unmodeled soft tissues.

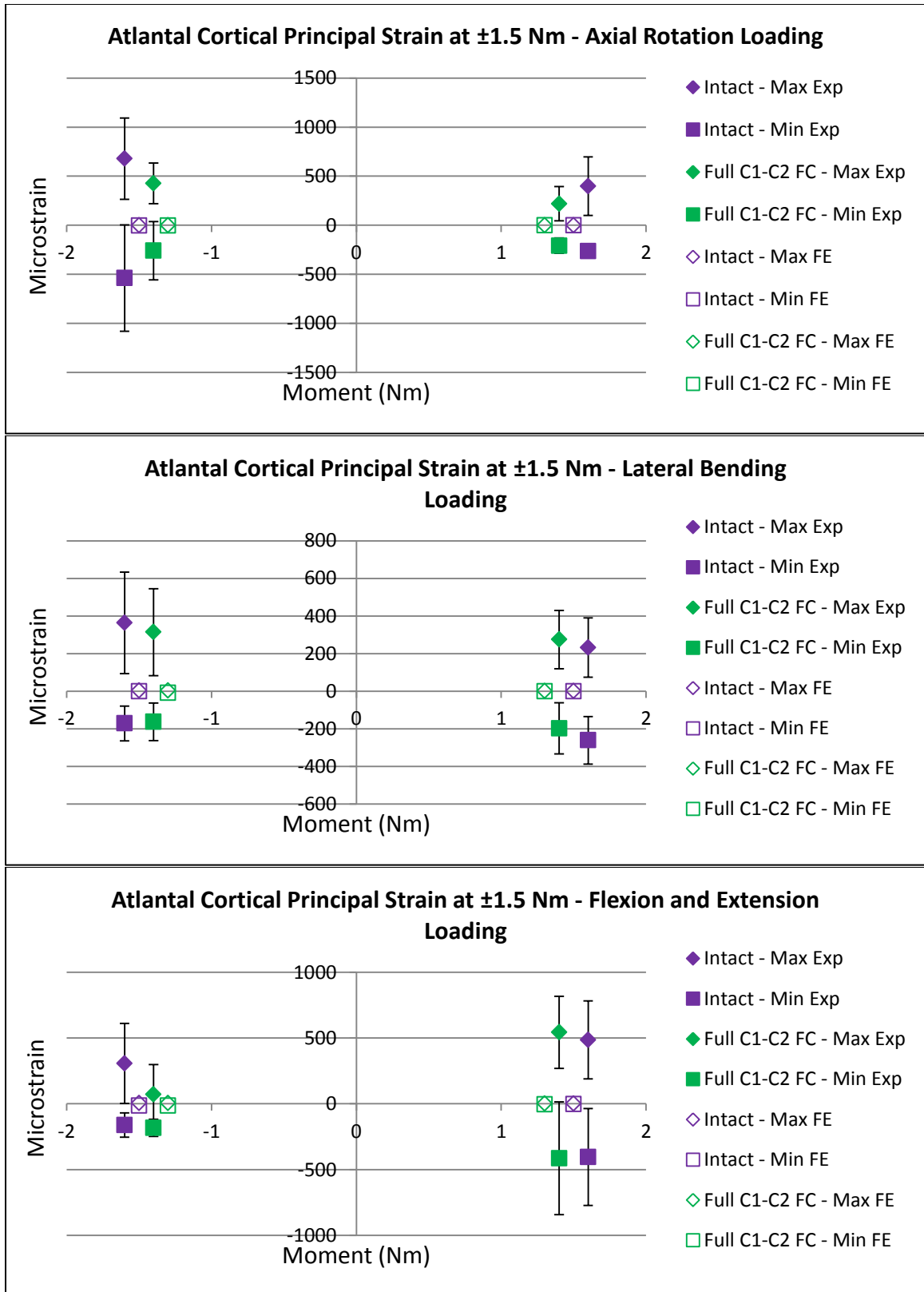


Figure 34: The experimentally-measured (Exp) and FE-predicted cortical strains at the atlas at peak moments. Average strains were generally reduced when the facet capsule ligaments were sectioned at the atlanto-axial joint.

Intervertebral foramen measurements showed dynamic reductions due to the application of moments in the axial rotation, lateral bending, and extension directions (Figure 35). Flexion loadings increased the foraminal width and height, therefore this data is not reported. This same finding applied to the contralateral foramen dimensions due to moments applied in the axial rotation and lateral bending directions.

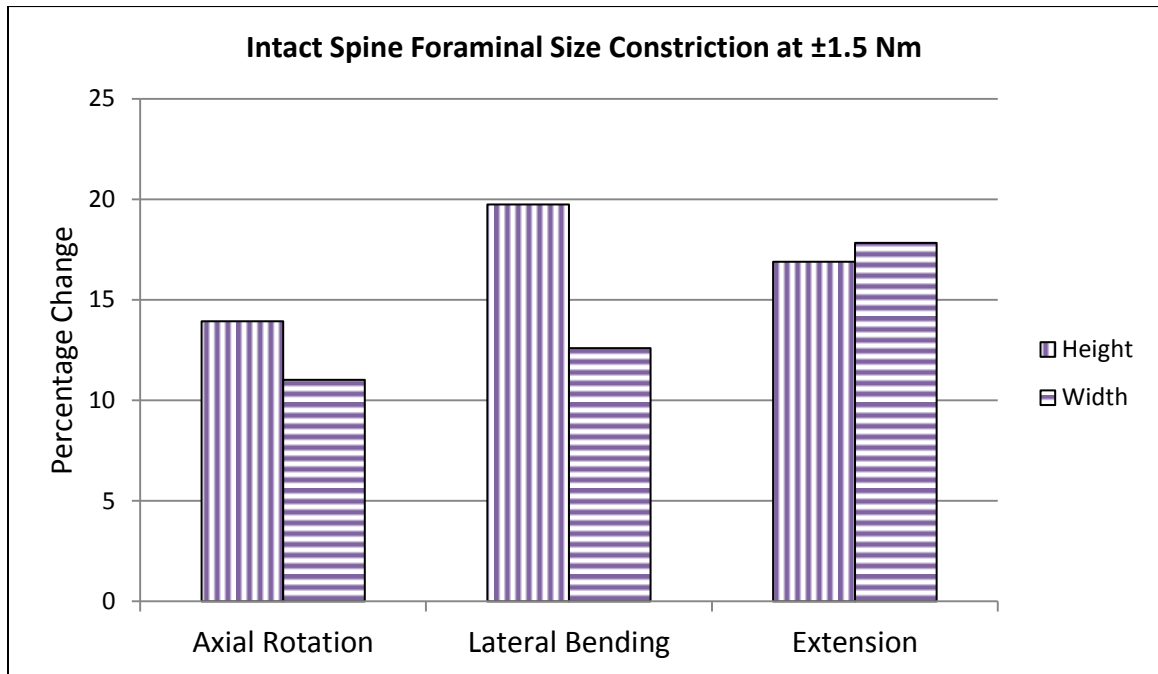


Figure 35: The FE-predicted change in left C5-C6 intervertebral foramen height and width for the intact cervical spine due to the application of a 1.5 Nm moment.

Initial height and width of the left C5-C6 foramen measured 9.001 mm and 8.373 mm, respectively. These measurements fall within the range of previously reported values [83]. Neither height nor width change of the foramen were likely to incite radiculopathy, using guidelines reported by Panjabi *et al* (see section 1.2.1.2 Neural Tissue) [83]. This finding is expected, as radiculopathy is unanticipated in the intact spine throughout normal, physiologic motion.

### 3.1.5.2 Convergence Models

The vast majority of convergence parameters were only slightly affected by mesh resolution variance. ROM was affected the least, with an average difference of 0.36% between the Low and Medium Resolution models, and 0.56% between the Medium and High Resolution variants. Performing this same calculation for strain energy showed a difference of 0.83% and 1.07% for the respective groups, well within the 10% convergence criteria. The greatest variance was seen in the C1-C2 facet contact forces. Although most facet contact forces featured very minor alterations between the models, the axial rotation direction demonstrated a large, 58% discrepancy between the Medium and High Resolution models. However, force magnitude only varied by 0.69 N despite the large percentage difference. The other rotational directions featured contact forces varying from 30 to over 50 N, where a 0.69 N difference was more negligible. Interestingly, the contact pressure between the Medium and High Resolution axial rotation cases did not vary nearly as much as the 58% percent force difference would suggest. The contact area was larger, dispersing the force to show only a 4.3% difference in pressure. Closer inspection revealed that the greater conformability of the second-order elements allowed more surface area to come into contact. The High Resolution lateral bending model was unable to proceed past 59% (0.89 Nm) due to distortion of the second-order elements. Accordingly, the comparison between the High and Medium Resolution lateral bending models were made at this loading magnitude. Concerns about interpolating were mitigated since the kinematic and facet contact force responses were largely linear at that moment magnitude (see Figures 29-31, 33).

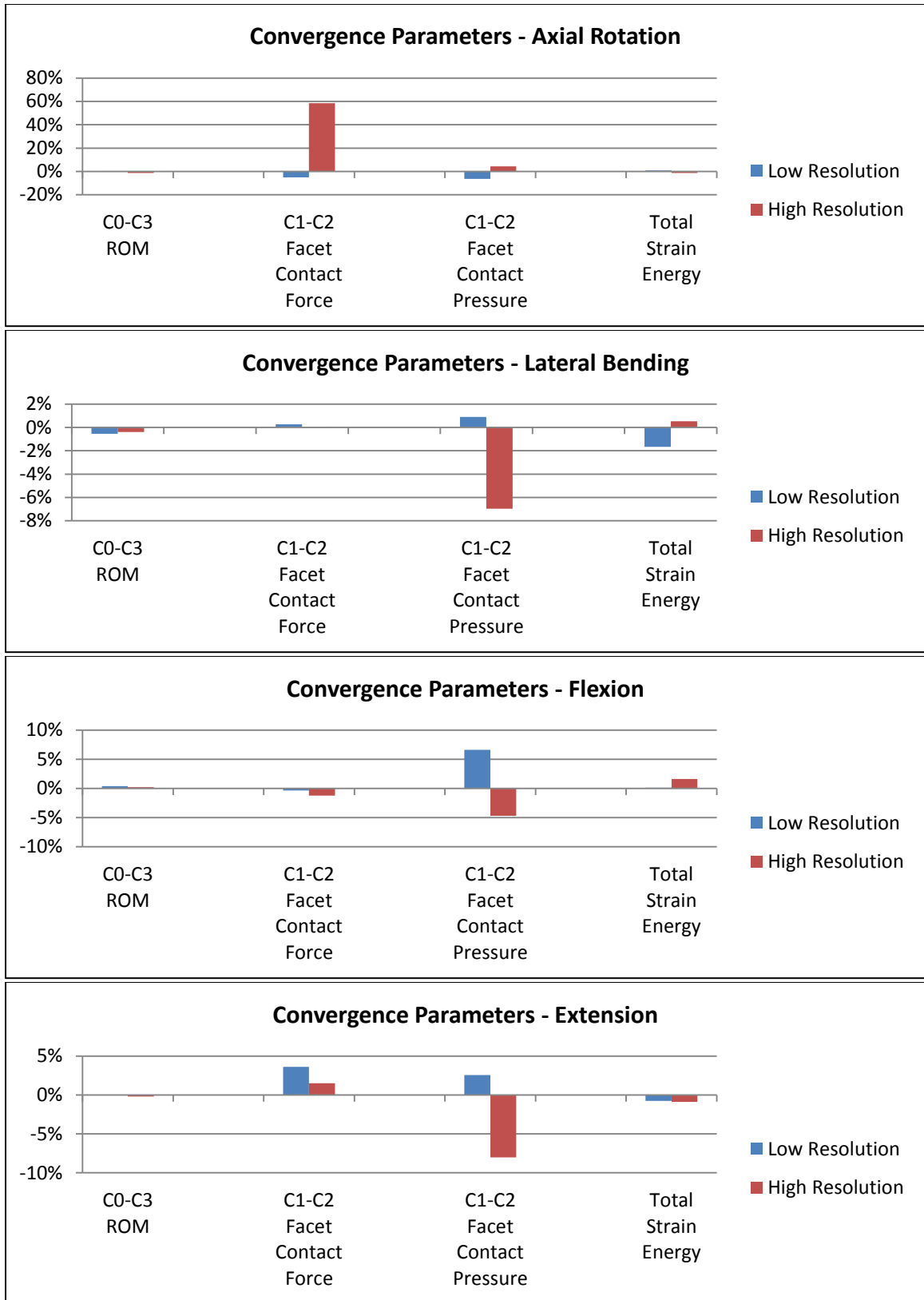


Figure 36: The variance in convergence parameters relative to the base (Medium Resolution) model.

## **3.2 Experimental Measurement of Injured Ligament Mechanical Properties (Specific Aim 2)**

Testing of ligamentous damage focused on the alar, anterior longitudinal, and flaval ligaments. The ALL and LF ligaments were chosen as they have been found: 1) to greatly influence spinal mechanics, 2) have vastly different ratios of collagen to elastin content, and 3) are commonly injured from excessive strains experienced during whiplash-type trauma in the lower cervical spine [46, 70, 86]. The alar ligaments were examined since they provide the primary constraint to hyper-rotation in the upper cervical spine, and can be injured in head-turned impacts [78, 79].

### **3.2.1 Injured Ligament Properties Experimental Method**

Following full-cervical, pure-moment testing (see section 3.1.4 Intact Cervical Spine Finite Element Model Experimental Validation and 3.3.3 Ligamentous Injury Cervical Spine Finite Element Model Experimental Validation Method), bone-ligament-bone specimens (Figure 37) were extracted from the spines with a diamond-bladed bandsaw (Exakt model 30/736, Exakt Apparetebau GmbH & Co., Norderstedt, Germany). Total yield of these six spines and one additional spine that did not undergo pure-moment testing included 7 left alar, 14 ALL (C2-C3: n = 6, C4-C5: n = 6, C5-C6: n = 1, C6-C7: n = 1) and 12 LF (C2-C3: n = 7, C4-C5: n = 4, C6-C7: n = 1) specimens. The bony portions of the specimens were potted into PMMA. Self-tapping screws were inserted into these bony tissues to increase purchase and reduce the possibility of slippage within the PMMA. Since the alar ligaments are composed of both an occipital (C0-C2) and atlantal (C1-C2) portion, the occipital and atlantal bony portions were potted together so the ligament could be tested as a unit. Wires were used to hold the occipital and atlantal bone

segments together in a physiologic configuration, as well as provide more purchase for the dens (C2) bone within the PMMA (Figure 38).

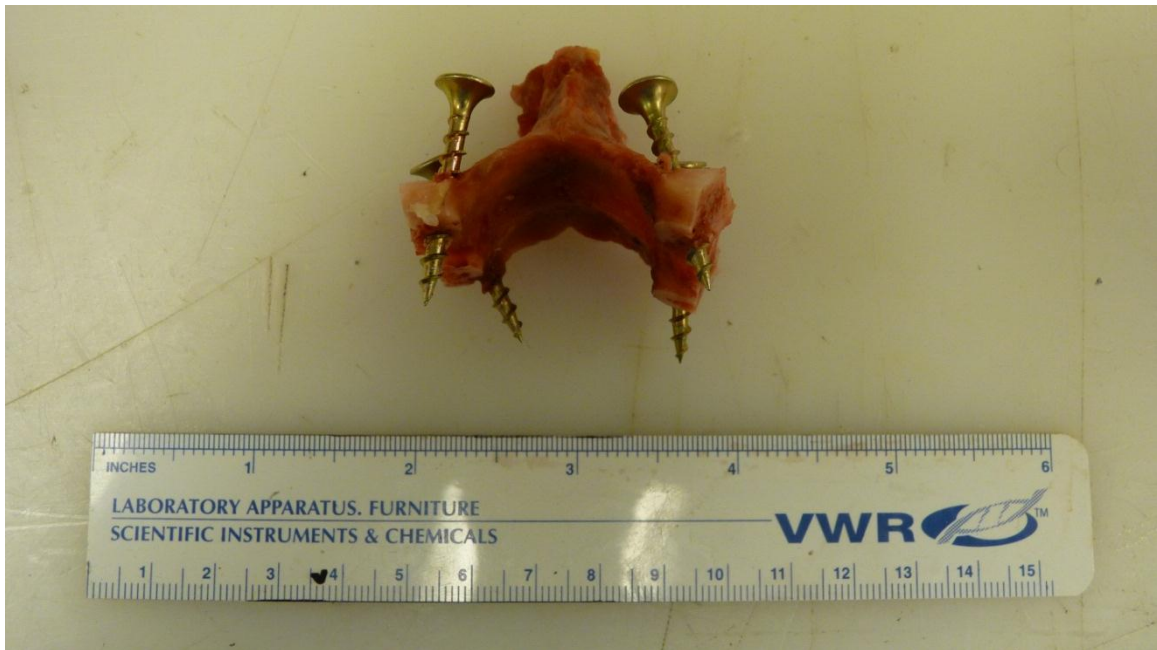


Figure 37: A typical bone-ligament-bone preparation, prior to potting in PMMA (LF shown).

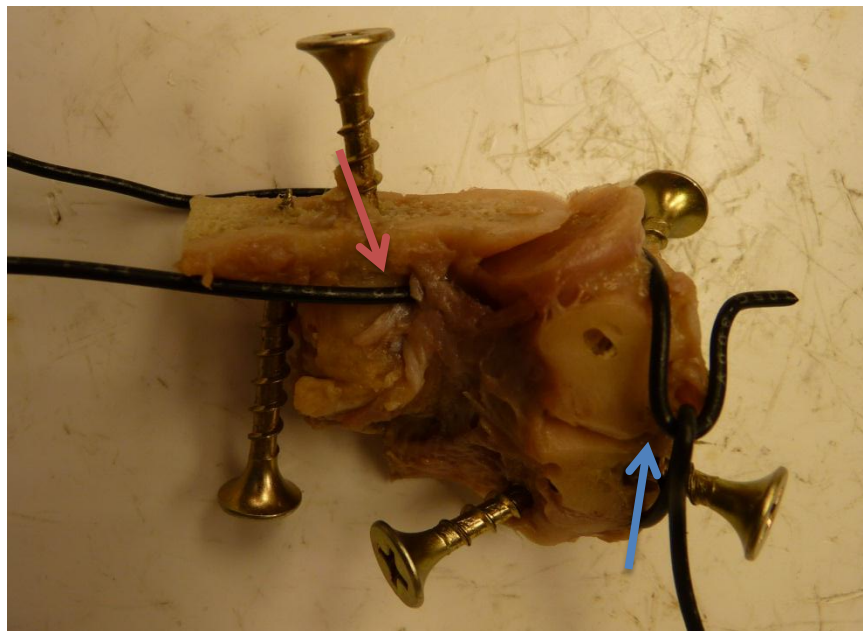


Figure 38: Wires were used to prevent slippage of the dens within the PMMA (red arrow). Wires were also employed to hold the occipital and atlantal bones together in a physiologic configuration (the atlanto-occipital junction is denoted with the blue arrow).

Tensile stiffness testing was accomplished with a servo-hydraulic loadframe (Mini Bionix II, model 858, MTS, Eden Prairie, MN). Displacement was measured via a crosshead-mounted

linear variable differential transformer (LVDT). Force was measured by an inline-mounted 5 kN load-cell (Model 661.19-01, MTS, Eden Prairie, MN). Specimens were housed within a heated, saline-filled tank, which replicated physiologic temperature (37<sup>0</sup>C) and hydration (Figure 39). Reference position (displacement = 0 mm) was determined by the position of the resting ligament weighted by the upper potting box (300 g) while submerged in saline. The MTS actuator was lowered until a hole in the actuator aligned with a hole in the upper potting box (Figure 40). A close-tolerance shear pin could only be inserted at perfect vertical alignment, ensuring an equal starting force for all ligaments. The specimen was mounted on a custom-made, biaxially-sliding table to allow adjustment of horizontal alignment. An automated testing sequence was developed, requiring no user intervention beyond zeroing the LVDT and load-cell at the beginning of the test. The testing sequence was accomplished using the following protocol: 1) increase displacement to induce 5 N tensile load; hold displacement at this level for 10 minutes, 2) apply 120 cycles of sinusoidal displacement (0.0 to 0.4 mm relative to the displacement at 4 N of tension) for preconditioning and quasistatically (0.2 mm/s) ramp from zero displacement to 40 N to determine initial stiffness, 3) dwell 10 minutes, 4) repeat Step 2, 5) induce partial ligament damage, 6) repeat Step 2 at 10, 30, and 90 minutes after the damage step to measure final stiffness. A pilot study (n = 14) indicated that the majority of ligaments could withstand 40 N without suffering damage, while undergoing comparable displacement to that experienced in normal physiologic cervical motion. The pilot study also found that the ligaments did not significantly alter in any mechanical properties between 90 minutes, 270 minutes, and 16 hours post-damage, so the final stiffness readings were taken at 90 minutes post-damage for the current experiments.

Partial ligament damage (Step 5) was executed by preloading the ligaments to 10 N, rapidly tensioning at 50 mm/s, and immediately reversing the actuator at 35 mm/s when the

load-cell detected a specified drop in force that indicated partial damage of the ligaments. Approximately 0.05 s were required to accelerate the actuator to 50 mm/s from the 0.2 mm/s rate immediately preceding damage. The force drop values were set to 1% for the alar and ALL specimens, and 3% for LF specimens, which were determined from pilot experiments to consistently induce damage without completely compromising the ligaments. The loading rate was modeled after a strain rate of 10/s, which has been reported to exist in impact trauma [60]. Force and displacement data were recorded at 204.80 Hz for quasistatic loading and 1024.0 Hz for high-rate loading.

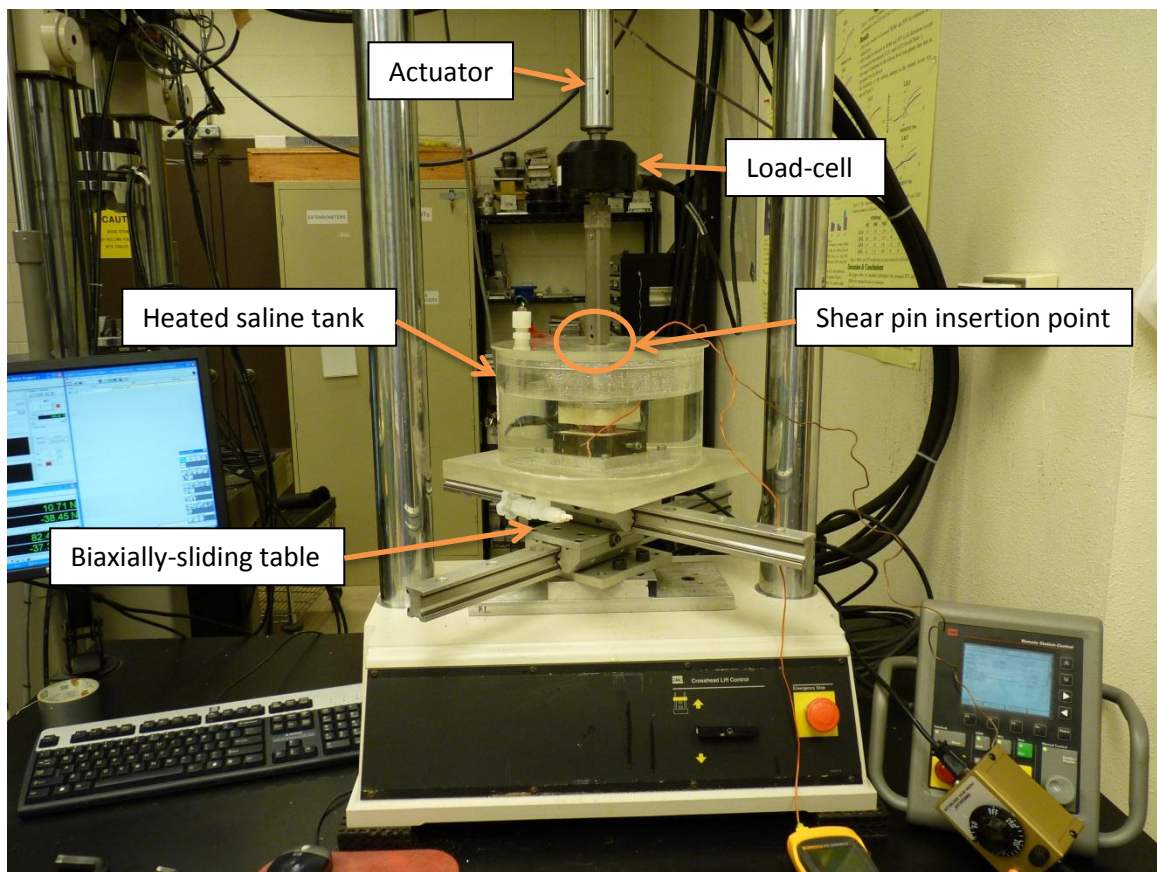


Figure 39: The ligament tensile-testing apparatus.

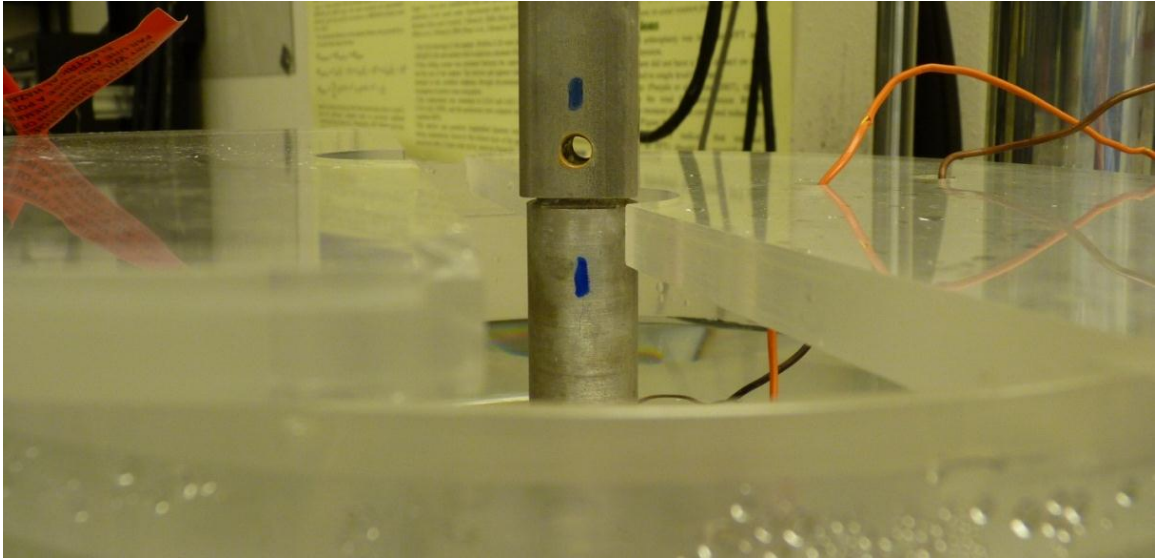


Figure 40: Alignment of the holes in the sliding, actuator-mounted square tube and potting box-mounted rod prior to shear-pin insertion ensured no initial force was applied by the actuator to the ligament.

### 3.2.2 Injured Ligament Properties Experimental Data Analysis

Stiffness values were calculated at discrete force intervals: between 10-20 N, 20-30 N, and 30-40 N. Force/displacement data for each segment were fitted using a linear regression tool in Excel (Office 2010, Microsoft, Redmond, WA). The slope of this line defined the stiffness for the segment. Squared standard Pearson's correlation coefficients ( $R^2$ ) averaged 0.993 (standard deviation: 0.014) for all segments. The calculation of stiffness at discrete force intervals accounted for the permanent yield experienced by the specimen as well as the nonlinear mechanical behavior seen in ligaments. The reporting of stiffness in force/length units also avoided the potentially erroneous method of measuring cross-sectional area and gauge length of the specimens. Displacement at the 10 N and 40 N force levels were also compared before and after injury to quantify the amount of permanent deformation. Percentage change values were calculated relative to the undamaged state.

Statistical analyses were performed to determine significant differences between the measurement timepoints for both stiffness and toe region length (displacement at 10 N). Each

ligament type (alar, ALL, and LF) was analyzed separately. A square root transformation was used to normalize the residuals and make them independent of the means (SAS V9.2, Cary, NC). Analysis was conducted with a randomized block design, blocking on specimen and time as a fixed effect. Significance was assigned to datasets showing p-values less than 0.01.

### **3.2.3 Injured Ligament Properties Experimental Results**

The experimental ligament data show a significant increase in toe length after damage for all specimens (increase of 1.985 mm = 218.11% for alar, 1.866 mm = 523.70% for ALL, 2.819 mm = 301.83% for LF, Tables 9, 11, and 13). Similarly, all specimens required greater displacement to reach 40 N of force (increase of 2.036 mm = 127.57% for alar, 2.172 mm = 322.20% for ALL, 2.781 mm = 163.48% for LF, Figure 41). Tensile tests of two ALL and two LF specimens were halted at 30 N due to excessive strain. Stiffness within the 10-40 N range experienced only a minor, insignificant reduction for alar (4.75% drop) and LF (15.30% drop) specimens, but a much larger, significant reduction for ALL specimens (57.59% drop, Tables 8, 10, and 12). The aforementioned pilot study revealed that there is no significant difference in toe region length or stiffness within the two pre-damage readings or the three post-damage readings. However, the data from the second pre-damage tensile test are reported because they demonstrated more linearity (higher  $R^2$  values) than data from the first pre-damage test. The additional linearity may be a result of the extra preconditioning received by the specimens prior to the second tensile test. Post-damage stiffnesses and displacements are reported from the 90 minute timepoint since clinical injury analysis is likely to occur more than 90 minutes post-injury [63].

Table 8: Alar stiffness before and after induced damage. The standard deviations are shown in parentheses. Significant ( $p < 0.01$ ) differences are shown in shaded cells.

Range (N)	Average Pre-Damage Stiffness (STD): N/mm	Average Post-Damage Stiffness (STD): N/mm	Average Stiffness Reduction (STD): N/mm	Average Stiffness Reduction Percentage
10-20	32.427 (7.398)	31.457 (10.191)	0.970 (7.495)	2.62%
20-30	57.286 (11.209)	53.931 (12.455)	3.354 (8.149)	5.79%
30-40	72.320 (14.665)	68.287 (18.308)	4.033 (12.310)	5.83%
10-40	54.011 (20.060)	51.225 (20.683)	2.786 (9.649)	4.75%

Table 9: Alar displacement at reference forces before and after damage. The standard deviations are shown in parentheses. Significant ( $p < 0.01$ ) differences are shown in shaded cells.

Reference Force (N)	Average Pre-Damage Displacement at Reference Force (STD): mm	Average Post-Damage Displacement at Reference Force (STD): mm	Average Increase in Displacement After Damage (STD): mm	Average Percentage Increase in Displacement After Damage
10	1.177 (0.539)	3.162 (0.579)	1.985 (0.274)	218.11%
40	1.825 (0.591)	3.861 (0.680)	2.036 (0.337)	127.57%

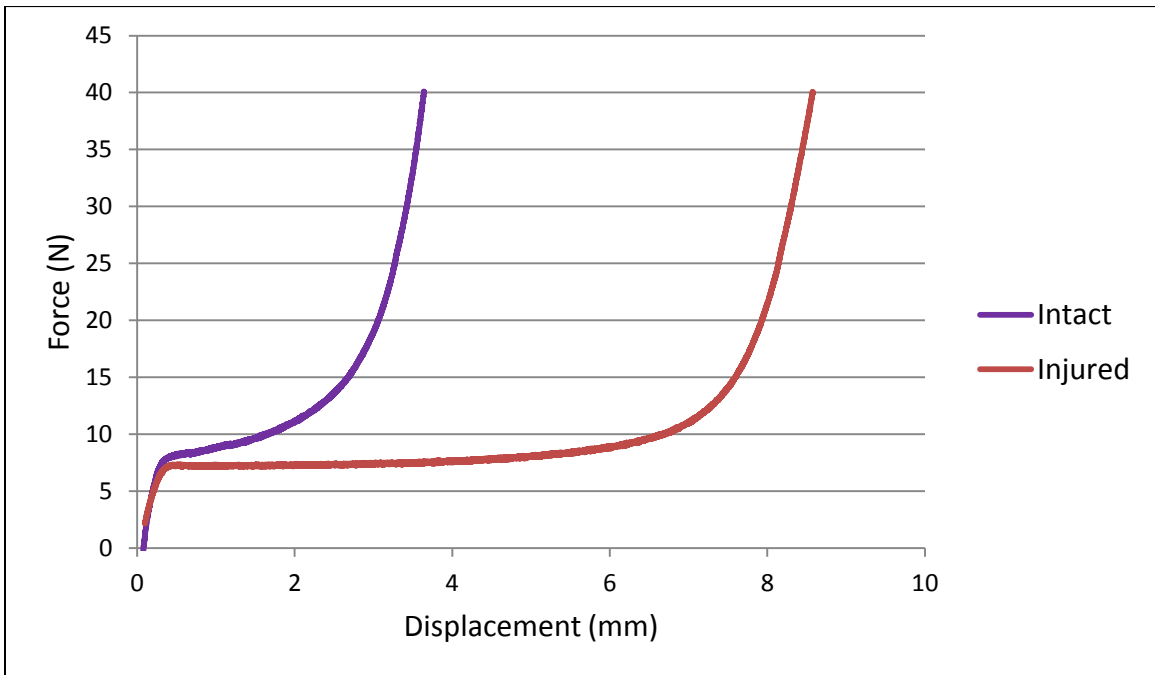


Figure 41: A typical ligament force/displacement plot shows an increase in toe region length (displacement at 10 N) after injury.

Table 10: ALL stiffness before and after induced damage. The standard deviations are shown in parentheses. Significant ( $p < 0.01$ ) differences are shown in shaded cells.

Range (N)	Average Pre-Damage Stiffness (STD): N/mm	Average Post-Damage Stiffness (STD): N/mm	Average Stiffness Reduction (STD): N/mm	Average Stiffness Reduction Percentage
10-20	80.728 (35.555)	29.696 (14.536)	51.032 (34.123)	59.71%
20-30	108.696 (31.753)	43.905 (18.772)	64.791 (32.466)	57.56%
30-40	135.591 (47.590)	60.249 (29.419)	82.427 (46.550)	55.49%
10-40	103.338 (44.879)	43.835 (24.615)	65.266 (39.823)	57.69%

Table 11: ALL displacement at reference forces before and after damage. The standard deviations are shown in parentheses. Significant ( $p < 0.01$ ) differences are shown in shaded cells.

Reference Force (N)	Average Pre-Damage Displacement at Reference Force (STD): mm	Average Post-Damage Displacement at Reference Force (STD): mm	Average Increase in Displacement After Damage (STD): mm	Average Percentage Increase in Displacement After Damage
10	0.513 (0.307)	2.379 (0.927)	1.866 (0.927)	523.70%
40	0.845 (0.379)	3.046 (0.703)	2.172 (0.651)	322.20%

Table 12: LF stiffness before and after induced damage. The standard deviations are shown in parentheses. Negative stiffness reduction indicates stiffness increased after damage. Significant ( $p < 0.01$ ) differences are shown in shaded cells.

Range (N)	Average Pre-Damage Stiffness (STD): N/mm	Average Post-Damage Stiffness (STD): N/mm	Average Stiffness Reduction (STD): N/mm	Average Stiffness Reduction Percentage
10-20	36.513 (18.877)	29.180 (14.481)	7.333 (9.442)	14.45%
20-30	57.304 (20.941)	46.586 (16.386)	10.719 (13.777)	16.17%
30-40	76.854 (24.620)	60.804 (21.086)	14.023 (22.581)	15.26%
10-40	55.716 (26.857)	45.087 (21.648)	10.495 (15.989)	15.30%

Table 13: LF displacement at reference forces before and after damage. The standard deviations are shown in parentheses. Significant ( $p < 0.01$ ) differences are shown in shaded cells.

Reference Force (N)	Average Pre-Damage Displacement at Reference Force (STD): mm	Average Post-Damage Displacement at Reference Force (STD): mm	Average Increase in Displacement After Damage (STD): mm	Average Percentage Increase in Displacement After Damage
10	1.398 (1.069)	4.217 (1.574)	2.819 (0.886)	301.83%
40	2.275 (1.407)	5.159 (2.016)	2.781 (0.879)	163.48%

Average peak force for alar specimens during the damage step was 381.35 N (standard deviation: 250.18 N) at 4.502 mm (standard deviation: 1.318 mm). ALL specimens averaged 589.95 N (standard deviation: 242.84 N) at 3.567 mm (standard deviation: 0.768 mm) displacement. The LF specimens attained 353.30 N (standard deviation: 148.80 N) at 4.986 mm (standard deviation: 1.649 mm). These displacements are in agreement with those reported during 8g whiplash-type impacts (ALL: 3.4 mm, LF: 4.6 mm) [46, 85]. A typical force/displacement curve for a damage event is shown in Figure 42.

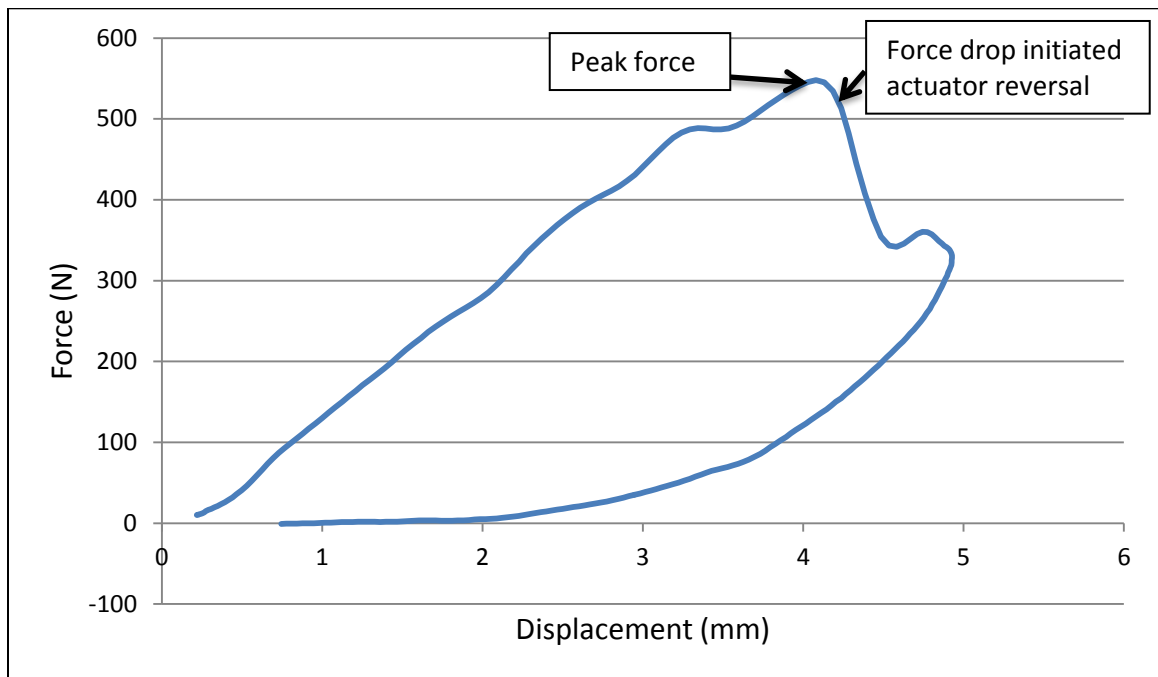


Figure 42: A typical damage step force/displacement curve. The displacement continued to increase after the force drop, indicating system lag.

### **3.3 Ligamentous Injury Cervical Spine Finite Element Model (Specific Aim 3)**

#### **3.3.1 Ligamentous Injury Cervical Spine Finite Element Model Generation**

The intact FE model (see section 3.1 Intact Cervical Spine Finite Element Model (Specific Aim 1)) was modified to reflect injured ligament properties. As stated in Specific Aim 3, the intact model was adapted to reflect partially (hyperstrained) and fully injured (transected) ligaments. Eight versions of the FE model were created and analyzed with injuries at the C5-C6 level: 1) partial FC injury, 2) full FC injury, 3) partial FC and ALL injury, 4) full FC and ALL injury, 5) partial LF and full ISL injury, 6) full LF and ISL injury, 7) partial FC, ALL, LF, and full ISL injury, and 8) full FC, ALL, LF, and ISL injury. Ninth and tenth models were created with partial and full injuries to the C1-C2 FC and right alar ligaments.

Uncertainty with respect to intertransverse tissue damage (including the intertransversarii muscles, intertransverse ligaments, and the vertebral artery) existed due to a lack of clinical data. Due to this ambiguity, these tissues were left intact in both the experimental and computational simulations. For the FE model, spring elements (type: SPRINGA) were placed between the transverse processes at the C4-C5, C5-C6, and C6-C7 levels to represent the passive stiffness of the muscles and aforementioned tissues. Measurements of the cross-sectional area of the tissues in conjunction with existing passive muscle tissue stiffness data indicated that 25 N/mm was an appropriate stiffness for these spring elements [122].

In the interest of computational efficiency, the C5-C6 injuries were simulated on models based on the lower cervical (C3-C7) model. Likewise, the alar ligament injuries were replicated with the upper cervical (C0-C3) model. A pilot study found that pursuing the model into two less computationally-expensive segments had no effect on the predicted data from the injured levels. The stiffnesses and toe lengths of the ALL, LF, and right alar ligaments in the partial-injury models were adjusted to reflect the percentage stiffness reductions and toe length increases

that were measured experimentally (see section 3.2 Experimental Measurement of Injured Ligament Mechanical Properties (Specific Aim 2)). Fully-injured ligaments were simulated by specifying zero stiffness for the representative spring elements. All injured ligaments were specified with zero preload force. To fit whiplash-type injury pathology, the FC ligaments were assumed to have undergone similar injury to the ALL ligaments, with stiffness and toe regions adjusted by the same percentage as the ALL. Due to the whiplash pathology, the FC and ALL ligaments were not expected to suffer damage independent of each other. However, exclusive FC injuries were simulated as this allowed direct comparison to the cadaveric, pure-moment loaded, experimental FC ligament-sectioning tests. For the hyperflexion-type injuries, whiplash pathology predicted the ISL to be completely compromised, so the spring elements representing the ISL were given zero stiffness at the level of partial LF injury [46, 85].

### **3.3.2 Ligamentous Injury Cervical Spine Finite Element Model Analysis**

Analysis of the injured-ligament models proceeded identically to the intact models with the exception of moment magnitude. The peak moment was reduced to 0.75 Nm from 1.5 Nm since a pilot study indicated the additional compliance of the ligamentously-injured spine increases ROM over the intact case for a given moment magnitude. Furthermore, previous experimental studies have found that the severely injured spine is incapable of surviving a 1.5 Nm moment without catastrophic tissue failure [86]. Correspondingly, rotations were tabulated at -0.75, -0.4, -0.25, -0.1, 0, 0.1, 0.25, 0.4, and 0.75 Nm.

### **3.3.3 Ligamentous Injury Cervical Spine Finite Element Model Experimental Validation**

#### **Method**

Experimental validation of the partial-injury models was impossible since the ligaments necessitated excision from the spine to be artificially injured. However, the full-injury models could be simulated by scalpel transection of the cadaveric ligaments whilst located in the full spine.

Immediately subsequent to intact pure-moment testing, the cadaveric full-cervical spines (see section 3.1.4 Intact Cervical Spine Finite Element Model Experimental Validation) were modified to simulate four ligamentous injuries. One of the aforementioned spines was used for an altered ligament-sectioning sequence in pilot testing and was not included in the “Ligamentous Injury” dataset. The initial injuries were replicated with serial ligament-sectioning via scalpel at the C5-C6 level. Cases were tested in the order of: 1) sectioned FC, 2) sectioned FC and ALL, and 3) sectioned FC, ALL, LF, and ISL. The remaining intertransverse tissues were left intact. The fourth and final injury configuration was accomplished by sectioning both the occipital (C0-C2) and atlantal (C1-C2) portions of the right alar ligament through a slit in the tectorial membrane. The pure-moment testing procedure of the full-injury, full-cervical spines was identical to that of the intact, full-cervical spines other than the reduction of applied moment from 1.5 Nm to 0.75 Nm.

Intervertebral rotations were measured as in the intact case. Additionally, digital radiographs were taken of the spine in the intact case and following each ligamentous injury at the C5-C6 level. These radiographs were taken from the lateral viewpoint as the spine was loaded at a steady-state 0.75 Nm in flexion and extension, and the frontal viewpoint for  $\pm 0.75$  Nm loadings in the lateral bending directions. The images were subsequently utilized in Specific Aim 4 for enhancing radiologic diagnosis.

### 3.3.4 Ligamentous Injury Cervical Spine Finite Element Model Analytic and Experimental Validation Results

#### 3.3.4.1 C5-C6 Injuries

Sectioning of the ligaments at the C5-C6 level produced progressively more ROM as predicted by the FE model and measured experimentally (Figures 43-45). As expected, partial ligamentous injury resulted in ROM between that of the intact and fully-injured cases. As predicted by the FE model, the ROM resulting from the partial injuries more closely approximated the fully-injured cases than the intact cases.

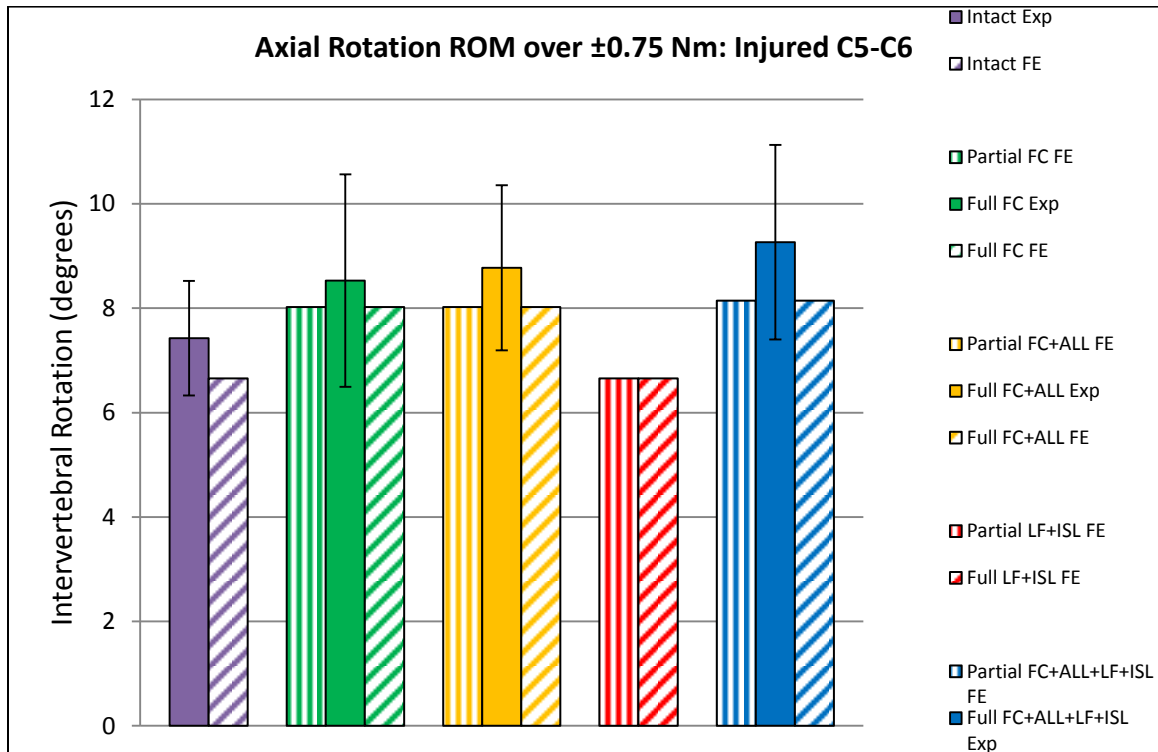


Figure 43: Experimentally-measured (Exp) and FE-predicted C5-C6 summed biaxial rotations for various ligamentous injuries at 0.75 Nm loading. Standard deviation bars are shown for experimental data.

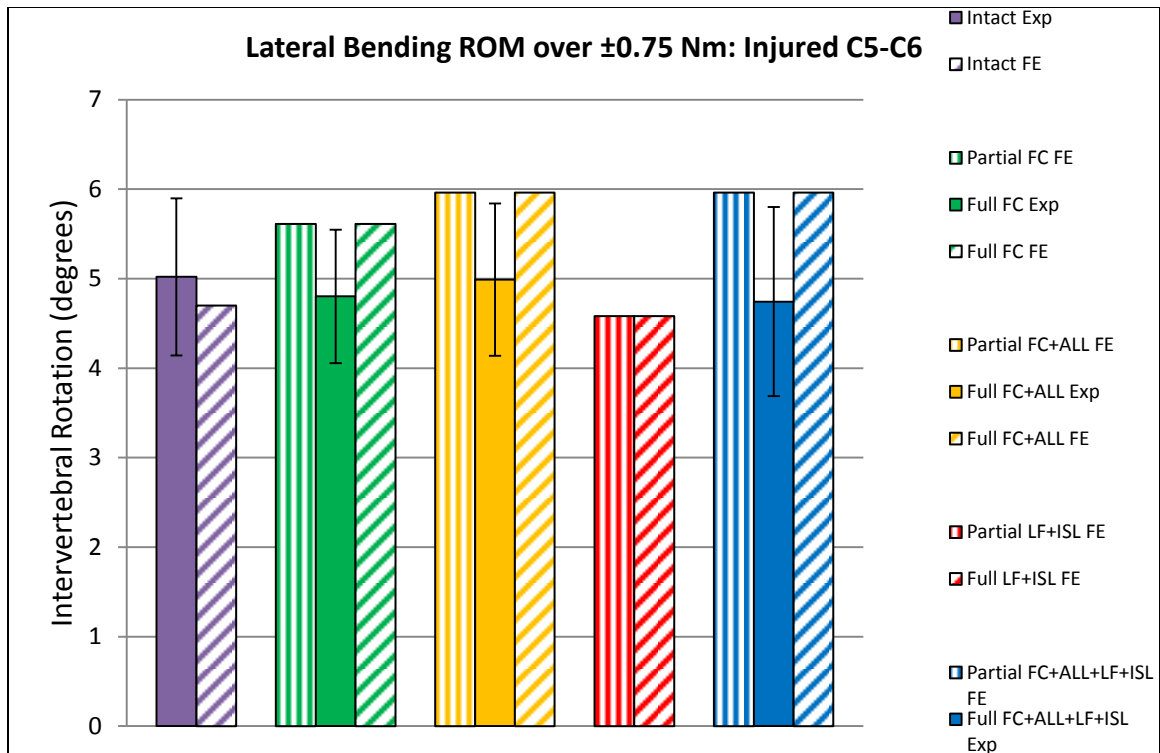


Figure 44: Experimentally-measured (Exp) and FE-predicted C5-C6 summed bilateral bending rotations for various ligamentous injuries at 0.75 Nm loading. Standard deviation bars are shown for experimental data.

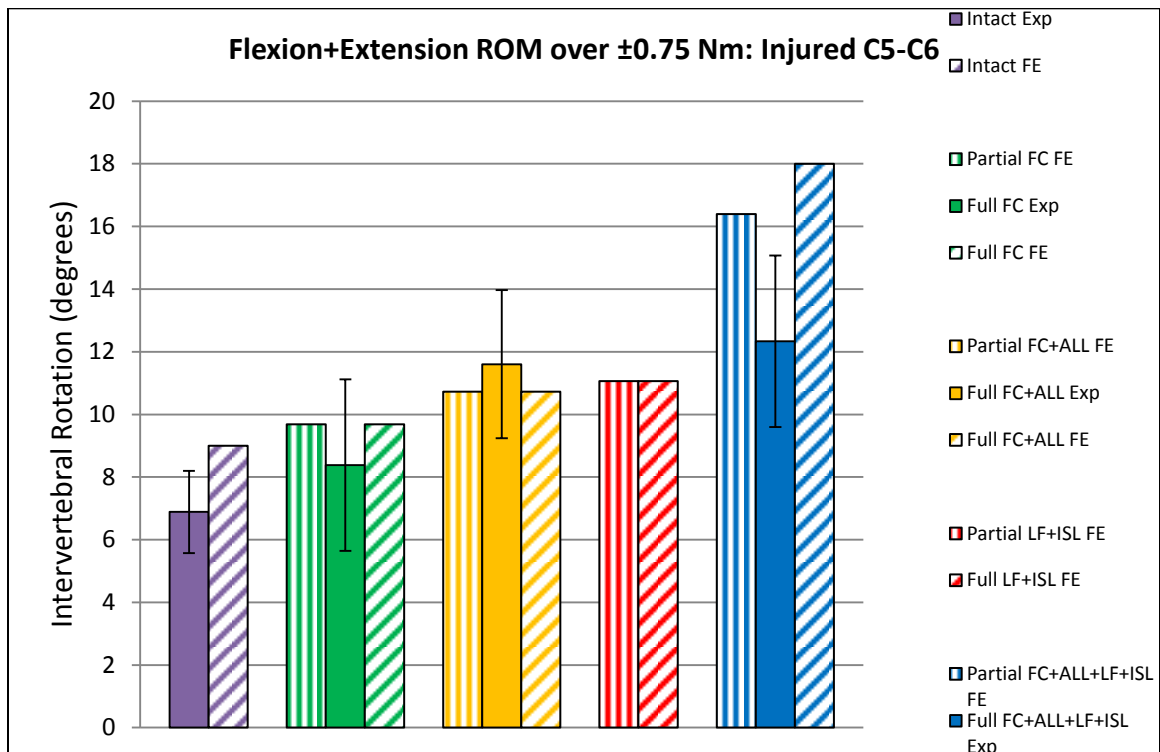


Figure 45: Experimentally-measured (Exp) and FE-predicted C5-C6 summed flexion+extension rotations for various ligamentous injuries at 0.75 Nm loading. Standard deviation bars are shown for experimental data.

The percentage increase in flexion+extension ROM over the intact case due to the FC+ALL partial injury is very similar to those reported from 8g hyperextension simulations (FC+ALL injury: 19.2% increase, hyperextension simulation: 15.9%) [44]. The referenced simulations tested and injured the entire cadaveric spine experimentally, including the intervertebral discs. These studies also demonstrated very similar ligamentous extension to the current study during the injury mechanism, which likely induced comparable ligamentous partial damage (see section 3.2.3 Injured Ligament Properties Experimental Results). The similarity of those ROM measurements to the current study, where the intervertebral disc was modeled as intact, indicates that the ligaments are the primary contributor to cervical stability. However, in the case of extreme ligamentous injury (FC+ALL+LF+ISL) it is evident that other tissues are recruited to provide support once the extreme values of flexion and extension are obtained. This assertion is supported by comparing the FE-predicted and experimental data. The supplementary supportive tissues that limit motion at the ROM extrema are likely passive muscles, vascular tissues, and possibly even the spinal cord. The required sophistication to consider these tissues in an FE model is formidable. Furthermore, experimentally attempting to apply only pure moments throughout the very large ROM present in this extreme injury is very difficult without introducing a substantial loading artifact.

The relative uniformity in lateral bending ROM between injury cases can be attributed to the connective tissues between the transverse processes. The lateral location of these tissues provides for a great deal of stiffening, particularly in the lateral bending direction. The stiffening effect is large enough to shield the contributions of the other ligaments, such that sectioning of the other cervical ligaments does not appreciably alter the spine's compliance in lateral bending [32, 99, 119]. Sparse data exist on the frequency of tissue damage in this anatomical location from whiplash trauma. However, severe (8.5 g) whiplash trauma has been found to substantially

increase the elongation of the vertebral artery between C0 and C6, from its typical physiologic extension of 5.8 mm to 14.8 mm (155% increase) during the trauma event [75]. This elongation has great potential to tear the adjacent intertransverse ligament and intertransversarii muscle, neutralizing the stiffening effect [30, 70]. Given the extreme difference between the passive muscular tissue available for *in-vitro* testing and the potentially active muscle tissue in an actual whiplash situation, it is difficult to experimentally determine the likelihood of muscular injury [122]. Further study of these tissues post-trauma is vital. While intertransverse tissue injury had no effect on flexion+extension ROM, it provided a notable increase in axial rotation ROM, and a very large increase in lateral bending ROM (Figures 46-48).

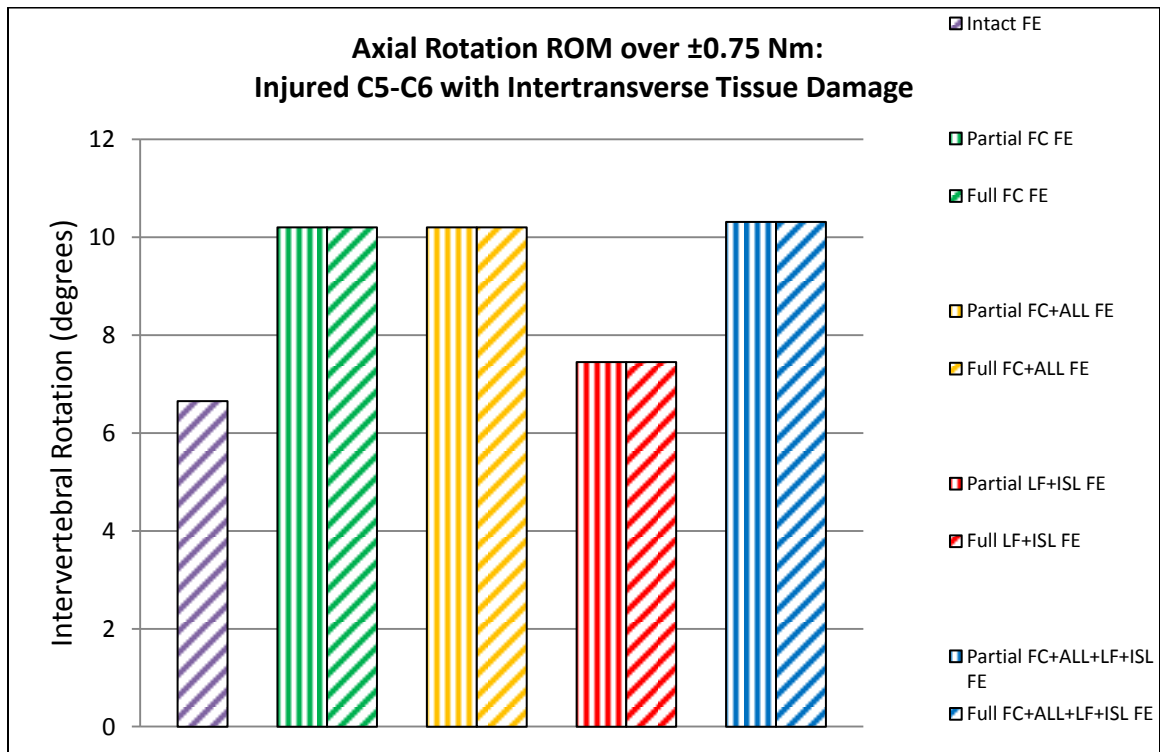


Figure 46: FE-predicted C5-C6 summed biaxial rotations for various ligamentous injuries with intertransverse tissue damage at 0.75 Nm loading.

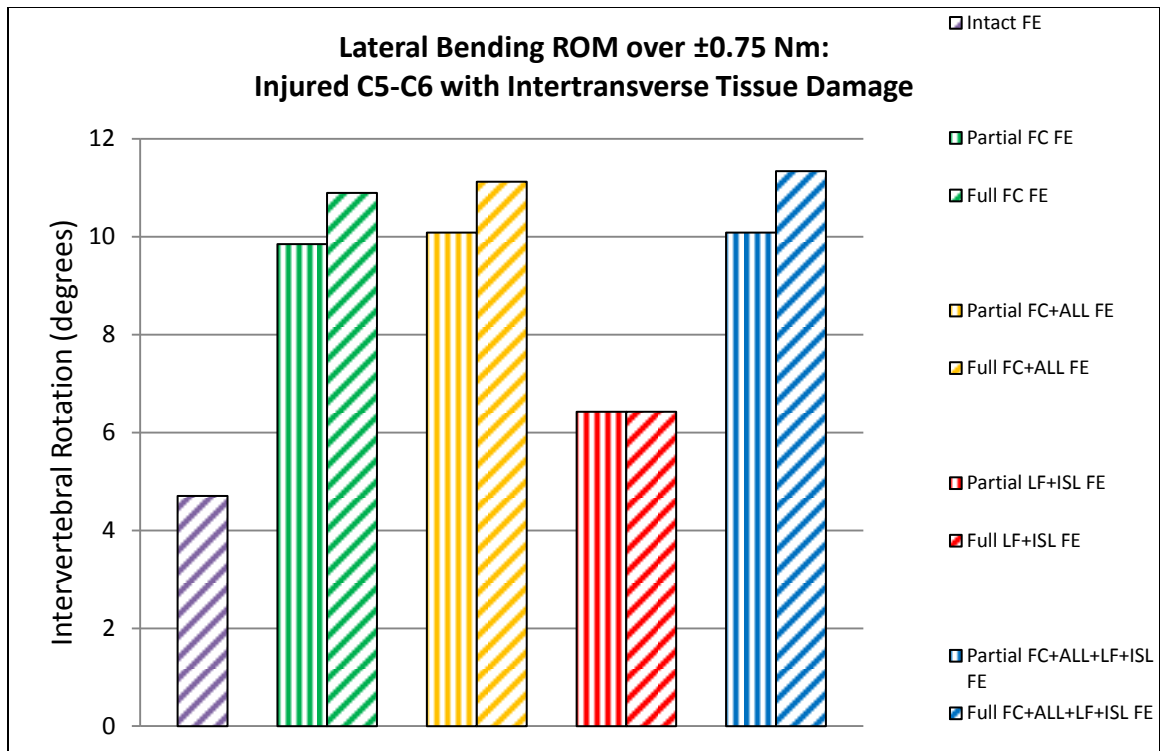


Figure 47: FE-predicted C5-C6 summed bilateral bending rotations for various ligamentous injuries with intertransverse tissue damage at 0.75 Nm loading.

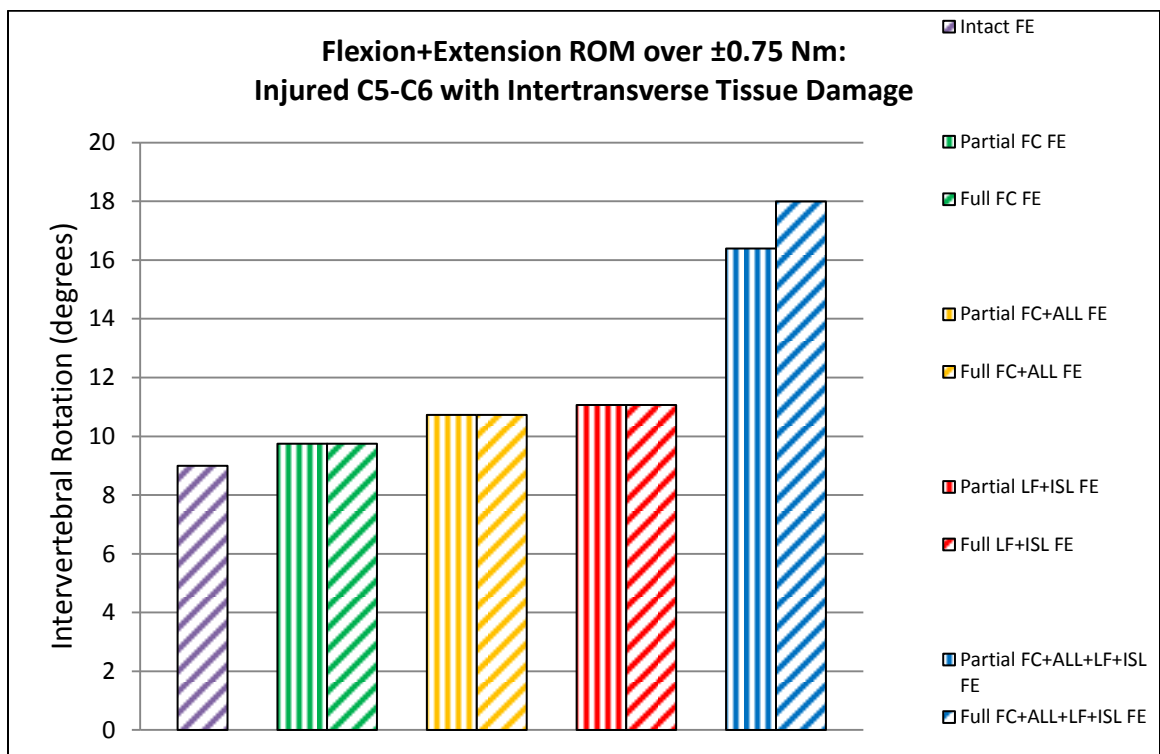


Figure 48: FE-predicted C5-C6 summed flexion+extension rotations for various ligamentous injuries with intertransverse tissue damage at 0.75 Nm loading.

It is apparent from the ROM data that the FC ligaments substantially contribute to stability of the spine. Experimental injury simulation of these ligaments was desired, but the experimental replication of the simultaneous tangential and tensile loading experienced by the FC ligaments would have been intractable with our current experimental apparatus. This concern is mitigated by the near-universal finding of substantial FC damage in severe whiplash injury cases [85, 110, 131, 137]. Additionally, the FE model predicted the FC ligaments will strain beyond the previously reported FC partial damage threshold of 35-64.8% when the vertebral bodies rotate to reach the strains this study found to induce partial damage in the ALL [15, 58, 94]. Previous experimental studies of the FC ligaments have also found a distinct discontinuity in their force/displacement curves, indicating partial damage [107, 123]. This type of event was detected in the ligamentous force/displacement curves of the current study, where it also signified partial ligament damage (see section 3.2.3 Injured Ligament Properties Experimental Results). Thus, the assumption that the FC ligaments sustain comparable partial damage along with the ALL is justified.

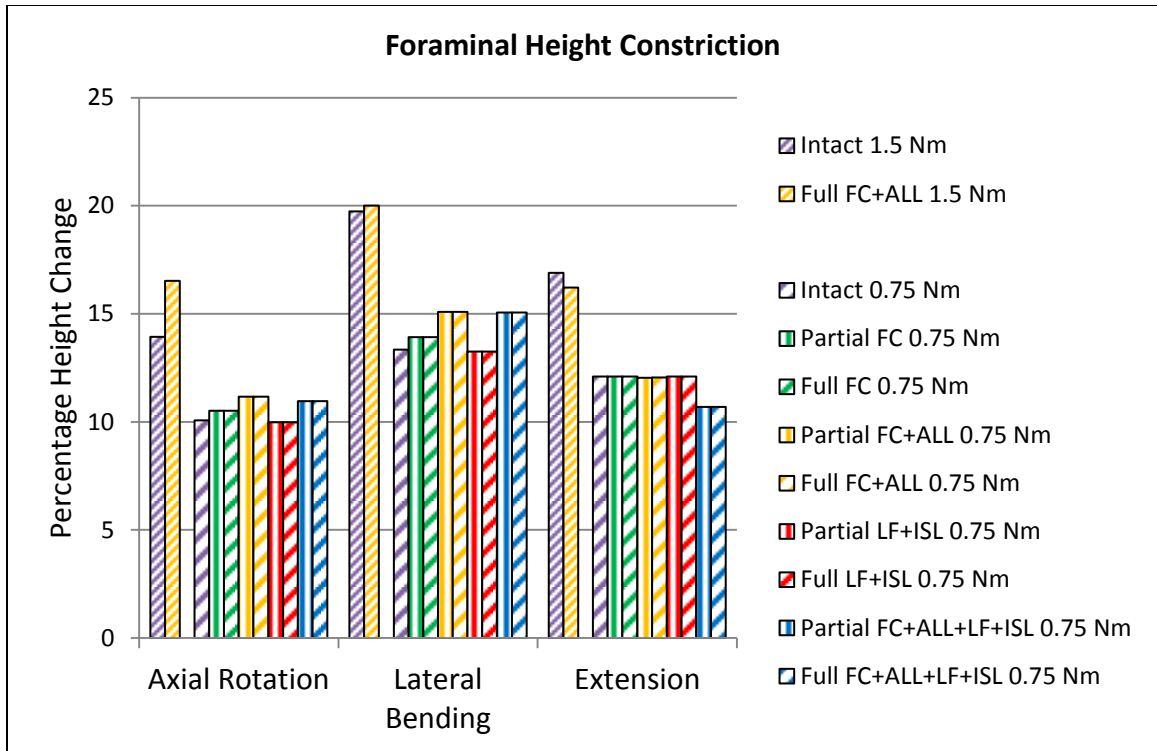


Figure 49: FE-predicted change in left C5-C6 intervertebral foramen height for various injuries due to the application of a 0.75 Nm moment. The intact and full FC+ALL injury spines loaded with 1.5 Nm moments are also shown for comparison.

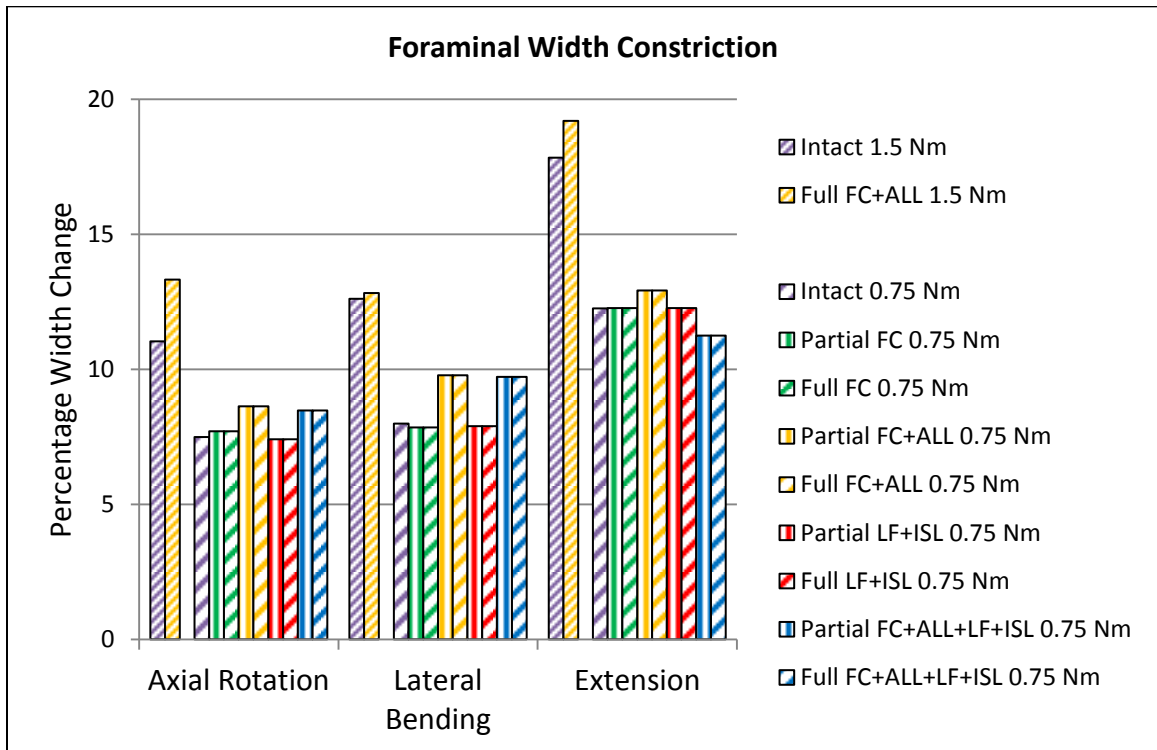


Figure 50: FE-predicted change in left C5-C6 intervertebral foramen width for various injuries due to the application of a 0.75 Nm moment. The intact and full FC+ALL injury spines loaded with 1.5 Nm moments are also shown for comparison.

Intervertebral foramen measurements did not meet radiculopathy criteria for any of the ligamentous injuries (Figures 49 and 50, see section 3.1.3 Intact Cervical Spine Finite Element Model Analysis) [83]. In general, the amount of foraminal constriction was proportionate with the ROM measured at C5-C6. Thus, the foraminal space was most reduced in cases where the intertransverse tissues were injured in addition to the ligaments (Figures 51 and 52). In this axial rotation loading case, the FC+ALL injured spine demonstrated more foraminal restriction at a 0.75 Nm moment than the intact spine at a 1.5 Nm moment. To further investigate the radiculopathic potential of FC+ALL injuries, the full FC+ALL injury case was also analyzed at 1.5 Nm loadings. In this scenario, 1.5 Nm moments resulted in motions which constricted the foramen almost to the threshold of radiculopathy. Lateral bending particularly decreased foraminal height (23.89% reduction compared to the 32% radiculopathy threshold), while extension posed a risk to foraminal width clearance (19.19% reduction compared to 28% threshold). However, this prediction of radiculopathic absence is made assuming the patient presents average-sized spinal ganglia and intervertebral foramina. If the ganglia are disproportionately large compared the foramina, as is often found, the risk of radiculopathy is increased greatly [83]. If this patient scenario applies, or any sort of excessive cervical motion is experienced during the healing period, it appears as though the FC+ALL injuries may result in deleterious radiculopathy. Thus, stabilization of the FC+ALL injured spine appears necessary to prevent neurological deficit.

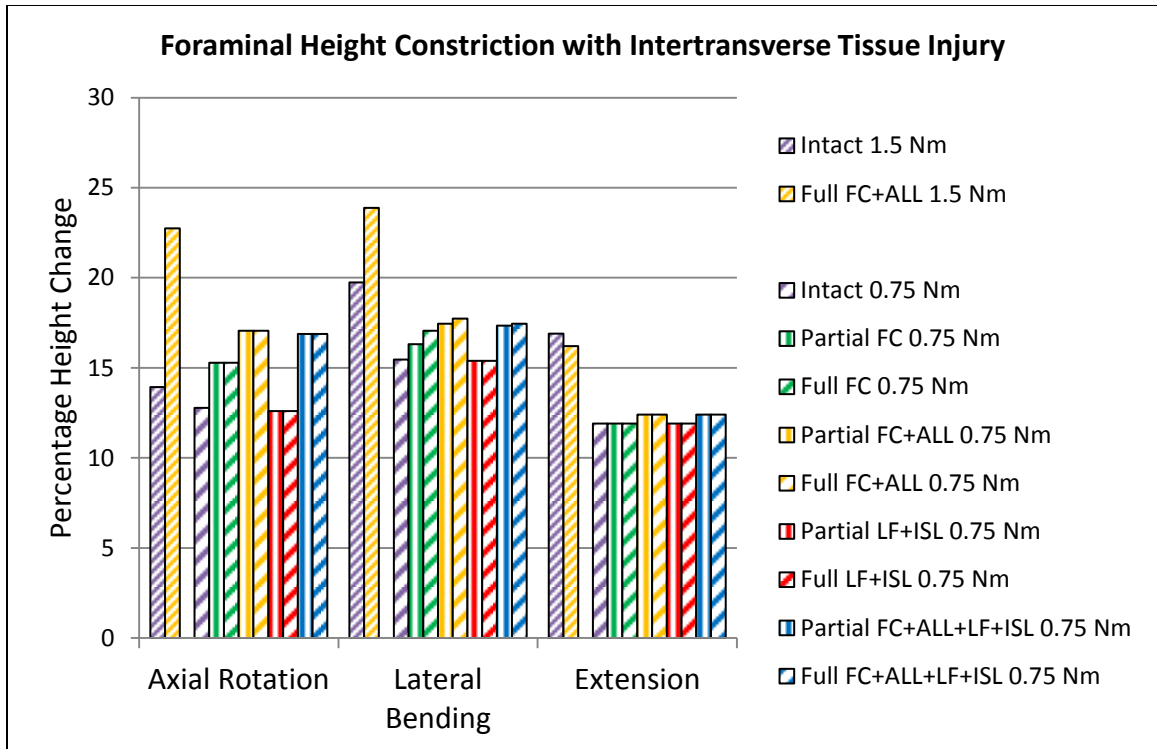


Figure 51: FE-predicted change in left C5-C6 intervertebral foramen height for various injuries with intertransverse tissue injury due to the application of a 0.75 Nm moment. The intact and full FC+ALL injury spines loaded with 1.5 Nm moments are also shown for comparison.

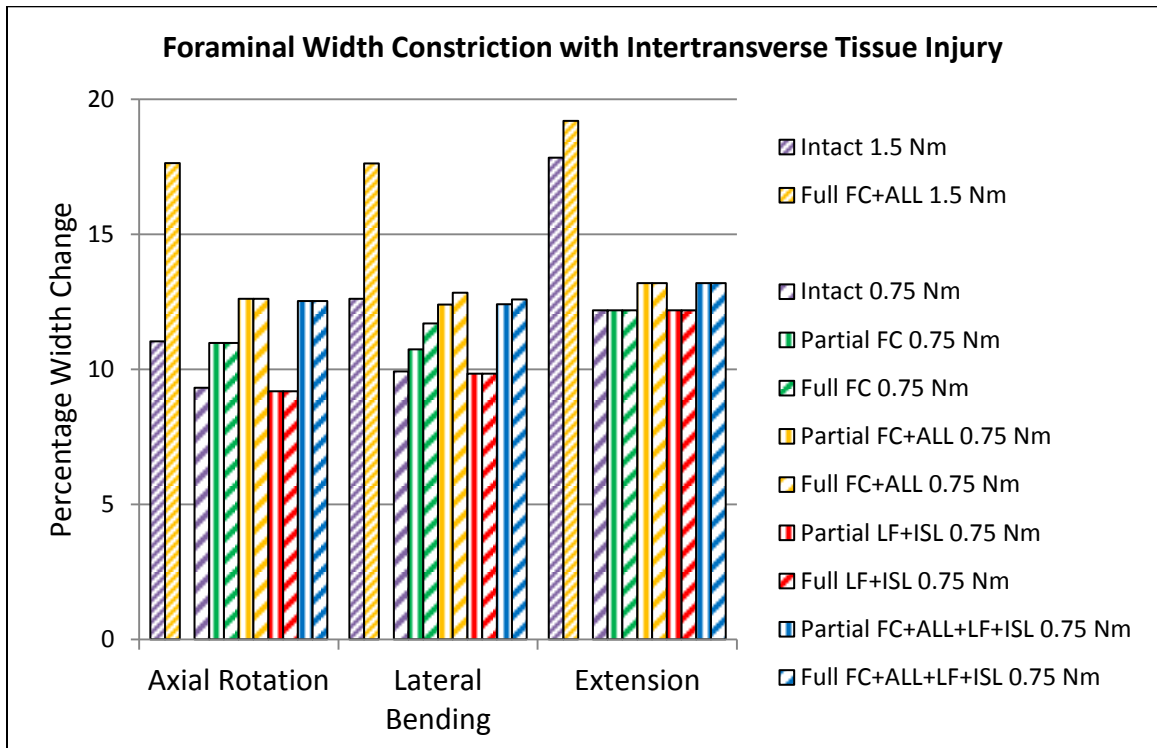


Figure 52: FE-predicted change in left C5-C6 intervertebral foramen width for various injuries with intertransverse tissue injury due to the application of a 0.75 Nm moment. The intact and full FC+ALL injury spines loaded with 1.5 Nm moments are also shown for comparison.

Interestingly, the combination of LF+ISL injuries with FC+ALL injuries often alleviated the issue of foraminal space reduction. Observing the relative motion between the C5 and C6 vertebrae, it is evident that the posterior ligaments (LF and ISL) act as a tether between the two vertebrae. When these ligaments are injured, the two vertebrae are not held together as tightly in the axial direction, which subsequently increases the foraminal space. It should be noted that the unloaded foraminal dimensions for all injury cases were identical to those of the intact case. Other than the aforementioned role in FC+ALL+LF+ISL injuries, the LF+ISL ligaments appear to contribute very little to foraminal constriction. For all ligamentous injuries, the differences in foraminal constriction between the full and partial injury cases were negligible.

#### **3.3.4.2 C1-C2 Injuries**

Ligament sectioning at the atlanto-axial joint provided different ROM trends to those in the lower cervical spine. Removal of each ligamentous structure subsequently increased the ROM at C1-C2 in axial rotation, but the other bending directions behaved differently (Figure 53). Interestingly, the ROM in both lateral bending and flexion+extension increased after sectioning of the C1-C2 facet capsule ligaments, but decreased when the right alar ligament was cut. These findings were also mirrored by very similar studies conducted by Crisco *et al* and Panjabi *et al* [21, 79]. The reduction in ROM in the lateral bending and flexion+extension directions was attributed in these studies to a kinematic change that altered the relative motion paths between the adjacent vertebrae, effectively decreasing the ROM over the intended bending axis. This phenomenon was also observed during the current cadaveric testing. The inability of the extremely compliant, injured atlanto-axial joint to maintain a neutral orientation caused the moments to be delivered in directions that were not in perfect alignment with the desired bending axes. The virtual loading axes of the FE model were not subject to this drift, and did not generate the phenomenon.

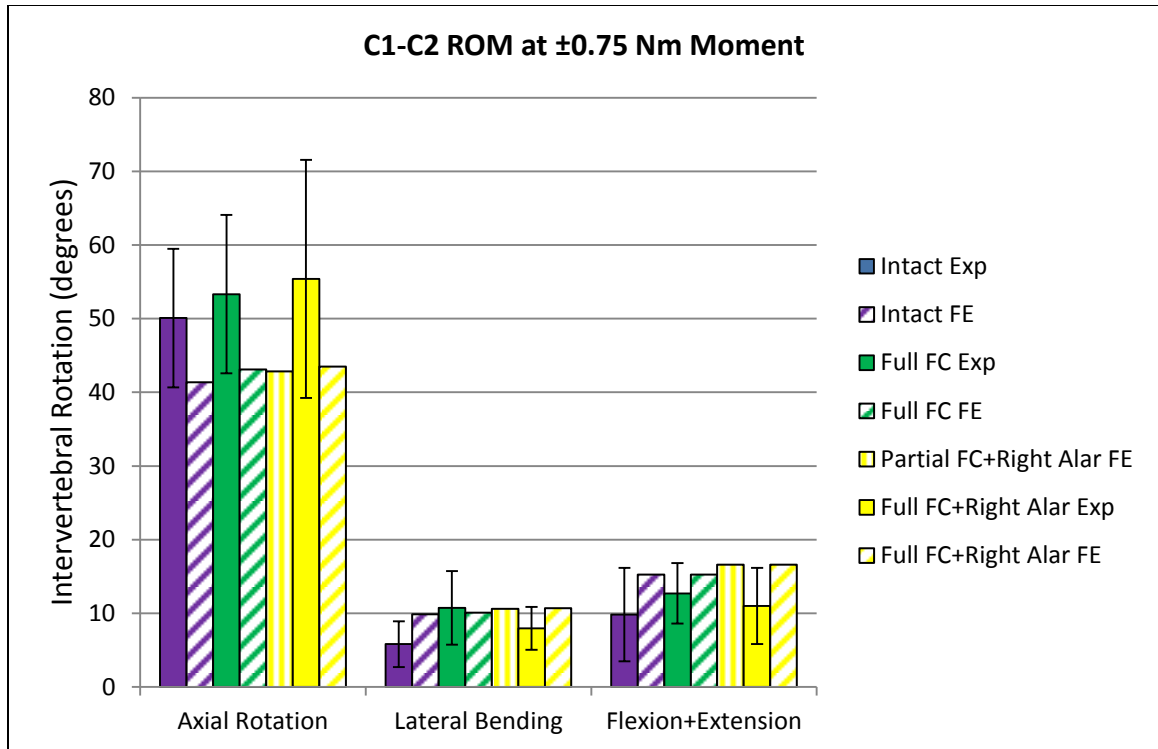


Figure 53: Experimentally-measured (Exp) and FE-predicted C1-C2 summed intervertebral rotations for various ligamentous injuries at 0.75 Nm loading. Standard deviation bars are shown for experimental data.

Due to the alar ligament's connection between C2 and C0, ROM at the C0-C1 joint was also studied (Figure 54). Although an increase in axial rotation ROM was expected due to sectioning of the alar ligament, transecting the C1-C2 facet capsule ligament unexpectedly increased the C0-C1 axial rotation ROM as well. In the lower cervical spine, increasing the compliance at an intervertebral level generally decreases the ROM at adjacent levels. The opposite trend found here in the upper cervical spine may result from the alar ligament's attachment to both C0 and C1. As seen at the C1-C2 joint, experimentally-measured ROM increases over the two other bending axes after C1-C2 capsular ligament injury, but decreases following alar ligament sectioning.

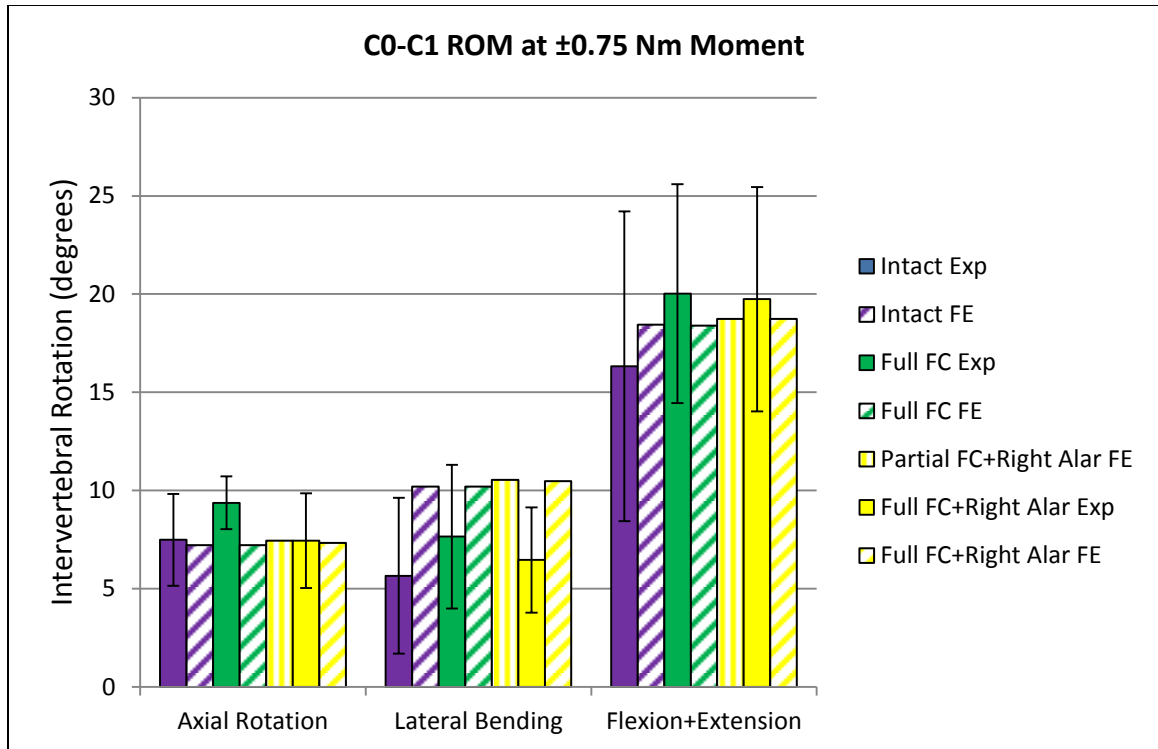


Figure 54: Experimentally-measured (Exp) and FE-predicted C0-C1 summed intervertebral rotations for various ligamentous injuries at 0.75 Nm loading. Standard deviation bars are shown for experimental data.

A hidden benefit of ligament sectioning was employed for the experimental validation of the finite element models. Sectioning of the ligaments allowed the individual structural contribution of each of the ligaments to be visible. This is in contrast to studying the kinematics of the overall structure. Thus, while the model was validated with respect to several ligamentous injury scenarios, appropriate specification for each individual tissue was ensured. This “piecemeal” approach can be an effective method for validating models of a wide variety of structures, and it is a recommended technique for experimental validation of future complex FE models.

### **3.4 Comparison of Cervical Spine Finite Element Models in Pursuit of an Enhanced Diagnostic Procedure (Specific Aim 4)**

#### **3.4.1 Diagnostic Enhancement Analytical and Experimental Method**

The ROM data calculated in pursuit of Specific Aim 3 were analyzed across all three loading directions. The aggregate responses over all of these loading conditions were compared between the specific injuries. These responses were compiled into a flowchart, allowing logical diagnosis of specific ligamentous injuries from standard ROM tests through the lateral bending and flexion+extension directions.

The previous FE simulations were also analyzed for excessive strains (maximum and minimum principal strain) in the annulus fibrosus and excessive contact stresses in the facet cartilage. Initially, the nodal locations of both maximum and minimum principal strains in the annulus were located. In all simulations, the strain extrema were situated on the exterior surface of the annulus. Accordingly, four elements surrounded each of the nodes. To minimize potential errors due to artificial stress concentrations, the nodal strains at each point of these four elements were averaged prior to reporting.

Contact stresses at the facets were noted at their peak nodal values. Due to the relatively simple geometry of the facets, there was no need to average the stresses among the surrounding elements. For all simulations, at least one adjacent node displayed strains within 15% of the peak value, reducing the likelihood of an artificial stress concentration.

The values for annular strain and facet cartilage stress at 0.75 Nm were denoted as “excessive” if they surpassed the values found in the intact spine at a 1.5 Nm moment. Similarly, injuries that allowed the intervertebral foramina dimensions to constrict beyond the intact 1.5 Nm case were documented. If any of these three scenarios applied, cervical stabilization was recommended.

In order to prove the viability of using radiography to measure the aforementioned ROM response, Cobb angles were graphically measured from the radiographs taken during pure-moment ROM testing (ImageJ V1.44p, National Institutes of Health, Bethesda, MD; Figure 55). The change in C5-C6 angles between the positive and negative 0.75 Nm moments were measured for each injury. Each graphical reading was repeated twice to minimize visual error. The readings were then averaged for reporting. The x-ray source blocked the motion analysis cameras while it was in place for imaging (Figure 56). Thus, the Cobb angular measurements were correlated *post-hoc* to the intervertebral rotations measured at  $\pm 0.75$  Nm by the stereophotogrammetric motion analysis system during the pure-moment ROM testing. Two flexion and extension images were unusable due to equipment malfunction, and one lateral bending radiograph was unreadable owing to blocking of anatomic landmarks by the motion analysis triad-carrying wires.



Figure 55: (Left) Intervertebral angles were measured in flexion and extension by comparing the angles made between the yellow lines at  $\pm 0.75$  Nm. These lines were drawn between the anterior/caudal endplate and the posterior/cranial wall of the spinal canal. (Right) A similar procedure was used to measure intervertebral angles in lateral bending. These lines were drawn between the uncinat processes.

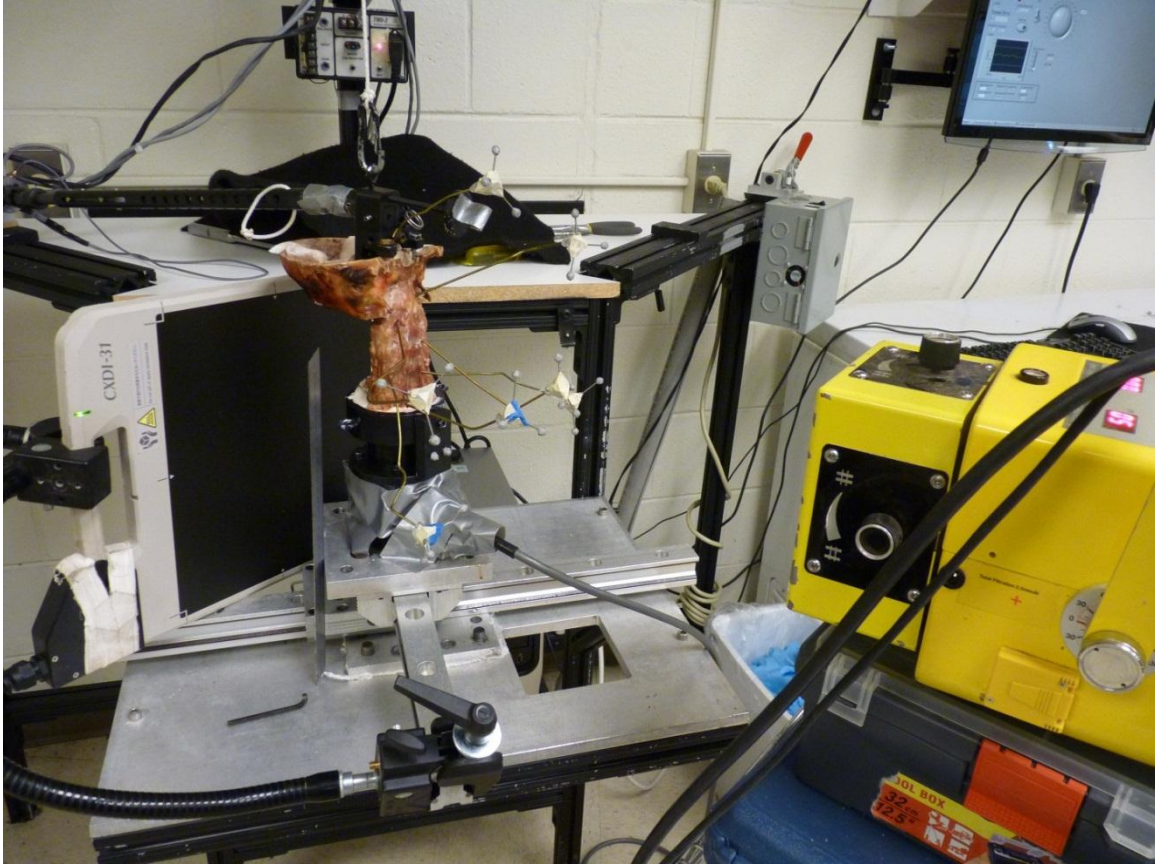


Figure 56: Radiographs were taken of the spines while under steady-state, pure-moment loading. The x-ray radiation source (the yellow box at right) blocked the motion analysis markers when in use.

### 3.4.2 Diagnostic Enhancement Analytical and Experimental Results

Comparison between the various injury cases revealed indistinguishable ROM for some loading cases, but noticeable differences for other loading scenarios (Figure 57). The difference between partial and full ligamentous injury on ROM is negligible. Previously, it was shown that both ligamentous injury variants produce similar foraminal constriction, and thus will likely require similar stabilization techniques.

It is critical to note that the FC+ALL and LF+ISL ligamentous injuries result in nearly indistinguishable flexion+extension ROM despite the injuries resulting from two different conditions (rear impact and frontal impact, respectively). Since these two types of trauma

typically damage different ligamentous structures, contrasting treatment regimens may be required for each injury type. Only when measuring the flexion and extension ROM independently are the differing effects of the injuries revealed. Specifically, the FC+ALL injuries (regardless of intertransverse tissue injury) yielded a larger increase to extension ROM over intact cases than the LF+ISL injuries (1.15 vs 0 degrees). This effect was reversed for flexion loadings (0.58 vs 2.07 degrees). However, it is difficult to determine when the spine passes from flexion to extension without knowing the neutral position of the intact spine, which varies between patients. Without this knowledge, the common flexion and extension ROM test does not appear to be a good indicator for diagnosing specific injuries. In contrast, ROM in both the lateral bending and axial rotation directions showed a more substantial difference between the LF+ISL and FC+ALL injuries (lateral: 4.58 vs 5.96 degrees, respectively; axial: 6.65 vs 8.02, respectively). If the intertransverse tissues are damaged, the lateral ROM difference is 6.42 vs 10.08 degrees, and the axial rotation ROM shows a contrast of 7.45 vs 10.20 degrees (Figure 58). These data suggest ROM tests should not be limited to only flexion and extension, as is often the case [109].

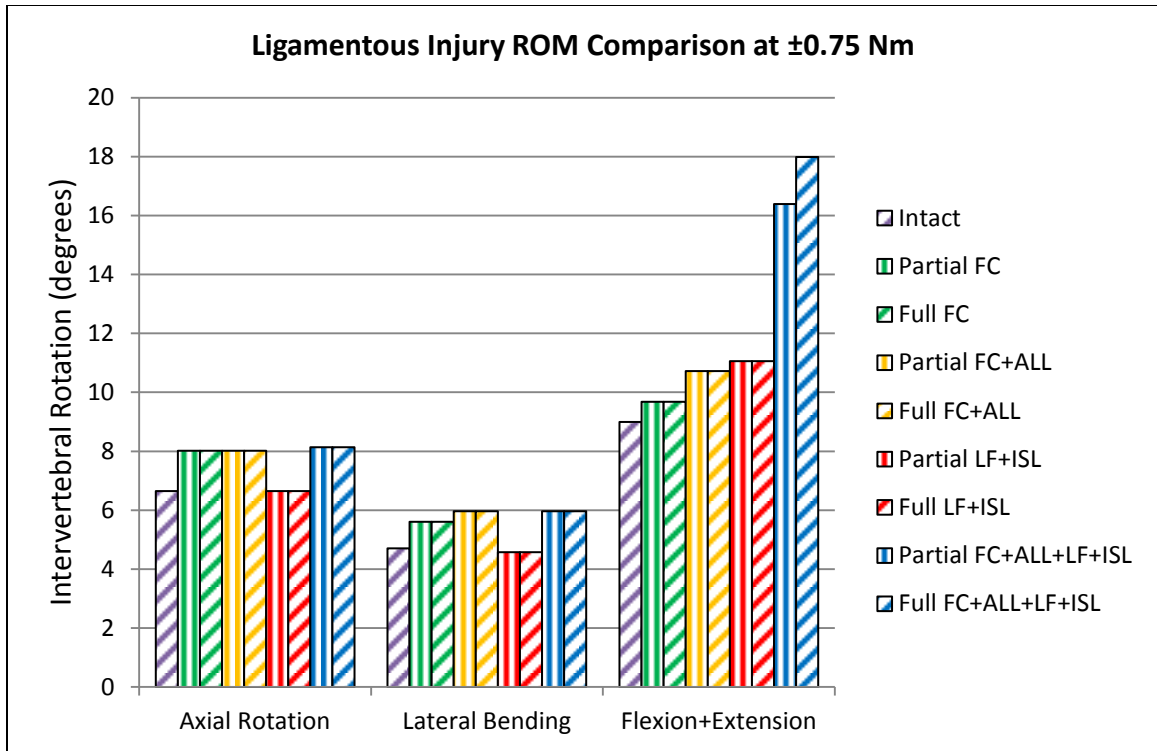


Figure 57: Comparison of FE-predicted C5-C6 intervertebral rotations for the various ligamentous injuries due to a 0.75 Nm moment.

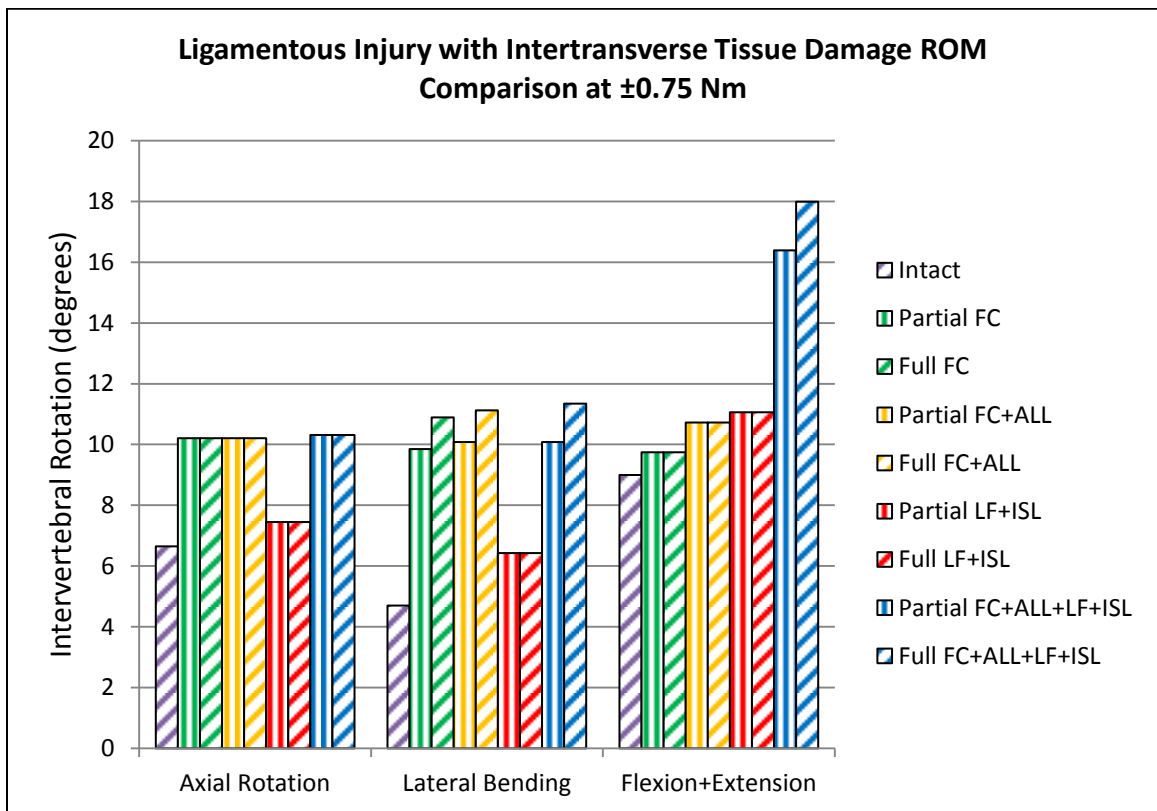


Figure 58: Comparison of FE-predicted C5-C6 intervertebral rotations for the various ligamentous injuries with intertransverse tissue damage due to a 0.75 Nm moment.

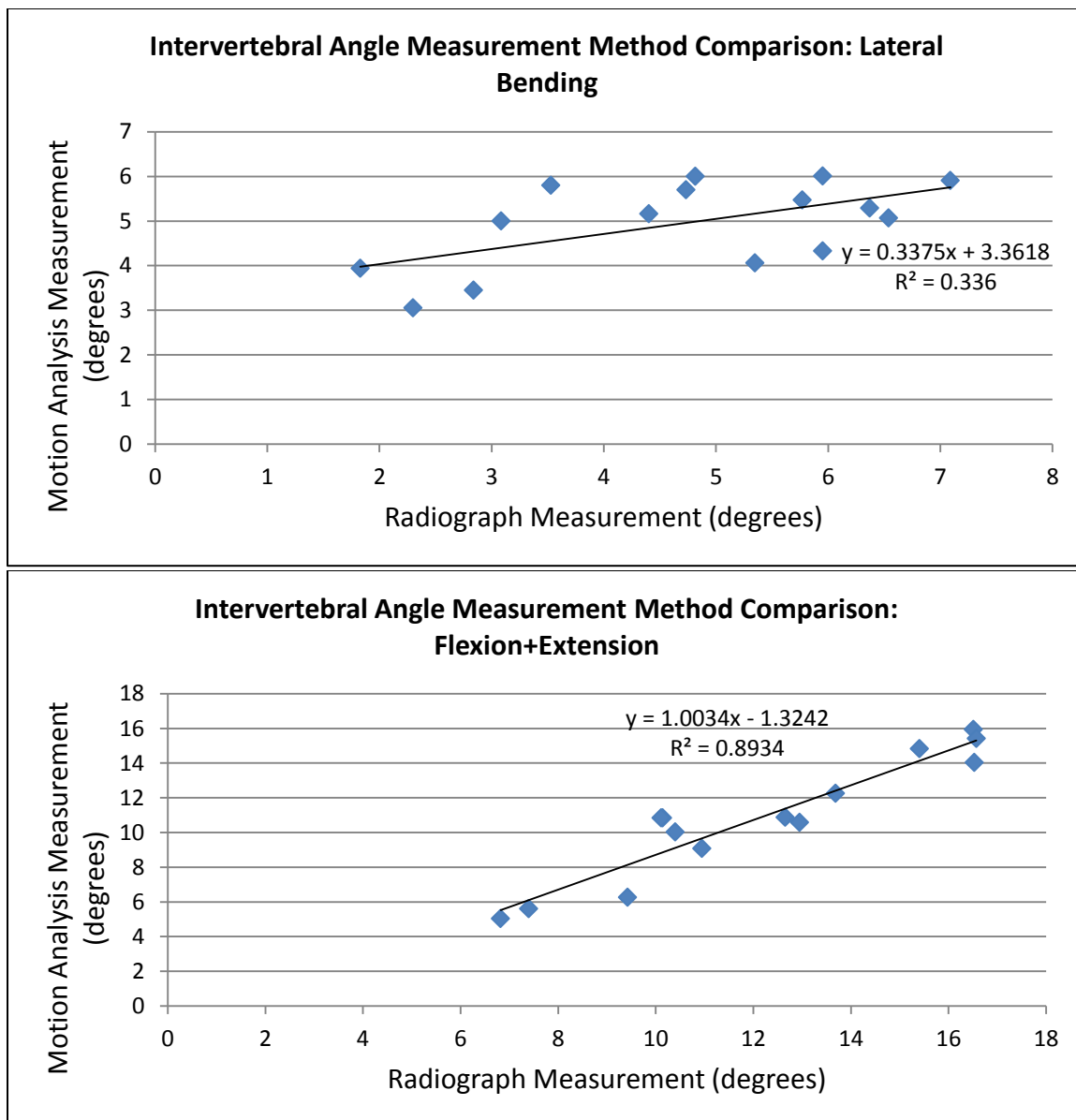


Figure 59: Comparison between intervertebral angle measurements made by the stereophotogrammetric motion analysis system and graphical measurements from radiographs.

The radiographic measurements correlated acceptably with the stereophotogrammetric motion analysis data when measuring flexion and extension ROM (Figure 59). A linear trendline fitted to the readings exhibits a slope of 1.0034, when a slope of 1.00 is expected for exact agreement between the two measurement methods. However, the lateral bending measurements do not show the same correlation reliability. This is largely due to the quality of the radiographs. The images created in this study have poor resolution compared to the

radiographs created in a typical clinical setting by professional radiologists. Additional difficulties stem from the smaller ROM found in lateral bending; the resolution is a higher percentage of the total ROM. If the lateral ROM was larger due to intertransverse tissue damage (as seen in Figures 46-48), the correlation reliability is expected to increase.

The arrangement of the data into a clinical diagnostic tool was accomplished using percentage enlargements of the intervertebral ROM due to the specific injuries (Figure 60). This method allows clinicians to continue to utilize their favored datasets which define “normal” intervertebral flexibility. It also allows different methods of ROM measurement, whether intervertebral rotations are calculated from Cobb angles, span length between spinous processes, or other means.

If intertransverse tissue damage occurs, all injuries other than the LF+ISL injuries result in excessive maximum and minimum principle strains in the annulus for the lateral bending direction. The full FC+ALL injuries provide for the largest maximum principle strain (40.2% versus 32.4% for the intact 1.5 Nm case). The axial rotation, flexion, and extension directions did not allow strains to go beyond the intact case for any injury.

Cartilage contact stress was largest in the full FC injury case. Stresses of 2.70 MPa were measured in the facets in lateral bending, compared to 1.82 MPa for the intact case. The full FC+ALL case created the second largest facet stress magnitude (2.57 MPa). As before, the other bending directions did not result in stresses beyond the intact case.

As previously disseminated in Figures 51 and 52, the intervertebral foraminal dimensions are reduced below intact levels for all but the LF+ISL injuries. Summarizing the foraminal constriction and tissue stress/strain trends, it appears as though hyperextension injuries are more likely to require cervical stabilization than hyperflexion-type injuries. Another observation is that post-injury flexion and extension motion was not found to portend any risk to the

annulus, cartilage, or neural tissue at 0.75 Nm loadings. Accordingly, it may be beneficial to design cervical stabilization devices to allow freer motion about this axis. This feature would likely provide for greater patient comfort, and potentially minimize the long-term loss of ROM often observed after healing [3, 10].

It appears that the healthy intertransverse tissues are able to provide adequate support to the spine in the presence of ligamentous injury. This conclusion is supported by the data wherein annular strain, cartilage contact stress, and foraminal constriction were all within physiological limits. However, comparing this minimal foraminal constriction with the actual clinical prevalence of radiculopathic symptoms after whiplash injury may indicate damage to the intertransverse tissues is common [25].

The magnitude of elevated annular strains and cartilage stresses is only applicable to the acute case. As healing of the ligamentous injuries commences, the ROM of the spine generally decreases to levels below the intact case. Thus, the current simulations are not applicable beyond the first few weeks to months after injury [3, 10]. However, consideration of irregular strains in certain tissues appears to be critical over longer terms. For example, the anterior annulus fibrosus is susceptible to lesions even at sub-failure strains to the overlying ALL. This damage to the annulus has been linked to the development of osteoarthritis [46].

Table 14: Cervical stabilization of the spine with ligamentous and intertransverse tissue injury is recommended when measured values exceed that of the intact 1.5 Nm-loaded case.

<b>Injury</b>	<b>Excessive Annular Strain</b>	<b>Excessive Facet Cartilage Stress</b>	<b>Excessive Foraminal Constriction</b>	<b>Stabilization Recommended</b>
Partial FC	YES	YES	YES	YES
Full FC	YES	YES	YES	YES
Partial FC+ALL	YES	YES	YES	YES
Full FC+ALL	YES	YES	YES	YES
Partial LF+ISL	no	no	no	no
Full LF+ISL	no	no	no	no
Partial FC+ALL+LF+ISL	YES	YES	YES	YES
Full FC+ALL+LF+ISL	YES	YES	YES	YES

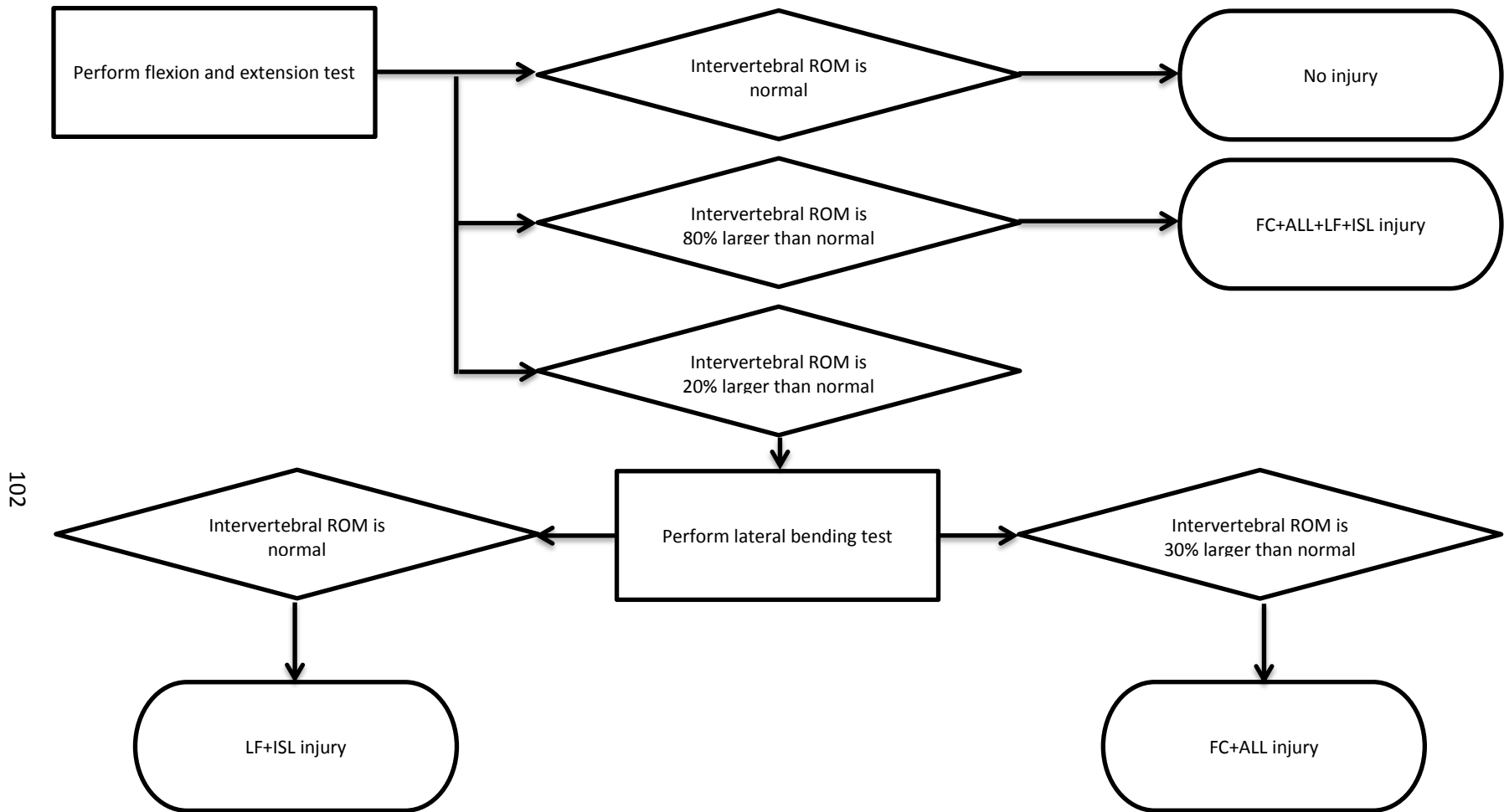


Figure 60: A diagnostic flowchart to be utilized with clinical range of motion test data.

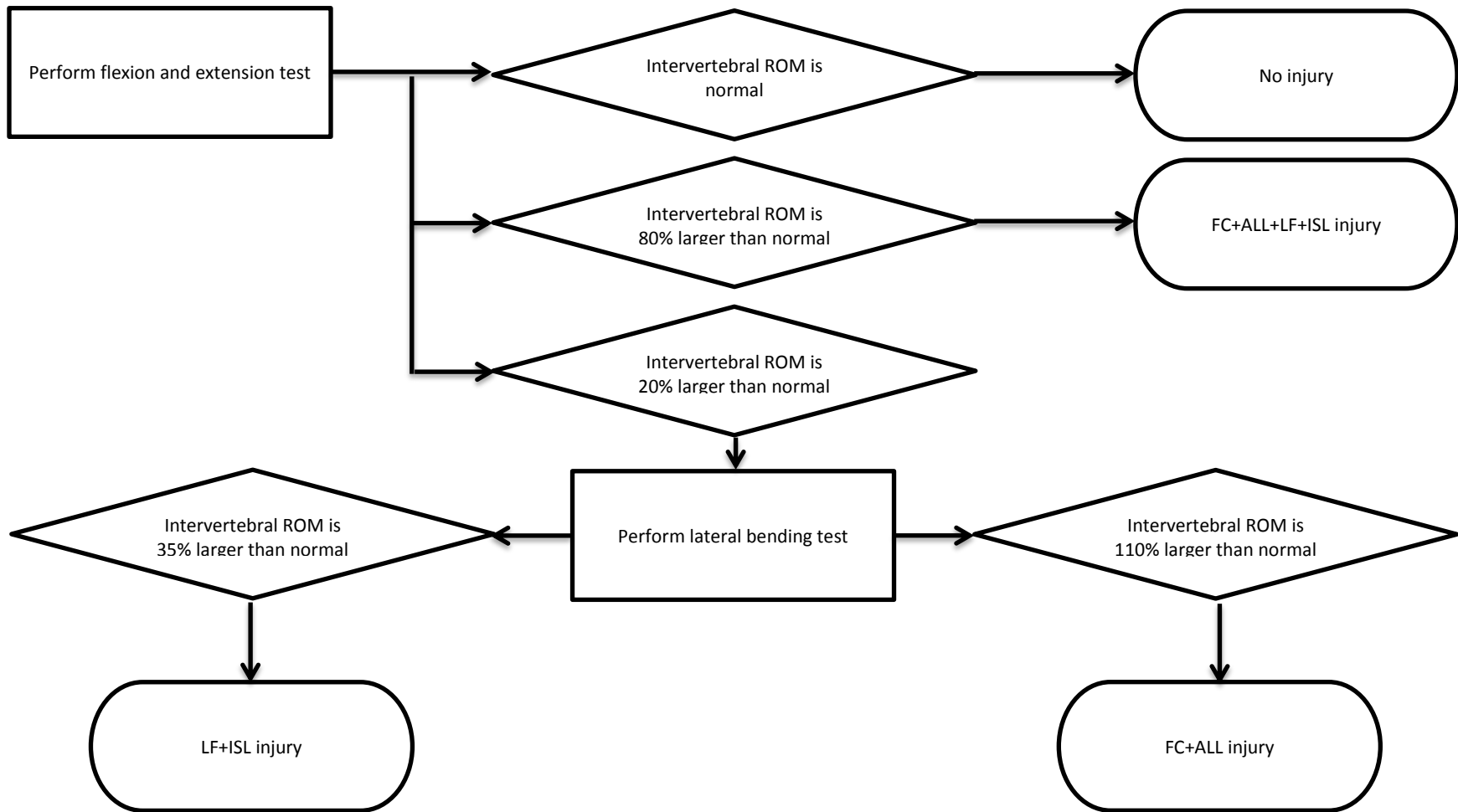


Figure 61: A diagnostic flowchart to be utilized with clinical range of motion test data with intertransverse tissue damage.

#### 4 OVERALL CONCLUSIONS

- The finite element model of the human upper cervical spine was converged with respect to multiple metrics, and has demonstrated accurate predictions with respect to experimentally-measured ROM and facet contact pressure. The model was validated with various ligaments absent to ensure each individual ligament was mechanically contributing to the overall structure with accurate properties.
- Commonly damaged cervical ligaments were found to suffer a large degree of permanent deformation post-injury. There was a great variability with respect to the post-injury stiffness reduction dependent on the type of ligament. Alar and flaval ligaments demonstrated minimal stiffness loss after injury, while the anterior longitudinal ligaments suffered nearly a 60% loss.
- Study of ligamentous injuries in the lower cervical spine found a very different kinematic response between FC+ALL injuries and LF+ISL injuries when observed in axial rotation and lateral bending. The same simulations demonstrated that the kinematic difference between these injuries is largely undetectable when only tested in flexion and extension motion. This finding may now allow the specific diagnosis of ligamentous injuries from simple radiographs by the addition of a lateral bending diagnostic range of motion test.

## 5 FUTURE WORK

The most straightforward improvement to this work would be the obtainment of clinical data detailing the frequency of injuries to the tissues between the transverse processes when ligamentous injury is present. Armed with this data, it would be possible to definitively state the expected increase in axial rotation and lateral bending ROM subsequent to ligamentous injuries.

Altering the FE model to enable the active simulation of injuries would be another interesting continuation of this work. Finding the combinations of motion paths and magnitudes necessary to induce injury to both bony and soft tissues may allow cervical spine safety to be improved in a variety of situations. A possible application could be the design of vehicular head restraints; improving the mechanism to prevent the most injurious motions of the spine has potential to improve occupant safety [122]. Steps necessary to achieve this goal include allowing the tissues to assume a set of “injured” mechanical properties once specified failure thresholds are reached. This is similar to the inclusion of “post-yield” mechanical properties in a standard impact/deformation simulation. A great deal of validation data could be sourced from clinical injury studies, where the anatomic locations of common injuries have been previously catalogued. The goal would be to virtually simulate these same injuries by enacting a trauma loading. Ideally, the model would include viscoelastic properties for the tissues, such that the predictions can be dependent on the timescale/speed of the injury mechanism. This most likely requires conversion of the model to utilize a “time-explicit” code.

Further study of the characteristics of the facet capsule ligaments may allow us to better understand their injury mechanism. The facet capsule ligaments contribute greatly to the kinematics of the spine, and have been previously linked to post-injury pain owing to their rich innervation [123]. Due to the ligaments' proximity to the intervertebral center of rotation, the ligaments experience both a tensile and shear loading during motions of the spine. This loading condition is much more difficult to simulate than the simple uniaxial tensile loading applied to most other spinal ligaments. The construction of a testing apparatus that can apply tensile loading to the facet capsule ligaments, while approximating the shear loading seen during facet sliding may allow a more realistic characterization of the mechanical properties of these ligaments.

Since clinical ROM testing for injury detection is generally accomplished using the active musculature of the patient, replicating muscle forces within the FE model may yield slightly different results. Although the kinematic similarity between moment loading and muscle loading for intact spines has been demonstrated, the loading comparison with injured spines has not received the same degree of study [10, 31]. The addition of muscular tissue may also increase the prediction accuracy of bony tissue stresses and strains if the physiologic attachment points are modeled appropriately.

## 6 REFERENCES

1. ABAQUS, *ABAQUS v6.9-EF2 Documentation*. 2010, Dassault Systemes - Simulia.
2. Alleyne, C.H., Jr., C.M. Cawley, D.L. Barrow, and G.D. Bonner, *Microsurgical anatomy of the dorsal cervical nerve roots and the cervical dorsal root ganglion/ventral root complexes*. *Surg Neurol*, 1998. **50**(3): p. 213-8.
3. Antonaci, F., M. Bulgheroni, S. Ghirmai, S. Lanfranchi, E. Dalla Toffola, G. Sandrini, and G. Nappi, *3D kinematic analysis and clinical evaluation of neck movements in patients with whiplash injury*. *Cephalalgia*, 2002. **22**(7): p. 533-42.
4. Armstrong, C.G. and V.C. Mow, *Variations in the intrinsic mechanical properties of human articular cartilage with age, degeneration, and water content*. *J Bone Joint Surg Am*, 1982. **64**(1): p. 88-94.
5. Ateshian, G.A., W.H. Warden, J.J. Kim, R.P. Grelsamer, and V.C. Mow, *Finite deformation biphasic material properties of bovine articular cartilage from confined compression experiments*. *J Biomech*, 1997. **30**(11-12): p. 1157-64.
6. Ayturk, U. and C. Puttlitz, *Parametric convergence sensitivity and validation of a finite element model of the human lumbar spine*. *Computer methods in biomechanics and biomedical engineering*, 2011.
7. Bass, C.R., S.R. Lucas, R.S. Salzar, M.L. Oyen, C. Planchak, B.S. Shender, and G. Paskoff, *Failure properties of cervical spinal ligaments under fast strain rate deformations*. *Spine (Phila Pa 1976)*, 2007. **32**(1): p. E7-13.
8. Benzel, E.C., B.L. Hart, P.A. Ball, N.G. Baldwin, W.W. Orrison, and M.C. Espinosa, *Magnetic resonance imaging for the evaluation of patients with occult cervical spine injury*. *J Neurosurg*, 1996. **85**(5): p. 824-9.
9. Bhattacharjee, A., *calib\_eval\_uncalibrated*. 2009.
10. Bonelli, A., P. Donati, G. Maltoni, F. Puglisi, and G.A. Norelli, *Neck motion evaluation after whiplash: a radiographic and kinematic protocol*. *Ital J Anat Embryol*, 2000. **105**(1): p. 51-62.
11. Brolin, K. and P. Halldin, *Development of a finite element model of the upper cervical spine and a parameter study of ligament characteristics*. *Spine (Phila Pa 1976)*, 2004. **29**(4): p. 376-85.
12. Carter, D.R. and W.C. Hayes, *The compressive behavior of bone as a two-phase porous structure*. *J Bone Joint Surg Am*, 1977. **59**(7): p. 954-62.
13. Carter, D.R., T.E. Orr, and D.P. Fyhrie, *Relationships between loading history and femoral cancellous bone architecture*. *J Biomech*, 1989. **22**(3): p. 231-44.

14. Cattrysse, E., M. Barbero, P. Kool, O. Gagey, J.P. Clarys, and P. Van Roy, *3D morphometry of the transverse and alar ligaments in the occipito-atlanto-axial complex: an in vitro analysis*. Clin Anat, 2007. **20**(8): p. 892-8.
15. Cavanaugh, J.M., A.C. Ozaktay, H.T. Yamashita, and A.I. King, *Lumbar facet pain: biomechanics, neuroanatomy and neurophysiology*. J Biomech, 1996. **29**(9): p. 1117-29.
16. Chang, U.K., D.H. Kim, M.C. Lee, R. Willenberg, S.H. Kim, and J. Lim, *Changes in adjacent-level disc pressure and facet joint force after cervical arthroplasty compared with cervical discectomy and fusion*. J Neurosurg Spine, 2007. **7**(1): p. 33-9.
17. Chazal, J., A. Tanguy, M. Bourges, G. Gaurel, G. Escande, M. Guillot, and G. Vanneuville, *Biomechanical properties of spinal ligaments and a histological study of the supraspinal ligament in traction*. J Biomech, 1985. **18**(3): p. 167-76.
18. Ciarelli, M.J., S.A. Goldstein, J.L. Kuhn, D.D. Cody, and M.B. Brown, *Evaluation of orthogonal mechanical properties and density of human trabecular bone from the major metaphyseal regions with materials testing and computed tomography*. J Orthop Res, 1991. **9**(5): p. 674-82.
19. Clausen, J.D., V.K. Goel, V.C. Traynelis, and J. Scifert, *Uncinate processes and Luschka joints influence the biomechanics of the cervical spine: quantification using a finite element model of the C5-C6 segment*. J Orthop Res, 1997. **15**(3): p. 342-7.
20. Como, J.J., M.A. Thompson, J.S. Anderson, R.R. Shah, J.A. Claridge, C.J. Yowler, and M.A. Malangoni, *Is magnetic resonance imaging essential in clearing the cervical spine in obtunded patients with blunt trauma?* J Trauma, 2007. **63**(3): p. 544-9.
21. Crisco, J.J., 3rd, T. Oda, M.M. Panjabi, H.U. Bueff, J. Dvorak, and D. Grob, *Transections of the C1-C2 joint capsular ligaments in the cadaveric spine*. Spine (Phila Pa 1976), 1991. **16**(10 Suppl): p. S474-9.
22. Crisco, J.J., 3rd, M.M. Panjabi, and J. Dvorak, *A model of the alar ligaments of the upper cervical spine in axial rotation*. J Biomech, 1991. **24**(7): p. 607-14.
23. Dickerman, R.D., M.A. Mittler, C. Warshaw, and J.A. Epstein, *Spinal cord injury in a 14-year-old male secondary to cervical hyperflexion with exercise*. Spinal Cord, 2006. **44**(3): p. 192-5.
24. Dickman, C.A., A. Mamourian, V.K. Sonntag, and B.P. Drayer, *Magnetic resonance imaging of the transverse atlantal ligament for the evaluation of atlantoaxial instability*. J Neurosurg, 1991. **75**(2): p. 221-7.
25. Douglass, A.B. and E.T. Bope, *Evaluation and treatment of posterior neck pain in family practice*. J Am Board Fam Pract, 2004. **17** Suppl: p. S13-22.
26. Dvorak, J. and M.M. Panjabi, *Functional anatomy of the alar ligaments*. Spine (Phila Pa 1976), 1987. **12**(2): p. 183-9.
27. Dvorak, J., E. Schneider, P. Saldinger, and B. Rahn, *Biomechanics of the craniocervical region: the alar and transverse ligaments*. J Orthop Res, 1988. **6**(3): p. 452-61.
28. Ebraheim, N.A., H.S. An, R. Xu, M. Ahmad, and R.A. Yeasting, *The quantitative anatomy of the cervical nerve root groove and the intervertebral foramen*. Spine (Phila Pa 1976), 1996. **21**(14): p. 1619-23.

29. Eubanks, A.C., J.A. Hipp, R. Lador, P.J. Ben-Galim, and C.A. Reitman, *Reference data for assessing widening between spinous processes in the cervical spine and the responsiveness of these measures to detecting abnormalities*. Spine J, 2010. **10**(3): p. 230-7.
30. Foreman, S.M. and A.C. Croft, *Whiplash injuries : the cervical acceleration/deceleration syndrome*. 3rd ed. 2002, Philadelphia: Lippincott Williams & Wilkins. xvi, 581 p.
31. Gadomski, B., C. Puttlitz, and J. Rasmussen, *The Effect of Muscle Loading on Internal Mechanical Parameters of the Lumbar Spine: A Finite Element Study*, in *Summer Bioengineering Conference*. 2011, American Society of Mechanical Engineers: Namacola, PA.
32. Goel, V.K., C.R. Clark, D. McGowan, and S. Goyal, *An in-vitro study of the kinematics of the normal, injured and stabilized cervical spine*. J Biomech, 1984. **17**(5): p. 363-76.
33. Goel, V.K. and J.D. Clausen, *Prediction of load sharing among spinal components of a C5-C6 motion segment using the finite element approach*. Spine (Phila Pa 1976), 1998. **23**(6): p. 684-91.
34. Goradia, D., K.F. Linnau, W.A. Cohen, S. Mirza, D.K. Hallam, and C.C. Blackmore, *Correlation of MR imaging findings with intraoperative findings after cervical spine trauma*. AJNR Am J Neuroradiol, 2007. **28**(2): p. 209-15.
35. Gray, H. *Anatomy Descriptive and Surgical (Gray's Anatomy)*. 1858 01/07/2010]; Available from: <http://en.wikipedia.org/wiki/File:Gray87.png>.
36. Gray, H., *Gray's Anatomy*. 20th ed, ed. W. Lewis. 1918, Philadelphia, PA: Lea & Febiger.
37. Gundiah, N., B.R. M, and A.P. L, *Determination of strain energy function for arterial elastin: Experiments using histology and mechanical tests*. J Biomech, 2007. **40**(3): p. 586-94.
38. Hall, R.M., R.J. Oakland, R.K. Wilcox, and D.C. Barton, *Spinal cord-fragment interactions following burst fracture: an in vitro model*. J Neurosurg Spine, 2006. **5**(3): p. 243-50.
39. Harrison, D.D., T.J. Janik, S.J. Troyanovich, and B. Holland, *Comparisons of lordotic cervical spine curvatures to a theoretical ideal model of the static sagittal cervical spine*. Spine (Phila Pa 1976), 1996. **21**(6): p. 667-75.
40. Harrison, J.L. and S.J. Ostlere, *Diagnosing purely ligamentous injuries of the cervical spine in the unconscious trauma patient*. Br J Radiol, 2004. **77**(916): p. 276-8.
41. Hogan, G.J., S.E. Mirvis, K. Shanmuganathan, and T.M. Scalea, *Exclusion of unstable cervical spine injury in obtunded patients with blunt trauma: is MR imaging needed when multi-detector row CT findings are normal?* Radiology, 2005. **237**(1): p. 106-13.
42. Holzapfel, G.A., C.A. Schulze-Bauer, G. Feigl, and P. Regitnig, *Single lamellar mechanics of the human lumbar anulus fibrosus*. Biomech Model Mechanobiol, 2005. **3**(3): p. 125-40.
43. Humphreys, S.C., H.S. An, J.C. Eck, M. Coppes, T.H. Lim, and L. Estkowski, *Oblique MRI as a useful adjunct in evaluation of cervical foraminal impingement*. J Spinal Disord, 1998. **11**(4): p. 295-9.

44. Ito, S., P.C. Ivancic, M.M. Panjabi, and B.W. Cunningham, *Soft tissue injury threshold during simulated whiplash: a biomechanical investigation*. Spine (Phila Pa 1976), 2004. **29**(9): p. 979-87.
45. Ivancic, P.C., M.P. Coe, A.B. Ndu, Y. Tominaga, E.J. Carlson, W. Rubin, F.H. Dipl-Ing, and M.M. Panjabi, *Dynamic mechanical properties of intact human cervical spine ligaments*. Spine J, 2007. **7**(6): p. 659-65.
46. Ivancic, P.C., A.M. Pearson, M.M. Panjabi, and S. Ito, *Injury of the anterior longitudinal ligament during whiplash simulation*. Eur Spine J, 2004. **13**(1): p. 61-8.
47. Johnson, R.M., E.S. Crelin, A.A. White, 3rd, M.M. Panjabi, and W.O. Southwick, *Some new observations on the functional anatomy of the lower cervical spine*. Clin Orthop Relat Res, 1975(111): p. 192-200.
48. Joshi, A., *Mechanical Behavior Of The Human Lumbar Intervertebral Disc With Polymeric Hydrogel Nucleus Implant: An Experimental And Finite Element Study*. 2004, Drexel.
49. Jost, R. and G. Nurick, *Development of a finite element model of the human neck subjected to high g-level lateral deceleration*. International Journal of Crashworthiness, 2000. **5**(3): p. 259-270.
50. Kaale, B.R., J. Krakenes, G. Albrektsen, and K. Wester, *Active range of motion as an indicator for ligament and membrane lesions in the upper cervical spine after a whiplash trauma*. J Neurotrauma, 2007. **24**(4): p. 713-21.
51. Kitagawa, T., A. Fujiwara, N. Kobayashi, K. Saiki, K. Tamai, and K. Saotome, *Morphologic changes in the cervical neural foramen due to flexion and extension: in vivo imaging study*. Spine (Phila Pa 1976), 2004. **29**(24): p. 2821-5.
52. Klisch, S.M., *A bimodular theory for finite deformations: Comparison of orthotropic second-order and exponential stress constitutive equations for articular cartilage*. Biomech Model Mechanobiol, 2006. **5**(2-3): p. 90-101.
53. Klisch, S.M. and J.C. Lotz, *Application of a fiber-reinforced continuum theory to multiple deformations of the annulus fibrosus*. J Biomech, 1999. **32**(10): p. 1027-36.
54. Kumaresan, S., N. Yoganandan, and F.A. Pintar, *Finite element modeling approaches of human cervical spine facet joint capsule*. J Biomech, 1998. **31**(4): p. 371-6.
55. Leahy, P.D., B.S. Smith, K.L. Easton, C.E. Kawcak, J.C. Eickhoff, S.S. Shetye, and C.M. Puttlitz, *Correlation of mechanical properties within the equine third metacarpal with trabecular bending and multi-density micro-computed tomography data*. Bone, 2010. **46**(4): p. 1108-13.
56. Lee, C.K., Y.E. Kim, C.S. Lee, Y.M. Hong, J.M. Jung, and V.K. Goel, *Impact response of the intervertebral disc in a finite-element model*. Spine (Phila Pa 1976), 2000. **25**(19): p. 2431-9.
57. Lee, I.H., H.Y. Choi, J.H. Lee, and D.C. Han, *Development of finite element human neck model for vehicle safety simulation*. International Journal of Automotive Technology, 2004. **5**(1): p. 33-46.
58. Lee, K.E., A.N. Franklin, M.B. Davis, and B.A. Winkelstein, *Tensile cervical facet capsule ligament mechanics: failure and subfailure responses in the rat*. J Biomech, 2006. **39**(7): p. 1256-64.

59. Lentell, G., M. Kruse, B. Chock, K. Wilson, M. Iwamoto, and R. Martin, *Dimensions of the cervical neural foramina in resting and retracted positions using magnetic resonance imaging*. J Orthop Sports Phys Ther, 2002. **32**(8): p. 380-90.
60. Lucas, S.R., C.R. Bass, R.S. Salzar, M.L. Oyen, C. Planchak, A. Ziemba, B.S. Shender, and G. Paskoff, *Viscoelastic properties of the cervical spinal ligaments under fast strain-rate deformations*. Acta Biomater, 2008. **4**(1): p. 117-25.
61. Lysell, E., *Motion in the cervical spine. An experimental study on autopsy specimens*. Acta Orthop Scand, 1969: p. Suppl 123:1+.
62. Maak, T.G., Y. Tominaga, M.M. Panjabi, and P.C. Ivancic, *Alar, transverse, and apical ligament strain due to head-turned rear impact*. Spine (Phila Pa 1976), 2006. **31**(6): p. 632-8.
63. Marion, D.W., R. Domeier, C.M. Dunham, F.A. Luchette, R. Haid, and S.C. Erwood, *PRACTICE MANAGEMENT GUIDELINES FOR IDENTIFYING CERVICAL SPINE INJURIES FOLLOWING TRAUMA*. Eastern Association for the Surgery of Trauma, 1998.
64. Maurel, N., F. Lavaste, and W. Skalli, *A three-dimensional parameterized finite element model of the lower cervical spine. Study of the influence of the posterior articular facets*. J Biomech, 1997. **30**(9): p. 921-31.
65. McAfee, P.C., B.W. Cunningham, V. Hayes, F. Sidiqi, M. Dabbah, J.C. Seftor, N. Hu, and H. Beatson, *Biomechanical analysis of rotational motions after disc arthroplasty: implications for patients with adult deformities*. Spine (Phila Pa 1976), 2006. **31**(19 Suppl): p. S152-60.
66. Menezes, A.H., *Decision making*. Childs Nerv Syst, 2008. **24**(10): p. 1147-53.
67. Mercer, S.R. and N. Bogduk, *Clinical anatomy of ligamentum nuchae*. Clin Anat, 2003. **16**(6): p. 484-93.
68. Middleditch, A. and J. Oliver, *Functional Anatomy of the Spine*. Second ed. 2005, London: Elsevier Ltd.
69. Moroney, S.P., A.B. Schultz, J.A. Miller, and G.B. Andersson, *Load-displacement properties of lower cervical spine motion segments*. J Biomech, 1988. **21**(9): p. 769-79.
70. Mow, V.C. and R. Huiskes, *Basic Orthopaedic Biomechanics and Mechano-Biology: Third Edition*. Third ed. 2005, Philadelphia, PA: Lippincott Williams & Williams.
71. Myklebust, J.B., F. Pintar, N. Yoganandan, J.F. Cusick, D. Maiman, T.J. Myers, and A. Sances, Jr., *Tensile strength of spinal ligaments*. Spine (Phila Pa 1976), 1988. **13**(5): p. 526-31.
72. Nachemson, A.L. and J.H. Evans, *Some mechanical properties of the third human lumbar interlaminar ligament (ligamentum flavum)*. J Biomech, 1968. **1**(3): p. 211-20.
73. Ng, H.W. and E.C. Teo, *Nonlinear finite-element analysis of the lower cervical spine (C4-C6) under axial loading*. J Spinal Disord, 2001. **14**(3): p. 201-10.
74. Ng, H.W., E.C. Teo, and V.S. Lee, *Statistical factorial analysis on the material property sensitivity of the mechanical responses of the C4-C6 under compression, anterior and posterior shear*. J Biomech, 2004. **37**(5): p. 771-7.

75. Nibu, K., J. Cholewicki, M.M. Panjabi, L.B. Babat, J.N. Grauer, R. Kothe, and J. Dvorak, *Dynamic elongation of the vertebral artery during an in vitro whiplash simulation*. Eur Spine J, 1997. **6**(4): p. 286-9.
76. Okada, E., M. Matsumoto, D. Ichihara, K. Chiba, Y. Toyama, H. Fujiwara, S. Momoshima, Y. Nishiwaki, T. Hashimoto, J. Ogawa, M. Watanabe, and T. Takahata, *Does the sagittal alignment of the cervical spine have an impact on disk degeneration? Minimum 10-year follow-up of asymptomatic volunteers*. European Spine Journal, 2009. **18**(11): p. 1644-1651.
77. Ouyang, H., W. Sun, Y. Fu, J. Li, J.X. Cheng, E. Nauman, and R. Shi, *Compression induces acute demyelination and potassium channel exposure in spinal cord*. J Neurotrauma, 2010. **27**(6): p. 1109-20.
78. Panjabi, M., J. Dvorak, J. Crisco, 3rd, T. Oda, A. Hilibrand, and D. Grob, *Flexion, extension, and lateral bending of the upper cervical spine in response to alar ligament transections*. J Spinal Disord, 1991. **4**(2): p. 157-67.
79. Panjabi, M., J. Dvorak, J.J. Crisco, 3rd., T. Oda, P. Wang, and D. Grob, *Effects of alar ligament transection on upper cervical spine rotation*. J Orthop Res, 1991. **9**(4): p. 584-93.
80. Panjabi, M., J. Dvorak, J. Duranceau, I. Yamamoto, M. Gerber, W. Rauschnig, and H.U. Bueff, *Three-dimensional movements of the upper cervical spine*. Spine (Phila Pa 1976), 1988. **13**(7): p. 726-30.
81. Panjabi, M.M., J.J. Crisco, 3rd, C. Lydon, and J. Dvorak, *The mechanical properties of human alar and transverse ligaments at slow and fast extension rates*. Clin Biomech (Bristol, Avon), 1998. **13**(2): p. 112-120.
82. Panjabi, M.M., J.J. Crisco, A. Vasavada, T. Oda, J. Cholewicki, K. Nibu, and E. Shin, *Mechanical properties of the human cervical spine as shown by three-dimensional load-displacement curves*. Spine (Phila Pa 1976), 2001. **26**(24): p. 2692-700.
83. Panjabi, M.M., T.G. Maak, P.C. Ivancic, and S. Ito, *Dynamic intervertebral foramen narrowing during simulated rear impact*. Spine (Phila Pa 1976), 2006. **31**(5): p. E128-34.
84. Panjabi, M.M., T.R. Oxland, and E.H. Parks, *Quantitative anatomy of cervical spine ligaments. Part I. Upper cervical spine*. J Spinal Disord, 1991. **4**(3): p. 270-6.
85. Panjabi, M.M., A.M. Pearson, S. Ito, P.C. Ivancic, S.E. Gimenez, and Y. Tominaga, *Cervical spine ligament injury during simulated frontal impact*. Spine (Phila Pa 1976), 2004. **29**(21): p. 2395-403.
86. Panjabi, M.M., A.A. White, 3rd, and R.M. Johnson, *Cervical spine mechanics as a function of transection of components*. J Biomech, 1975. **8**(5): p. 327-36.
87. Panzer, M.B. and D.S. Cronin, *C4-C5 segment finite element model development, validation, and load-sharing investigation*. J Biomech, 2009. **42**(4): p. 480-90.
88. Patwardhan, A.G., R.M. Havey, A.J. Ghanayem, H. Diener, K.P. Meade, B. Dunlap, and S.D. Hodges, *Load-carrying capacity of the human cervical spine in compression is increased under a follower load*. Spine (Phila Pa 1976), 2000. **25**(12): p. 1548-54.
89. Pintar, F.A., *THE BIOMECHANICS OF SPINAL ELEMENTS (LIGAMENTS, VERTEBRAL BODY, DISC)*. 1986, Marquette: Milwaukee.

90. Pitzen, T., B. Schmitz, T. Georg, D. Barbier, T. Beuter, W.I. Steudel, and W. Reith, *Variation of endplate thickness in the cervical spine*. Eur Spine J, 2004. **13**(3): p. 235-40.
91. Planchak, C., *Temperature Effects on Viscoelastic Properties of Ligaments*. 2006, University of Virginia: Charlottesville.
92. Przybylski, G.J., G.J. Carlin, P.R. Patel, and S.L. Woo, *Human anterior and posterior cervical longitudinal ligaments possess similar tensile properties*. J Orthop Res, 1996. **14**(6): p. 1005-8.
93. Puttlitz, C.M., V.K. Goel, C.R. Clark, V.C. Traynelis, J.L. Scifert, and N.M. Grosland, *Biomechanical rationale for the pathology of rheumatoid arthritis in the craniovertebral junction*. Spine (Phila Pa 1976), 2000. **25**(13): p. 1607-16.
94. Quinn, K.P. and B.A. Winkelstein, *Cervical facet capsular ligament yield defines the threshold for injury and persistent joint-mediated neck pain*. J Biomech, 2007. **40**(10): p. 2299-306.
95. Reid, J.G. and P.A. Costigan, *Trunk muscle balance and muscular force*. Spine (Phila Pa 1976), 1987. **12**(8): p. 783-6.
96. Reilly, D.T. and A.H. Burstein, *Review article. The mechanical properties of cortical bone*. J Bone Joint Surg Am, 1974. **56**(5): p. 1001-22.
97. Rho, J.Y., R.B. Ashman, and C.H. Turner, *Young's modulus of trabecular and cortical bone material: ultrasonic and microtensile measurements*. J Biomech, 1993. **26**(2): p. 111-9.
98. Rho, J.Y., M.C. Hobatho, and R.B. Ashman, *Relations of mechanical properties to density and CT numbers in human bone*. Med Eng Phys, 1995. **17**(5): p. 347-55.
99. Richter, M., H.J. Wilke, P. Kluger, L. Claes, and W. Puhl, *Load-displacement properties of the normal and injured lower cervical spine in vitro*. Eur Spine J, 2000. **9**(2): p. 104-8.
100. Ritchie, R.O., J.H. Kinney, J.J. Kruzic, and R.K. Nalla, *A fracture mechanics and mechanistic approach to the failure of cortical bone*. Fatigue & Fracture of Engineering Materials & Structures, 2005. **28**(4): p. 345-371.
101. Saito, T., T. Yamamuro, J. Shikata, M. Oka, and S. Tsutsumi, *Analysis and prevention of spinal column deformity following cervical laminectomy. I. Pathogenetic analysis of postlaminectomy deformities*. Spine (Phila Pa 1976), 1991. **16**(5): p. 494-502.
102. Schinagl, R.M., D. Gurskis, A.C. Chen, and R.L. Sah, *Depth-dependent confined compression modulus of full-thickness bovine articular cartilage*. J Orthop Res, 1997. **15**(4): p. 499-506.
103. Schmitz, B., T. Pitzen, T. Beuter, W.I. Steudel, and W. Reith, *Regional variations in the thickness of cervical spine endplates as measured by computed tomography*. Acta Radiol, 2004. **45**(1): p. 53-8.
104. Seijas, R., O. Ares, and J. Casamitjana, *Occult ligamentous injury of the cervical spine associated with cervical spine fracture*. Acta Orthop Belg, 2005. **71**(6): p. 746-9.
105. Setton, L.A., W. Zhu, M. Weidenbaum, A. Ratcliffe, and V.C. Mow, *Compressive properties of the cartilaginous end-plate of the baboon lumbar spine*. J Orthop Res, 1993. **11**(2): p. 228-39.
106. Shim, V.P.W., J.F. Liu, and V.S. Lee, *A technique for dynamic tensile testing of human cervical spine ligaments*. Experimental Mechanics, 2006. **46**(1): p. 77-89.

107. Siegmund, G.P., B.S. Myers, M.B. Davis, H.F. Bohnet, and B.A. Winkelstein, *Mechanical evidence of cervical facet capsule injury during whiplash: a cadaveric study using combined shear, compression, and extension loading*. Spine (Phila Pa 1976), 2001. **26**(19): p. 2095-101.
108. Sliker, C.W., S.E. Mirvis, and K. Shanmuganathan, *Assessing cervical spine stability in obtunded blunt trauma patients: review of medical literature*. Radiology, 2005. **234**(3): p. 733-9.
109. Subramanian, N., C.A. Reitman, L. Nguyen, and J.A. Hipp, *Radiographic assessment and quantitative motion analysis of the cervical spine after serial sectioning of the anterior ligamentous structures*. Spine (Phila Pa 1976), 2007. **32**(5): p. 518-26.
110. Tominaga, Y., A.B. Ndu, M.P. Coe, A.J. Valenson, P.C. Ivancic, S. Ito, W. Rubin, and M.M. Panjabi, *Neck ligament strength is decreased following whiplash trauma*. BMC Musculoskelet Disord, 2006. **7**: p. 103.
111. Troyer, K.L. and C.M. Puttlitz, *Human cervical spine ligaments exhibit fully nonlinear viscoelastic behavior*. Acta Biomater, 2011. **7**(2): p. 700-9.
112. Tubbs, R.S., J. Dixon, M. Loukas, M.M. Shoja, and A.A. Cohen-Gadol, *Ligament of Barkow of the craniocervical junction: its anatomy and potential clinical and functional significance*. J Neurosurg Spine, 2010. **12**(6): p. 619-22.
113. Tubbs, R.S., P. Grabb, A. Spooner, W. Wilson, and W.J. Oakes, *The apical ligament: anatomy and functional significance*. J Neurosurg, 2000. **92**(2 Suppl): p. 197-200.
114. Tubbs, R.S., C.J. Griessenauer, J.G. McDaniel, A.M. Burns, A. Kumbla, and A.A. Cohen-Gadol, *The transverse occipital ligament: anatomy and potential functional significance*. Neurosurgery, 2010. **66**(3 Suppl Operative): p. 1-3; discussion 3.
115. Tubbs, R.S., D.R. Kelly, E.R. Humphrey, G.D. Chua, M.M. Shoja, E.G. Salter, L. Acakpo-Satchivi, J.C. Wellons, 3rd, J.P. Blount, and W.J. Oakes, *The tectorial membrane: anatomical, biomechanical, and histological analysis*. Clin Anat, 2007. **20**(4): p. 382-6.
116. Tubbs, R.S., E.G. Salter, and W.J. Oakes, *The accessory atlantoaxial ligament*. Neurosurgery, 2004. **55**(2): p. 400-2; discussion 402-4.
117. Tubbs, R.S., W. Stetler, M.M. Shoja, M. Loukas, A. Hansasuta, P. Liechty, L. Acakpo-Satchivi, J.C. Wellons, J.P. Blount, E.G. Salter, and W.J. Oakes, *The lateral atlantooccipital ligament*. Surg Radiol Anat, 2007. **29**(3): p. 219-23.
118. Urbina, A., T. Paez, and B. Rutherford. *Validation of Mathematical Models: An Overview of the Process*. in SEM Annual Conference and Exposition on Experimental and Applied Mechanics. 2005.
119. Wen, N., F. Lavaste, J.J. Santin, and J.P. Lassau, *Three-dimensional biomechanical properties of the human cervical spine in vitro. II. Analysis of instability after ligamentous injuries*. Eur Spine J, 1993. **2**(1): p. 12-5.
120. Wheeldon, J.A., B.D. Stemper, N. Yoganandan, and F.A. Pintar, *Validation of a finite element model of the young normal lower cervical spine*. Ann Biomed Eng, 2008. **36**(9): p. 1458-69.

121. White III, A. and M. Panjabi, *Spinal Kinematics. The Research Status of Spinal Manipulative Therapy*, N. Monogram, Editor. 1975, U.S. Department of Health, Education and Welfare: Washington, DC.
122. White III, A.A. and M.M. Panjabi, *Clinical Biomechanics of the Spine: Second Edition*. Second ed. 1990, Philadelphia, PA: J.B. Lippincott Company.
123. Winkelstein, B.A., R.W. Nightingale, W.J. Richardson, and B.S. Myers, *The cervical facet capsule and its role in whiplash injury: a biomechanical investigation*. Spine (Phila Pa 1976), 2000. **25**(10): p. 1238-46.
124. Womack, W., *Computational Modeling of the Lower Cervical Spine: Facet Cartilage Distribution and Disc Replacement*. 2009, Colorado State University.
125. Womack, W., P. Leahy, V. Patel, and C. Puttlitz, *Finite element modeling of kinematic and load transmission alterations due to cervical intervertebral disc replacement*. Spine (Phila Pa 1976), 2011.
126. Womack, W., D. Woldtvedt, and C.M. Puttlitz, *Lower cervical spine facet cartilage thickness mapping*. Osteoarthritis Cartilage, 2008. **16**(9): p. 1018-23.
127. Woo, S.L., C.A. Orlando, J.F. Camp, and W.H. Akeson, *Effects of postmortem storage by freezing on ligament tensile behavior*. J Biomech, 1986. **19**(5): p. 399-404.
128. [www.ispub.com](http://www.ispub.com).
129. [www.uphs.penn.edu](http://www.uphs.penn.edu).
130. Yamaura, I., K. Yone, S. Nakahara, T. Nagamine, H. Baba, K. Uchida, and S. Komiya, *Mechanism of destructive pathologic changes in the spinal cord under chronic mechanical compression*. Spine (Phila Pa 1976), 2002. **27**(1): p. 21-6.
131. Yang, K.H., F. Zhu, F. Luan, L. Zhao, and P.C. Begeman, *Development of a Finite Element Model of the Human Neck*. 42nd Stapp Car Crash Conference proceedings, Society of Automotive Engineers, Inc, 1998: p. 195-205.
132. Yoganandan, N., S.A. Knowles, D.J. Maiman, and F.A. Pintar, *Anatomic study of the morphology of human cervical facet joint*. Spine (Phila Pa 1976), 2003. **28**(20): p. 2317-23.
133. Yoganandan, N., S. Kumaresan, and F.A. Pintar, *Biomechanics of the cervical spine Part 2. Cervical spine soft tissue responses and biomechanical modeling*. Clin Biomech (Bristol, Avon), 2001. **16**(1): p. 1-27.
134. Yuksel, K.Z., M. Yuksel, L.F. Gonzalez, S. Baek, J.E. Heiserman, V.K. Sonntag, and N.R. Crawford, *Occipitocervical vertical distraction injuries: anatomical biomechanical, and 3-tesla magnetic resonance imaging investigation*. Spine (Phila Pa 1976), 2008. **33**(19): p. 2066-73.
135. Zhang, H. and J. Bai, *Development and validation of a finite element model of the occipito-atlantoaxial complex under physiologic loads*. Spine (Phila Pa 1976), 2007. **32**(9): p. 968-74.
136. Zhang, H. and J. Bai, *Nonlinear finite element analysis of C0-C1-C2 complex under physiologic loads*. Conf Proc IEEE Eng Med Biol Soc, 2005. **6**: p. 6165-7.

137. Zhang, Q.H., S.H. Tan, and E.C. Teo, *Finite element analysis of head-neck kinematics under simulated rear impact at different accelerations*. Proc Inst Mech Eng H, 2008. **222**(5): p. 781-90.